2015

An experimental study of wind-driven surface water transport process pertinent to aircraft icing

Kai Zhang
Iowa State University

Recommended Citation

Zhang, Kai, "An experimental study of wind-driven surface water transport process pertinent to aircraft icing" (2015). *Graduate Theses and Dissertations*. 14465.
https://lib.dr.iastate.edu/etd/14465

An experimental study of wind-driven surface water transport process pertinent to aircraft icing

by

Kai Zhang

A dissertation submitted to the graduate faculty

in partial fulfillment of the requirements for the degree of

DOCTOR OF PHILOSOPHY

Major: Aerospace Engineering

Program of Study Committee:
Hui Hu, Co-Major Professor
Alric P. Rothmayer, Co-Major Professor
Terrence R. Meyer
Chris R. Rehmann
Richard Wlezien

Iowa State University

Ames, Iowa

2015

TABLE OF CONTENTS

NOMENCLATURE

A	Rivulet cross-section area
c	Airfoil chord length
C_d	Drag coefficient
D	Roughness diameter
F_c/f_c	Centrifugal force/unit width centrifugal force at meandered rivulet cross-section
F_d/f_d	Aerodynamic drag/unit width aerodynamic drag at rivulet front
f_1	Surface wave frequency of film flow over flat plate
f_2	Surface wave frequency of film flow over roughness array
K	Grid displacement to height parameter
H_r	Roughness peak height
h	Water film thickness
$\bar{h}$	Time-averaged film thickness of film flow over flat plate
$\overline{h_r}$	Time-averaged film thickness of film flow over roughness array
LWC	Liquid water content
M	Water-air viscosity ratio
$\overline{\langle M_T \rangle}$	Averaged water mass trapped ratio
P/p	Static pressure/unit width static pressure within film/rivulet flow
Q/q	Liquid flow rate/unit width liquid flow rate
Re	Reynolds number
R_m	Initial radius of meandered rivulet curvature
T_σ/t_σ	Surface tension/unit width surface tension at film/rivulet front
Ts_σ/ts_σ	Surface tension /unit width surface tension at the cross-section of meandered rivulet
u, v	Local instantaneous velocity
U, V	Local time averaged velocity
U_∞	Free stream velocity

We	Weber number

Greek symbols

β	Impinging water droplet collection efficiency
δ	Velocity boundary layer thickness
μ	Dynamic viscosity
ν	Kinematic viscosity
φ	Yaw angle of meandered rivulet
ρ	Density
σ	Water surface tension
θ	Contact angle
τ_a	Air shear stress

Subscripts

a	Variables defined in air
f	Variables defined in film flow
r	Variables defined in rivulet flow
w	Variables defined in water
$*$	Non-dimensional quantities

ACKNOWLEDGEMENTS

I would like to express my gratefully and sincerely thanks to my major advisors, Dr. Hui Hu, whose expertise, enthusiasm, and research attitude have been influencing me during my entire Ph.D. period. Without his generous guidance and support, this dissertation would not have been possible. It was an honor for me to study under his assistance and to be one of his research students.

My heartily appreciation also goes to my co-advisor, Dr. Alric P. Rothmayer, for his advises about the scaling law of film thickness and water trapped effects induced by roughness. I also would like to thanks him for the helpful discussions. I wish to thank my committee members Dr. Chris R. Rehmann, Dr. Richard Wlezien and Dr. Terrence R. Meyer, for their generous help during my research. I would also like to thank them for evaluating my research work and giving me many insightful comments.

I would like to thank Mr. Bill Rickard, Mr. James Benson and Mr. Andrew Jordan, for their continuous help on setting up my experimental facilities. In addition, I would like to thank our graduate secretaries, Ms. Dee Pfeiffer, Ms. Gayle Fay, Ms. Laurie Hoifeldt and Ms. Jackie Kester for answering my endless questions about the graduate program and helping me prepare paper work.

I am grateful to Dr. Wei Tian and Dr. Wenli Chen for their valuable help. I wish to thank Dr. Blake Johnson, Mr. Yang Liu and Mr. Wenwu Zhou for their help during the experiments. I wish to than Dr. Rye Waldman and Mr. Andrew Bodling for their effects on revising my dissertation. I would like to thanks all the group members for providing me a good environment during the past four years.

Most important is the endless love and support from my parents, Debao Zhang and Qiaoling Kong, and my sister Yifei Zhang, without which nothing happens.

Finally, my fiancee Jie Bai is always my constant source of encouragement, and I thank her.

ABSTRACT

Water transport behaviors will significantly influence the icing accretion process during glaze icing conditions. Many important micro-physical processes associated with water transport phenomena, such as film/rivulet formation on the flat and curve surface, surface waves generation, and interaction of runback liquid with local ice roughnesses, are still unclear. In order to elucidate the underlying physics of water transport behaviors under icing conditions, advanced experimental technique capable of providing accurate measurements on the wind-driven thin film/rivulet flows are highly desirable. A novel digital image projection (DIP) system is presented in this work. Using this new technique, a comprehensive experimental study was conducted to quantify the transient behaviors of the wind-driven surface water transport processes pertinent to aircraft icing problems.

DIP technique is a further development of digital fringe projection (DFP) technique. In contrast to project sinusoidal patterns, the digital projector projects a grid pattern with known characteristics onto test objects (i.e., water droplet/rivulet flows over icing accreting surfaces). The heights of 3D objects are linear dependent on the grid point displacements between the measurement images of a 3D shape and the reference image of a zero height substrate. Compared with typical DFP measurement system, the DIP technique can significantly reduce the measurement error as well as decrease the requirement of the measurement image quality.

After carefully calibrated and validated, the proposed DIP technique was applied to characterize the wind-driven water rivulet flows. Seen from measurement results, the transient motion of rivulet front was found to be significantly influenced by the surface waves' behaviors. The Force Balance (FB) rivulet breaking criteria is further refined and evaluated by the reconstructed tiny rivulet flow structures. Rivulet meandering phenomena and the water mass

trapping induced by the meandered water-air contact line were observed. A model based on force balance analysis at the cross-section of meandering rivulet was built to illustrate the meandering instability of wind-driven rivulet flow.

In order to examine the effects of the roughness arrays on the surface film flow, i.e., trapped mass effects, which is pertinent to the surface water runback over airfoils/wings with ice roughness, the DIP technique was used to quantify the transient behavior of wind-driven film flow over a surface with roughness arrays. While surface water mass trapping was observed clearly right downstream of the roughness elements, some other interesting features about the water film flow within roughness elements were also revealed clearly from the quantitative DIP measurements, which were found to agree well with those previous numerical studies.

The water runback process on an airfoil surface was reconstructed by the DIP technique. The measurement results clearly revealed that, after impinged on the leading edge of the NACA0012 airfoil, the micro-sized water droplets would coalesce to form a thin water film in the region near the leading edge of the airfoil. The formation of rivulets was found to be time-dependent process and relies on the initial water runback flow structure. The film thickness scaling law is evaluated by the time-average measurements of the film thickness. The measurement results show good consistent with the analytical scaling predictions.

CHAPTER 1

GENERAL INTRODUCTION

Aircraft icing is one of the most dangerous threatens to aviation safety. Icing accretion is due to the supercooled water droplets impinging and frozen on the exposed aircraft surfaces. There are two types of icing accretion processes: glaze icing and rime icing. In a dry regime, all the collected water in the impingement area freezes on impact to form rime ice. For a wet regime, only a fraction of the collected water freezes in the impingement area to form glaze ice and the remaining water runs back and can freeze outside the impingement area. Because of its wet nature, glaze ice is much more dangerous than rime ice. It causes airplane performance degradation (Bragg et al. 1986) and inhibits the control of airplane (Ranaudo et al. 1991).

Water beads, rivulets and film flows were observed running back along the airfoil surface during glaze icing condition (Olsen and Walker 1987). Water runback also occurs at near frozen icing condition or ice particles melt by a thermal ice protection system. In those situations, no ice accretes near the stagnation, but the freezing water runback along the airfoil surface, causing ice accretion behind the protected areas of the wing (Ballough 2007). The water transport behaviors directly influence the icing accretion process by redistributing the super cooled water on the airfoil surface. Besides that, the film/rivulets flow will indirectly influence the ice accretion process by interacting with local ice roughnesses. This coupled effect will change the local heat transfer coefficient (Liu et al. 2015, Rothmayer and Hu 2012), moreover directly influence the water mass transport behavior by obstructing the liquid flow (Rothmayer and Hu 2014). Previous experimental investigations about surface water flows over aerodynamic shapes generally illustrated the macro water flow phenomena by analyzing videos taken in the experiments (Hansman and Barsotti 1985, Hansman and Craig 1987, Olsen and Walker 1987, Thompson and

Jang 1996). The important micro-physical processes such as film thickness distribution, contact line moving velocity, and wet surface area can not be well revealed in those videos. Advanced experimental techniques capable of providing accurate measurements to reveal the micro-transient phenomena pertinent to surface water runback are highly desired.

In chapter 2 of the current paper, a novel digital image projection (DIP) technique for measuring free surface deformation of wind-driven thin water film is presented. The ideas of DIP technique are inspired by Molecular tagging velocimetry (MTV) technique (Koochesfahani and Nocera 2007) and Digital Fringe Projection (DFP) technique (Gorthi and Rastogi 2010). For MTV technique, the velocity field is measured by the deformation of grid points which is generated by intersecting laser lines. Meanwhile, using DFP technique, 3D shapes are reconstructed by measuring the distortion of the sinusoidal patterns. The Key ideas of DIP technique are to replace the sinusoidal pattern with a grid line pattern using a digital projector; meanwhile replace the complex phase processing by cross-correlation calculation. The feasibility and implementation of the DIP system was preliminary demonstrated by a successfully reconstruction of a 3D sphere-head geometry and then further proved by measuring the film thickness distribution of wind-driven film flow over a flat plate surface.

A simulated icing condition test at NASA Lewis (Glenn) research center revealed that the water runback flow on a airfoil can be divided into a fully wetted film flow range and a partly wetted rivulets range (Gelder and Lewis 1951). Rivulets stagnation will provide enough time and water mass for the initial formation of ice roughness. The early investigations on break-up of stagnated wind-driven film/rivulet fronts were focused on preventing the dry-patch formation within the water film cooling equipments. Hartley and Murgatroyd (1964) established two film break-up criteria to determine the minimum liquid layer thickness for a dry-patch rewetting. One of the criteria is based on the force balance (FB) analysis near the stagnation range of a dry-patch. Since then the FB criterion has been widely used and developed by researchers (McAlister et al. 2005, Murgatroyd 1965, Penn et al. 2001, Thompson and Marrochello 1999). However, due to the limitation of experiment technique, the influences of micro-physical flow structures, such as surface waves, and irregular rivulet front shapes on the rivulet breaking are still unclear. Rivulet meandering is the other interesting phenomenon in this study. Especially the meandered rivulet contact line could trap a certain amount of freezing water, which also provides enough time and water mass for ice accretion. Although gravity-driven rivulets meandering had been investigated both experimentally and theoretically (Culkin and Davis 1984, Daerr et al. 2011, Drenckhan et al. 2004, Kim et al. 2004, Le Grand-Piteira et al. 2006, Nakagawa 1992, Tanner 1960), to the author's knowledge, research on wind-driven meandering is still blank.

In chapter 3, the FB model is extended by adding one more force term, i.e., aerodynamic drag. Furthermore, the force terms in the FB model (i.e., inertia force, air shear stress and aerodynamic drag) were refined by the dynamic behaviors of wind-driven rivulet flows that were measured experimentally by DIP technique. The refined model was then validated by the measurement results. One more aerodynamic drag term is added to Grand-Piteira's rivulet meandering model as well (Le Grand-Piteira, Daerr and Limat 2006). Scaling analysis is performed to further evaluate the relative importance of the force terms in the model. A rivulet meandering model was then established and used to predict the yaw angle of meander rivulets. Compared with the experimental measurements, the predicted results provide a reasonable well estimation.

Semi-regular roughness elements are often observed during ice accretion process (Anderson and Ruff 1998, Shin 1996). Local ice roughness choke a certain amount of water mass in place near the roughness elements which was observed in Waldman and Hu's (2015) high speed imaging experiments. This phenomenon was referred as water mass trapping effect (Matheis and Rothmayer 2003). The water trapping effect was numerical investigated (Rothmayer and Hu 2013, Rothmayer and Hu 2014, Wang and Rothmayer 2009). However, there is no direct experimental evidence to verify the numerical simulation results related to this micro-transient phenomenon.

In chapter 4, the DIP technique is used to achieve time-resolved measurements to quantify the transient behaviors of the wind-driven surface water flows over a rough surface in order to examine the water mass trapped effect due to the presence of the roughness array. The airflow boundary layers were measured by PIV technique to investigation the possible reasons of the water trapping effect. Both the water mass trapping effect and the transient behaviors of surface waves are quantified based on the quantitatively DIP measurement results (i.e., film thickness, water mass trapped ratio, surface wave frequency, wave length). The mass trapping effect was found mainly occurs near the back side range of roughness elements. The water mass transport behavior revealed from present experimental study will be used to validate the numerical simulation results reported in previous studies.

Wind-driven water runback flow significantly affects the final ice shape on the airfoil surface. Hansman and Turnock’s experiment showed that surface tension of a liquid significantly altered the glaze ice shape (Hansman and Turnock 1989). Kind (2001) claimed that one more parameter, i.e., Weber number based on the thickness of liquid film, should be considered as a critical scaling parameter in the glaze icing tunnel test. Anderson and Feo (2002) suggested that the non-dimensional water film thickness itself might be a critical dimension that affects the ice accretion. The scaling law of film thickness near the stagnation line was established by experimental study (Feo 2000) and theoretical analysis (Rothmayer 2003). Nelson (1995) showed that the water film thickness increases as flowing along a flat plate by a ¼ power law. However, in the previous studies, the film thickness on airfoil was measured by point measurement probes (e.g., conductance sensor in Feo's experiment). The scaling law of a film thickness at the water runback range has not yet been demonstrated experimentally. Rivulets stagnation and formation on an airfoil surface are important phenomena during the ice accretion process. Rivulet models were developed to predict the final rivulet configuration (e.g., rivulet width, rivulet formation location). However, those models are origin from the rewetting problem of a dry-patch in film flows. The dry-patch surround by film flow is a steady flow whereas the formation of rivulets during runback motion is an unsteady process. A time-resolved, whole field measurement is needed to disclose the transient behaviors of the water runback flow and the measurement results can be used to evaluate film thickness scaling laws and rivulet formation models.

In chapter 5, an experimental study was conducted to achieve water film/rivulets flow thickness measurements on a NACA0012 airfoil surface using the DIP system. The transient process of water runback was reconstructed with details. The formation of rivulets is found to be a time dependent process and highly relies on the initial flow structure. Film thickness scaling laws are evaluated by the time-average film thickness profile along chord length. The measurements results show that the film scaling law works well for the water runback range.

Chapter 6 presents the general conclusions of this dissertation.

References

Anderson DN, Feo A (2002) Ice-accretion scaling using water-film thickness parameters 40th AIAA Aerospace sciences meeting and exhibit. Reno, NV

Anderson DN, Ruff GA (1998) Measurement and correlation of ice accretion roughness 36th AIAA Aerospace science meeting and exhibit. Reno, NV

Ballough J (2007) Pilot's Guide: Flight In Icing Conditions. FAA, AC

Bragg MB, Gregorek GM, Lee JD (1986) Airfoil aerodynamics in icing conditions. Journal of Aircraft 23:76-81

Culkin JB, Davis SH (1984) Meandering of water rivulets. AIChE journal 30:263-267

Daerr A, Eggers J, Limat L, Valade N (2011) General mechanism for the meandering instability of rivulets of Newtonian fluids. Physical review letters 106:184501

Drenckhan W, Gatz S, Weaire D (2004) Wave patterns of a rivulet of surfactant solution in a Hele-Shaw cell. Physics of Fluids (1994-present) 16:3115-3121

Feo A (2000) Icing Scaling with Surface film thickness similarity for high LWC conditions. Madrid INTA (Instituto Nacional de Tecnia Aeroespacial) Report AE/PRO/4420/184/INTA/00 13pp

Gelder TF, Lewis JP (1951) Comparison of heat transfer from airfoil in natural and simulated icing conditions NACA TN 2480. NACA

Gorthi SS, Rastogi P (2010) Fringe projection techniques: whither we are? Optics and Lasers in Engineering 48:133-140

Hansman RJ, Barsotti MF (1985) Surface wetting effects on a laminar flow airfoil in simulated heavyrain. Journal of aircraft 22:1049-1053

Hansman RJ, Craig AP (1987) Low Reynolds number tests of NACA 64-210, NACA 0012, and Wortmann FX67-K170 airfoils in rain. Journal of Aircraft 24:559-566

Hansman RJ, Turnock SR (1989) Investigation of surface water behavior during glaze ice accretion. Journal of Aircraft 26:140-147

Hartley D, Murgatroyd W (1964) Criteria for the break-up of thin liquid layers flowing isothermally over solid surfaces. International Journal of Heat and Mass Transfer 7:1003-1015

Kim H-Y, Kim J-H, Kang BH (2004) Meandering instability of a rivulet. Journal of Fluid Mechanics 498:245-256

Kind RJ (2001) Assessment of importance of water-film parameters for scaling of glaze icing. 39th AIAA Aerospace sciences meeting and exhibit. Reno NV

Koochesfahani MM, Nocera DG (2007) Molecular tagging velocimetry. Handbook of experimental fluid dynamics:362-382

Le Grand-Piteira N, Daerr A, Limat L (2006) Meandering rivulets on a plane: A simple balance between inertia and capillarity. Physical review letters 96:254503

Liu Y, Waldman R, Hu H (2015) An Experimental Investigation on the Unsteady Heat Transfer Process over an Ice Accreting NACA 0012 Airfoil. 53rd AIAA Science and Technology Forum and Exposition, Kissimmee, FL.

Matheis BD, Rothmayer A (2003) Impact of underlying surface roughness on water transport AIAA 41st Aerospace sciences meeting and exhibit. Reno NV

McAlister G, Ettema R, Marshall J (2005) Wind-driven rivulet breakoff and droplet flows in microgravity and terrestrial-gravity conditions. Journal of fluids engineering 127:257-266

Murgatroyd W (1965) The role of shear and form forces in the stability of a dry patch in two-phase film flow. International Journal of Heat and Mass Transfer 8:297-301

Nakagawa T (1992) Rivulet meanders on a smooth hydrophobic surface. International journal of multiphase flow 18:455-463

Nelson JJ, Alving AE, Joseph DD (1995) Boundary layer flow of air over water on a flat plate. Journal of Fluid Mechanics 284:159-169

Olsen W, Walker E (1987) Experimental evidence for modifying the current physical model for ice accretion on aircraft surfaces.

Penn DG, de Bertodano ML, Lykoudis PS, Beus SG (2001) Dry patch stability of shear driven liquid films. Journal of fluids engineering 123:857-862

Ranaudo RJ, Reehorst AL, Bond TH, Batterson JG, O'Mara TM (1991) Effects of horizontal tail ice on longitudinal aerodynamic derivatives. Journal of Aircraft 28:193-199

Rothmayer AP (2003) Scaling laws for water and ice layers on airfoils 41th AIAA Aerospace sciences meeting and exhibit. Reno NV

Rothmayer AP, Hu H (2012) Solutions for two-dimensional instabilities of ice surfaces uniformly wetted by thin films. 4th AIAA Atmospheric and Space Environments Meeting. New Orleans, LN

Rothmayer AP, Hu H (2013) Linearized solutions of three-dimensional condensed layer films 5th AIAA Atmospheric and Space Environments Conference. San Diego, CA

Rothmayer AP, Hu H (2014) On the numerical solution of three-dimensional condensed layer films. 6th AIAA Atmospheric and space environments conference. Atlanta, GA

Shin J (1996) Characteristics of surface roughness associated with leading-edge ice accretion. Journal of aircraft 33:316-321

Tanner WF (1960) Helicoidal flow, a possible cause of meandering. Journal of Geophysical Research 65:993-995

Thompson BE, Jang J (1996) Aerodynamic efficiency of wings in rain. Journal of aircraft 33:1047-1053

Thompson BE, Marrochello MR (1999) Rivulet formation in surface-water flow on an airfoil in rain. AIAA journal 37:45-49

Waldman RM, Hu H (2015) High-speed imaging to quantify the transient ice accretion process on a naca 0012 airfoil. 53rd AIAA science and technology forum and exposition. Kissimmee, FL

Wang G, Rothmayer A (2009) Thin water films driven by air shear stress through roughness. Computers & Fluids 38:235-246

CHAPTER 2

DEVELOPMENT OF DIGITAL IMAGE PROJECTION TECHNIQUE TO MEASURE WIND-DRIVEN WATER FILM/RIVULET FLOWS

Abstract: In this work, an innovative 3D shape measurement technique digital image projection (DIP), which is an improvement of digital fringe projection (DFP) technique, is proposed for accurate and fast thin film/rivulet flow measurement. Instead of projecting a sinusoidal fringe pattern, a grid pattern is used in the DIP technique. Free surface shape is reconstructed by analyzing the projected grid points' displacements between a reference and measurement image. In comparison to the Fourier transformation based DFP system, The DIP system gives more accurate measurement result without rigid image quality requirement. This technique was applied to characterize of wind-driven thin film/rivulet flows that were formed in an open circuit wind tunnel. The film thickness and surface wave frequency were evaluated for variety of wind speeds and flow rates. The results show that this technique successfully revealed the dynamic motions of wind driven film/rivulets flows. Greater emphasis on the quantitative evaluation of the water film and rivulet flow over flat plate surface can be referred to the following chapter.

1. Introduction

Free surface flows are of interest in fundamental fluid dynamics research as well as in various practical applications. For example, Liu et al. (1995) performed experimental investigation to explore the three dimensional instabilities of film flows. Savelsberg et al. (2006) studied the interaction effect of free surface deformation and the turbulence channel flow. Kouyi et al. (2003) conducted experiment on the free surface of a storm overflow sanitation system. Pautsch and Shedd (2006) optimized a spray cooling system design by measuring the thickness distribution of FC-72 liquid film. Many experimental techniques have been applied to measure the thickness distribution of liquid free surfaces. Photo luminescent techniques have been successfully applied in measuring the free surface thickness in the past. The principle of this kind of technique is straight forward. The instantaneous film thickness is directly related to the fluorescent intensity by a calibration process. Liu et al. (1993) used a fluorescent imaging method to investigate the three dimensional instabilities of gravity-driven film flows. Johnson et al. (1997, 1999) also developed a fluorescent imaging system for detecting the dynamic moving contact line of film flowing over an inclined plate. Later, a laser induced fluorescence intensity method was used to measure wavy films (Lel et al. 2005, Schagen and Modigell 2007) and a heated liquid film (Chinnov et al. 2007). Recently, an LED fluorescence based imaging system had been applied to characterize thin films, droplets and rivulets (Hagemeier et al. 2012).

Stereo vision based techniques are frequently used in the surface reconstruction of open water flow. In those techniques, multiple cameras are calibrated to map the cameras’ view to a physical coordinate space. The free surface location is determined by find the matching pattern of image pairs by using Digital Image Correlation (DIC) calculation. Surface waves on a lake were evaluated with a stereo vision system (Wanek and Wu 2006). During the measurement, the reflections from surface ripples were used as the image patterns to compute the cross-correlation. However, this kind of image pattern does not exist on smooth water surface. Seeding the flow with particles is an alternate approach to achieve an acceptable image pattern correlation. Tsubaki and Fujita (2005) developed a stereo vision measurement technique to investigate the wavy water surface and ripples generated in a shallow water box. A random image pattern was projected onto white-colored water surface using a LCD projector. Two digital cameras were installed in a stereo configuration. The projected pattern was not directly used in measurement process but provided adequate information for the pattern points matching process. Turney et al. (2009) proposed a stereoscopic method (3D-IPIV) which simultaneously measured the topography and velocity of air-water interface. Fluorescent particles were used as air-water interface tracers to enable the cross-correlation calculation. Particle image sequences of each individual camera were used as PIV image pairs to obtain surface flow velocity. Gomit et al. (2013) presented a stereo-refraction method to evaluate a ship wake flow, which differs from the other stereo vision techniques that rely on reflected image patterns. In this method, the surface reconstruction was based on the analysis of apparent displacement between a reference and refracted images of the laser sheet viewed through a water-air interface from two cameras.

Density-based techniques have also been a useful tool for mapping the free surface deformation. Zhang et al. (1996) developed a color encoding system to measure free surface vibration by mapping the free surface slope. Scheid et al. (2000) reported a reflectance schlieren method to profile the local heated vertical falling film flow. Moisy et al. (2009) developed a free-surface synthetic schlieren method (FS-SS) and applied this method to reconstruct the wave pattern generated by impacting water droplets.

Besides optical methods, single point techniques like ultrasonic techniques (Li et al. 2010, Liu et al. 2014) and electrically-based methods (Burns et al. 2003, Yu et al. 2012) have long been used both in laboratories and in the open field. Those single point measurement techniques usually have higher time resolution and are robust in use.

Recently, the digital fringe projection (DFP) technique, with the advantages of high-resolution, whole-field 3D reconstruction of objects in a non-contact manner at video frame rates (Gorthi and Rastogi 2010), has been increasing use in free surface thickness measurements. Its applications include vertex shape reconstruction at a free surface (Zhang and Su 2002), free surface measurement of sanitation system storm overflow (Kouyi et al. 2003), evaluation of surge’s free surface variation with time related to dam-break (Cochard and Ancey 2008) and water-wave trapped modes investigation (Cobelli et al. 2011). All of those investigations used Fourier transform profilometry (FTP) system to reconstruct the shape of free water surface. This method requires projecting a precise sinusoidal fringe pattern, which is very hard if not impossible to achieve on a liquid surface. Additionally, the two-dimensional phase unwrapping integration is sensitive to the integral path and tends to accumulate errors. Shadowed regions appear when the highly distorted liquid surfaces block the projector light path or the camera view. The phase information will totally lost in the shadowed region. Hence, it is easily to contaminate the measurement result even a proper phase unwrapping algorithm is used to handle the problem.

In this paper, a novel digital image projection (DIP) technique is used to measure free surface deformation of wind-driven thin water films/rivulets. In contrast to directly projecting sinusoidal patterns to 3D objects surface, a crossed line grid is used to reconstruct the 3D shape. The grid points' displacements between a zero height reference image and the deformed liquid surface image are calculated by using cross-correlation. The relationship of grid displacement and object height is mapped by a calibration process. In order to demonstrate the advantages of the digital image projection measurement system, both the DIP technique and FTP based DFP measurement technique are used to reconstruct a spherical cap shape object with known profile. The result shows that the DIP system is more accurate and insensitive to image quality.

The other particular interest of present paper is the water-air interface reconstruction of the wind-driven thin water film flows. Although there are some theoretical and numerical investigations on the shear stress-driven water film flows (Boomkamp et al. 1997, Rothmayer et al. 2002, Wang and Rothmayer 2009), experimental investigations on wind-driven thin film flows are seldom found (Marshall and Ettema 2004, Shaikh and Siddiqui 2010). In this study, DIP measurement system was applied to measure the free surface of thin water film flows, which were generated by a small wind tunnel using different airflow velocities and different water flow rates. The thin film deformation process and traveling wave frequency were quantitatively studied.

This chapter is organized in six sections as follows. Section 2 describes the principles of digital image projection technique. Section 3 compares the measurement accuracy of our DIP technique with FTP based DFP method. Section 4 illustrates the complete experiment set up for wind-driven thin water film flow thickness measurement. Section 5 shows the thin water film flows measurement results, such as film flow instantaneous and average thickness, traveling wave frequency, and wave deformation process. Finally, section 6 presents conclusions.

2. Principles of the measurement method

2.1 Key ideas of digital image projection (DIP) technique

The basic principle of the digital fringe projection technique had been illustrated by the literature reviews (Gorthi and Rastogi 2010, Zhang 2010). A typical DFP system contains a projection unit, an image capture unit, and a data processing unit. The projector projects a known pattern onto the test object. Due to the 3D geometry of the object, the projected image will appear distorted in the camera view. By proper processing algorithm to compare the distorted image pattern with the reference image, the three dimensional profile of the object can be reconstructed.

The key ideas of DIP technique are to replace the sinusoidal pattern with a grid pattern and to avoid the complex phase processing by use of cross-correlation calculation. Modern projectors provide a great flexibility in projecting any kind of fringe patterns. This feature permits researchers to design variety of patterns and associated processing algorithms for 3D shape profile reconstruction (Gorthi and Rastogi 2010). Our new cross-correlation based system measurement techniques can be seen as a development of novel projection pattern and corresponding novel processing algorithm. In addition, the new technique is applied to wind-driven film/rivulets flow free surface deformation measurement problems.

The ideas of DIP technique are inspired by molecular tagging velocimetry (MTV) technique. For MTV, measurement of two components of the velocity field relies on a grid of intersecting laser lines that are generated by a pair of crossing laser beams. This kind of illumination provides spatial gradients along two orthogonal directions (Fig. 2-1a). Gendrich and Koochesfahani (1996) presented a spatial image correlation method that processes the displacement vector of the tagged grid points with high accuracy. As the displacements of fringes pattern are similar to molecular tagging velocimetry image deformations, it is straightforward to replace the projected fringe pattern with projected grid lines pattern (Fig. 2-1b) and process the displacement vectors of the grid pattern with the same algorithm developed by Gendrich and Koochesfahani (1996).

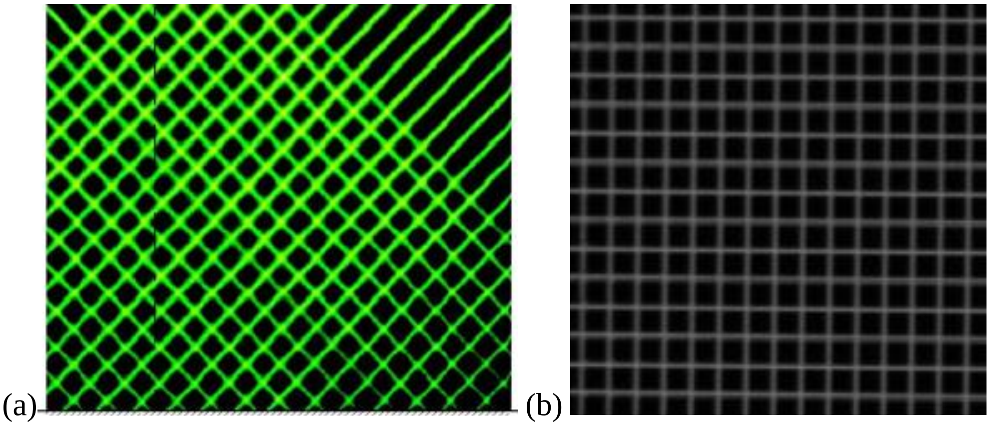

Figure 2-1 *(a) Typical MTV image grid pattern(Gendrich et al. 1997). (b) Typical DIP image grid pattern*

Figure 2-2 illustrates the flow chart of typical DFP measurement technique and DIP technique. As discussed above the setup of the DIP technique has the same projection unit and image recording unit as DFP technique. However there are four steps for a DFP measurement: sinusoidal pattern generation, phase detection, phase unwrapping and phase to height conversion. In order to get high quality measurement, all four steps must be treated properly. For example, nonlinear gamma correlation may be required in sinusoidal pattern generation step and integral path must be selected to avoid discontinuity area in phase unwrapping process. On the other hand, there are three steps for DIP measurement: grid pattern generation, displacement vector calculation, and displacement to height conversion. Unlike the sinusoidal pattern, no intensity relationship is required by grid patterns. Hence, high accuracy measurements can be achieved even when the projected pattern is distorted. Furthermore, the grid points are independent from each other. Therefore, local poor image quality does not influence the whole field measurement. In DIP technique, the chain of image distortion to phase difference and then convert to 3D object height is simplified to image distortion displacement to object height process. This makes the measurement principle much easier to understand. The sophisticated phase processing is replaced by spatial cross-correlation. According to Gendrich and Koochesfahani (1996), the cross-correlation is insensitive to signal noise as long as the image has sufficient contrast (image contrast>50). As this feature was obtained by simulations of different illumination conditions, this benefit still applies for the DIP technique which means high quality measurement will be easier to achieve. The other benefit of cross-correlation calculation is it avoids the complex and difficult phase unwrapping problem. 2D unwrapping is the final and most challenging step in the phase extraction process. One difficulty of phase unwrapping is how to different between genuine phase and false phase. The other difficulty is the accumulative nature of unwrapping process. One false phase may propagate throughout the test image. Ghiglia and Pritt's (1998) book clear explain the difficulties in solving this problem.

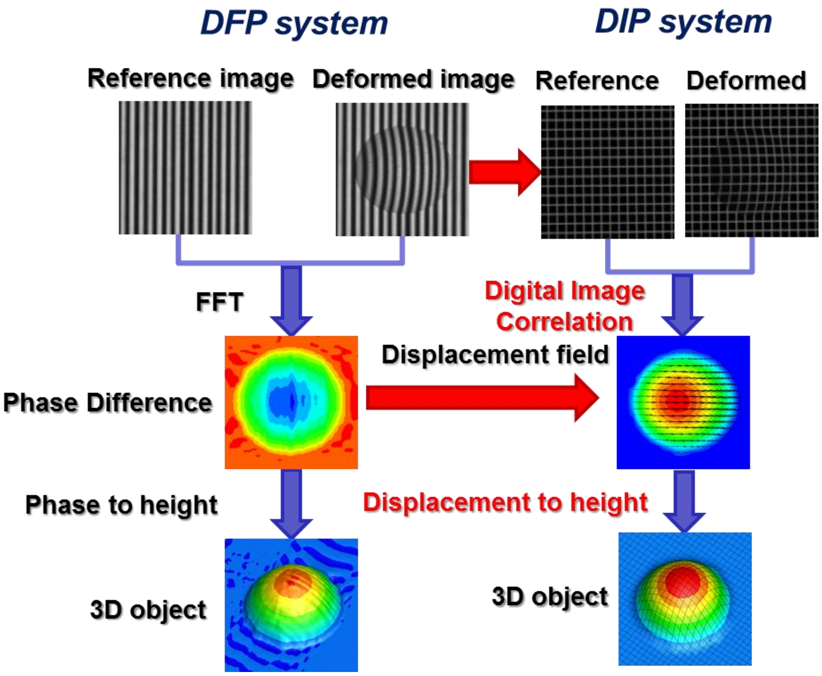

Figure 2-2 *Comparison of DFP system and DIP system*

2.2 Principle of the digital image projection method

Figure 2-3 illustrates the schematic of the optic principle of digital image projection (DIP) technique. To conduct a DIP measurement, a camera and a projector are located at same height s and separated by a distance d. An image of a reference plane without the measurement object is then recorded. 3D object image will be recorded as measurement image. Because of the 3D shape of the object, the projected grid will distort and grid points on the 3D object surface will translate a distance. Point M denotes the pupil center of a projector and point N denotes the pupil center of a camera. The projector projects a grid point D on the 3D object surface. Supposing that there is no 3D object in the reference plane, from projector's perspective, grid point D should be projected to grid point A on the reference plane. From the camera's view, point D is the same pixel as point C in the reference image. The grid deformation displacement between point D and point A then can be expressed as:

$$\overline{CA} = P_r(\mathrm{C}) - P_r(A) = P_m(D) - P_r(A) \tag{2.1}$$

Where $\overline{CA}$ denotes grid displacement, P denotes the grid point location, subscript r denotes the reference image, and subscript m denotes the measurement image. Displacement $\overline{CA} = P(D) - P_r(A)$ can be obtained by spatially correlating the reference image with the deformed object image.

Because the triangle ADC is similar to triangle MDN, the relationship between the object height h and the deformed grid displacement $\overline{CA}$ can be represented as:

$$\frac{d}{\overline{CA}} = \frac{s - h(i,j)}{h(i,j)} = \frac{s}{h(i,j)} - 1 \tag{2.2}$$

In equation (2.2), subscript i, j denotes grid point location index on the deformed measurement image. The maximum height of measurement object is much smaller than the camera-projector plane height s, so that $\frac{s}{h(i,j)} \gg 1$.Note that s and d are constants determined by the configuration of the experiment. The equation can be simplified as:

$$h(i,j) = \frac{s}{d}\overline{CA} = K(i,j)\overline{CA} \tag{2.3}$$

Equation (2.3) defines a linear relationship between distorted displacement $\overline{CA}$ and 3D object height. K denotes the displacement-to-height conversion factor, and should be a constant value throughout the measurement field of view if the camera and the projector are at the same height. However, in reality, the projector height can not equal to the camera height exactly (the location of CCD sensor and the location of sensor within the projector are unknown). Even this height discrepancy only slightly affects the measurement accuracy; a displacement to height conversion map is used to replace a single conversion value. Once the grid points displacement vector field and the displacement to height conversion map K are determined, the 3D shape can be reconstructed by multiplying them together.

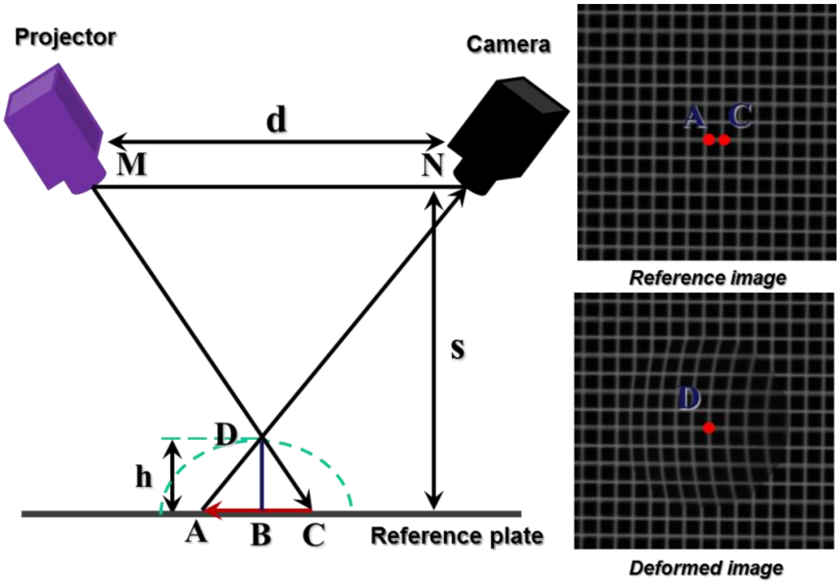

Figure 2-3 *Optic principle of DIP measurement technique*

2.3 Principle of the digital image correlation method

Digital image correlation (DIC) algorithms are widely used in particle image velocimetry (PIV) (Adrian 1991, Raffel et al. 1998). This method is used to compute and identify the peak correlation coefficient of a two-image sequence. As discussed in section 2.1, the spatial correlation algorithm developed by Gendrith and Koochesfahani (1996) is selected as the cross-correlation method used in digital projection measurement technique. Figure 2-4 shows the sketch of correlation algorithm. The small red window (I_r) refers to the source interrogation window located in the grid centers of reference image (image of zero height plane). Correspondingly, the small blue window (I) refers to the roam interrogation window in the measurement image. The big rectangular window is the searching window. The normalized correlation coefficient is computed by following formula:

$$R(r,s)=\frac{\sum_i\sum_j(I_r(i,j)-\overline{I_r})(I(i+r,j+s)-\overline{I})}{\sqrt{\sum_i\sum_j(I_r(i,j)-\overline{I_r})^2(I(i+r,j+s)-\overline{I})^2}} \tag{2.4}$$

Where I and I_r represent the picture intensity within interrogation window of reference image and measurement image respectively, $\overline{I_r}$ and $\overline{I}$ are the corresponding mean intensity values of I_r and I, $R(r,s)$ denotes the correlation coefficient , and (r,s) denotes the searching vector. The peak correlation coefficient $R(r,s)$ location determines the displacement vector $(\Delta x,\Delta y)$, where x direction denotes the axis parallel with camera-projection connection line and y normal to x direction.

According to Gendrith and Koochesfahani (1996), sub-pixel accuracy can be achieved using a polynomial fit to the correlation coefficients. In this work, A 4th order polynomial fitting with a 5×5 pixels fitting window was used. The fitting function $F(i,j)$ is expressed as:

$$F(i,j)=\sum_{n=0}^{4}(c_{n,0}i^n j^0+c_{n,1}i^{n-1}j^1+...+c_{n,n}i^0 j^n) \tag{2.5}$$

In equation (2.5), (i,j) denotes the local coordinate within fitting window. The origin point of the i,j coordinate locates at the local cross line intersections of a reference image. $c_{n,0},c_{n,1}...c_{n,n}$ denote fit coefficients.

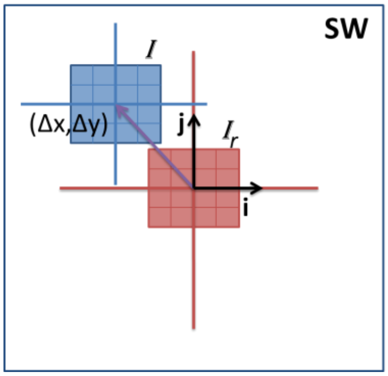

Figure2-4 *Sketch of correlation algorithm*

A typical reference and measurement images are shown in Fig. 2-5. The reference image was generated by projecting cross lines grid onto the substrate (Fig. 2-5a). An image identification algorithm was applied to recognize the cross line intersections in the reference image (Fig. 2-5b). To maximize the signal to noise ratio, the reference interrogation windows are centered at the grid points. Cross-correlation calculation was then performed to get the grid displacements, which is shown in Figure 2-5c.

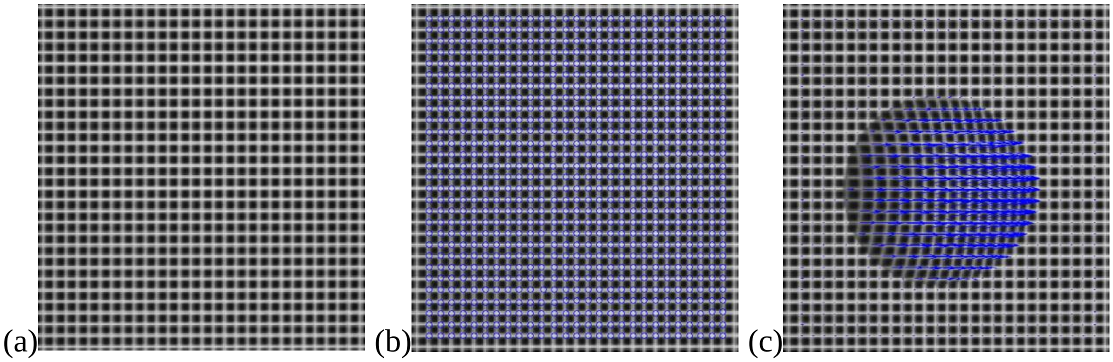

Figure 2-5 *Typical DIP images and resultant deformation vector field. (a) Reference image. (b) Cross line intersection detection image. (c) Calculated grid points displacement vector field*

2.4 Displacement to height conversion map

The map of displacement-to-height coefficients can be determined by calibrating the DIP system. Figure 2-6 illustrates the schematic of the calibration set up. To conduct a calibration, a camera and a projector are roughly set at same height. The camera is set to be normal to the calibration target so that no camera calibration is need.

Equation (2.3) represents a linear relationship between deformation displacement $\overline{CA}$ and object height h. For current setup, the Y direction displacements approach zero. Thus X direction displacement is used to map the coefficients:

$$h(i,j) = K(i,j)\Delta X(i,j) \tag{2.6}$$

To accurately calibrate the DIP system, a vertical translation stage with micrometer is used to precisely adjust the vertical location of the calibration target. The calibration target is then moved to 8-10 heights. Image of grid pattern on the calibration target at each individual height is recorded. The initial plate location is selected as the zero height and its grid pattern image is taken as the reference image. Other images are spatial correlated with the reference image to obtain the grid points displacements. The linear displacement to height coefficients map is then determined by the least square fitting method.

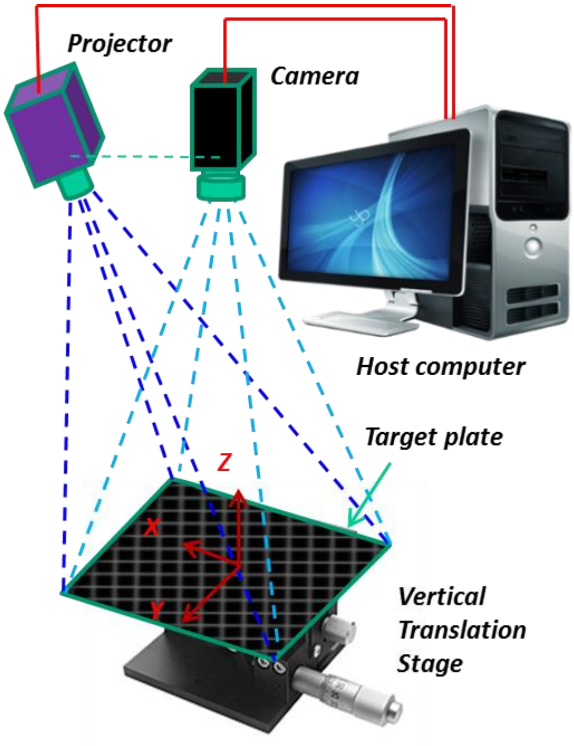

Figure 2-6 *Sketch of DIP displacement to height calibration setup*

3. Technique verification

Currently, most of the free surface measurements using DFP system are based on the Fourier transform profilometry method. In this section, we will compare the DIP method with the FTP based DFP method and demonstrate that the DIP system is advantageous for accurate 3D shape reconstruction. The sinusoidal fringe patterns, which are used in FTP based DFP system, are obtained using defocused binary patterns (DBP). The defocused intensity profile is shown in Fig. 2-7. The used pattern was verified with a sinusoidal fit to guarantee a high quality sinusoidal pattern was used in the comparison (Fig. 2-7b). However, there are still phase shifts and intensity differences between the projected image pattern and best-fit sinusoidal pattern (Fig. 2-7b). The Fourier transform method was used to obtain the wrapped phase map. For details about the data processing method, including phase separation algorithm, and high-order and fundamental frequency noise reduction, refer to our previous paper (Wang et al. 2012).

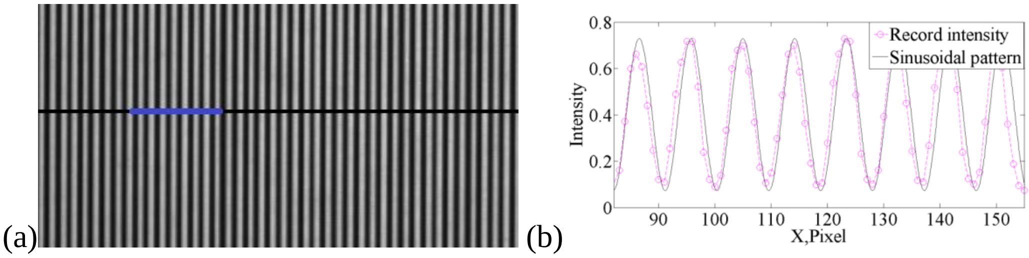

Figure2-7 *(a) Projected image pattern. (b) Comparison of normalized image intensity with sinusoidal fitting profile, intensity value from the blue line of left image*

During the experiment, a Dell DLP projector (M109S) was used to project the defocused binary fringe patterns and grid patterns onto a spherical cap model with known profile. A CCD camera (DMKBU2104) with a Pentax C1614-M lens (F/1.4, f=16mm) was used for image acquisition. A digital pulse/delay generator (Standard research system, Model DG535) was employed to synchronize the CCD camera with the projector using the VGA vertical sync signal. The camera has a maximum frame rate of 60frames/s with a resolution of 640×480. The camera exposure time was set at 1ms. The projector has a resolution of 858×600. The spherical cap has a bottom circle radius of 10mm and 4mm height. This model was 3D printed with a rapid prototyping machine with typical accuracy of 20µm. To improve the diffuse reflectivity of the surface, the test model was coated with flat white paint.

Calibrations were performed to determine the phase-to-height coefficients map $K_1(i, j)$ for the FTP based DFP system and to determine the displacement-t- height coefficients map $K_2(i, j)$ for the DIP system. The results are shown in Figure 2-8. As seen from the figure, the phase-to-height conversion coefficients $K_1(i, j)$ are varied with each fringe, whereas the displacement-to-height conversion coefficients $K_2(i, j)$ are varied along the camera-projector direction. In Figure 2-8, (xi, yj) represents the image coordinate system.

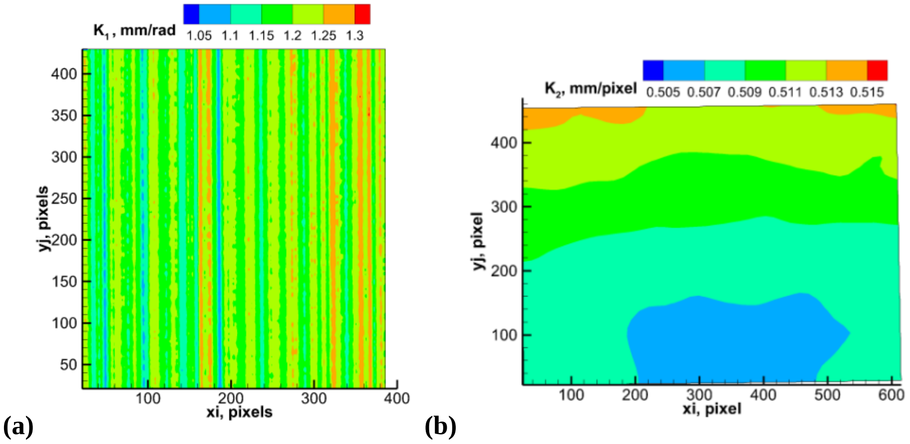

Figure2-8 *Phase to height and displacement to height coefficient map: (a) Coefficient map for the FTP-based system; (b) Coefficient map for the DIP system*

Table 1 shows the average measurement errors and standard deviation of the two techniques. Note that the average measurement error was calculated from absolute differences between measured height distributions and the design shape of the spherical cap model. In addition, we only accounted for the measurement points on the spherical cap object surface. The manufacturing errors of the test model were not taken into account during this work. The average measurement error of the FTP-based DFP system is 0.12mm with a corresponding standard deviation of 0.08mm. The average measurement error of the DIP system is only 0.04mm with a corresponding standard deviation of 0.04mm. This shows that the DIP system is much more accurate than the FTP-based measurement system. The measurement errors are halved by DIP system.

Table1 *Measurement error comparison of DFP and DIP*

	Mean error (mm)	Standard deviation of errors (mm)
FTP based DFP	0.12	0.08
DIP	0.04	0.04

Figure 2-9 shows the measured height distribution of the spherical cap model by FTP-based DFP system. Figure 2-9a displays that spherical cap shape was not precisely reconstructed. Distinct, uneven, fringe-shaped roughness is seen in the 3D reconstructed surface. Figure 2-9b shows the measurement errors distribution of the DFP system. As shown in Figure 2-9b, the measurement errors are also varied by individual fringe. The measurement error ranges from -0.5mm-0.5mm. Those measurement errors are mainly caused by the discrepancy between the faultless sinusoidal intensity pattern and the experimental image pattern intensity profile. This inconsistency could be induced by many sources including projector interpolation blur (commercial projector usually provides higher resolution than its clip), non-uniform reflectivity of the object plane, camera lens distortion, etc.

Figure 2-10 shows the measurement surface reconstruction and errors from the DIP system. As shown in Figure 2-10a, the reconstructed 3D object shape is much smoother with only some tiny distortions on the boundary of the test object. Figure 2-10(b) presents that the measurement error of our novel system is generally in the range -0.1mm-0.15mm. Some relatively large error variances appear at the edge of the spherical cap. Due to the nature of correlation calculation, a single measurement point is the spatial-average of an interrogation window (7×7 pixels). For those boundary points whose interrogation windows are partly on the substrate and partly on the 3D object surface, measurement errors cannot be avoided. Because of the spatial filtering of the correlation window, the DIP technique decreases the measurement's spatial resolution compared with FTP based DFP system. The measurement results indicate that, at a cost of decreased spatial resolution, the new technique can conduct high accuracy measurements without rigid picture quality restrictions.

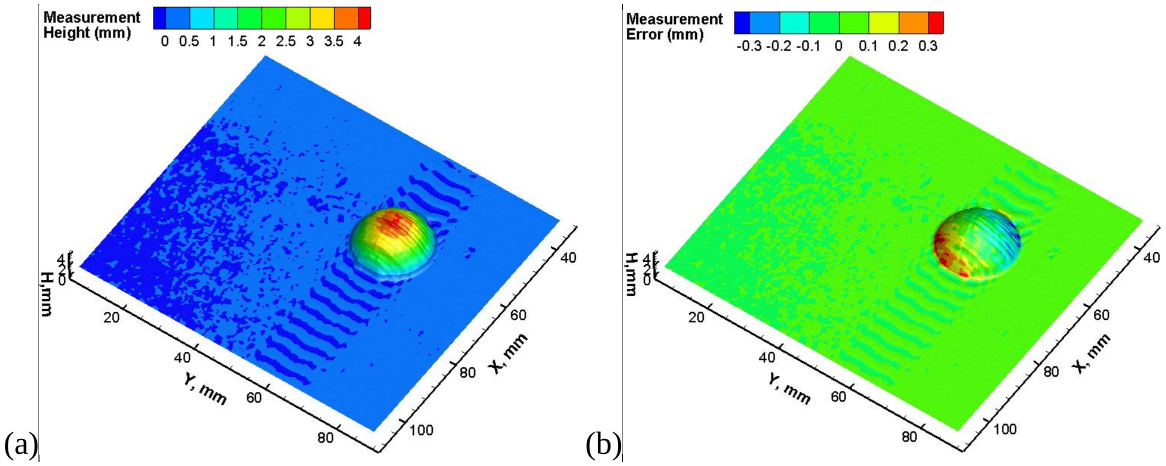

Figure 2-9 *Measurement results of FTP-based DFP system. (a) 3D shape reconstruction for R10mm, H4mm spherical cap model. (b) Measurement errors distribution of spherical cap model*

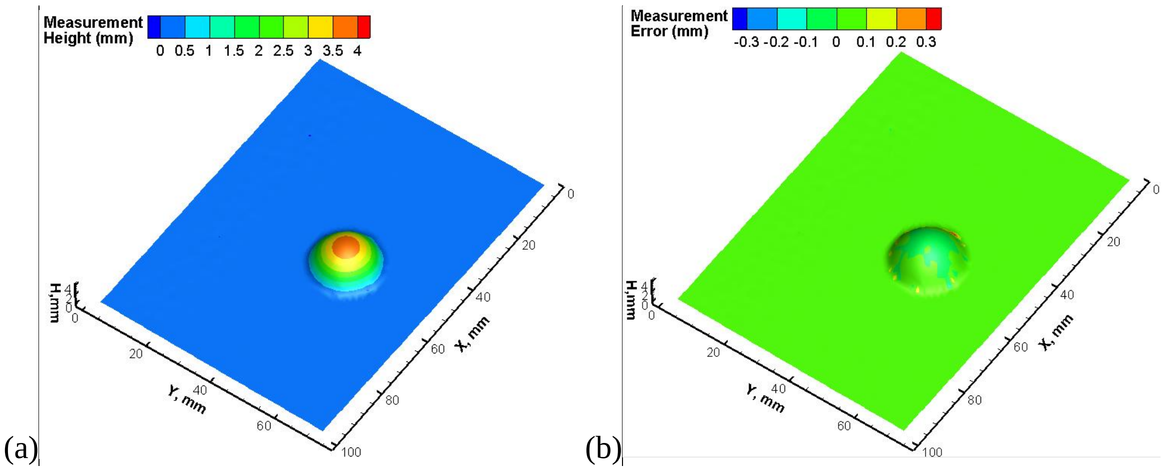

Figure 2-10 *Measurement results of DIP system. (a) 3D shape reconstruction for R10mm, H4mm spherical cap model. (b) Measurement errors distribution for spherical cap model*

4. Experiment set up and procedure

Figure 2-11 illustrates the the experiment setup for wind-driven thin water film flows thickness measurements. The DIP system configuration is the same as the verification experiment configuration. Camera frame rate was set to 30FPS with a 2ms exposure time. The field-of-view of the CCD camera is approximately $9cm \times 11cm$. The projected grid size and the interrogation window size is 7×7 pixels. A micro digital gear pump (Cole-parmer 75211-30) and a small water tank were used to produce two steady water flow rate of 100ml/min and 200ml/min. In order to generate a uniform film flow, an array of holes were drilled in the substrate that was coated with flat white paint. The width of holes array was measured D=6cm, the holes were spaced 5mm apart, the hole diameter was measured 2mm (Fig. 2-12). The overall dimension of substrate was 25cm×15cm. It should be noted that, during the experiment, water may run backward due to the surface tension force under low wind speed conditions (10m/s). A wedge edge plane may solve the problem in the future work.

The experiments were conducted in an open circuit low-speed wind tunnel. The wind tunnel has a plexiglas test section with dimension of 20×14×30cm (W×H×L). Three different wind speeds 10m/s, 15m/s and 20m/s were used to investigate the behaviors of the thin film flow. Flat white latex paint was added to the water to enhance the diffusive reflection from the liquid surface. Note that latex paint affects the surface tension of the water, and as a result, the film behavior in this work is different with pure water film flows. Some other coloring pigments may be used in the future work to avoid film flow contamination (Przadka et al. 2012). The other limitation of current experiment is that we did not investigate the errors caused by the diffusion effect as the projector light ray enters into the water surface.

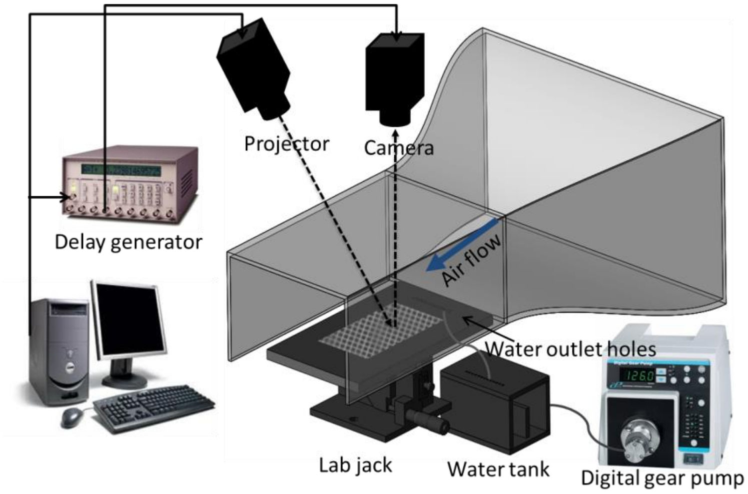

Figure 2-11 *Experiment set up for wind-driven thin water film/rivulet flow test*

The film flow measurement procedure was simple: first let the water overflow the substrate under test flow rate condition. Next adjust the wind speed to 20m/s to generate a uniform, thin water film flow. Then further reduce the wind speed to the test condition (i.e., 15m/s, 10m/s). For each measurement, 600 images (20s) were collected under steady-state condition. Cross-correlation analysis of each snapshot with the reference image was performed and the image deformations were interpolated onto a regular grid. The measurement results are normalized by the width of the width of hole array. L denotes the distance that is away from the water holes array. W denotes the distance that is away from the centerline of the test plane along flow direction (Fig. 2-12).

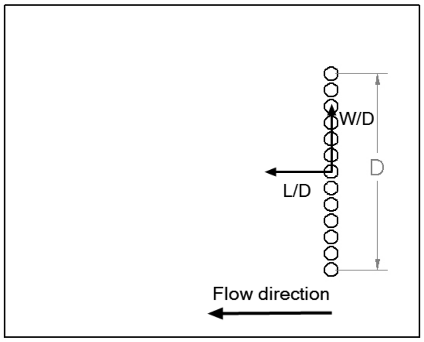

Figure 2-12 *Schematic diagram of water outlet holes array and coordinate*

5. Results and discussion

Figure 2-13 shows the instantaneous and ensemble-average thin water film flow thickness distributions for the air speeds $U_\infty = 10m/s - 20m/s$ and at the flow rate $q = 16.7ml/min/cm$. As displayed in Fig. 2-13(A), the instantaneous film shape was almost the same as the $U_\infty = 10m/s$ time-averaged film shape. The water-air interface behaved like a calm water surface, which demonstrates that the surface tension is the dominant force and resists the water-air interface displacement under low wind speed conditions. Water surface raise was observed near the end of the measurement field (more clearly in Fig. 2-15). It is because the surface tension at the vertical edge of the substrate end will block the film flow. As the flow speed increased to $U_\infty = 15m/s$, water traveling waves were generated from the disturbance of air shear stress. We found that quasi-regular waves would emerge near the water outlet holes and gradually attenuate as they traveled downstream. We did identified quasi-period waves using spectral analysis, which be discussed later. The average thickness distribution for this case is generally the same with other flow speeds and flow rate cases except the $U_\infty = 10m/s$, $q = 16.7ml/min/cm$ one. The thickness distribution was a generally symmetric distribution with respect to the centerline and it decreased along flow direction. Figure 2-13(C) shows that water waves break into several segments at the very beginning of the thin film flow when the airflow velocity reaches 20m/s. Those waves further breakup and evolve into small pieces as they flow downstream. This indicates the air shear stress dominated the flow. The time-average thickness distribution exhibits a perfect thin film shape like a flat plate.

Figure 2-14 shows the film thickness distribution under the flow rate $q = 33.3ml/min/cm$. Compared with flow rate $q = 16.7ml/min/cm$ cases, the disturbances from the water outlet holes was much more severe. Because of higher flow rate and flow rate unevenness of each hole, the water-air interfaces displayed an irregular surge shape in the region close to water outlet holes (L/D<0.5). For the wind speed $U_\infty = 10 m/s$ case, in the range L/D>0.75, the thin water film was generally flat (Fig. 2-14A). For wind speeds $U_\infty = 15 m/s$ and 20m/s cases, in the range L/D>0.75, the displayed instantaneous water-air interfacial waves characteristics were roughly the same with the $q = 16.7 ml/min/cm$ ones. The flow rates of individual holes might be different, as a result, the time-averaged results showed that the film thicknesses were no longer uniform along the water holes' array direction. However, the time-averaged film thicknesses distribution still exhibited a level surface shape. Both the instantaneous and ensemble-averaged results indicate that the flows are somewhat regulated by the combined effects of water surface tension, gravity force and air shear stress force.

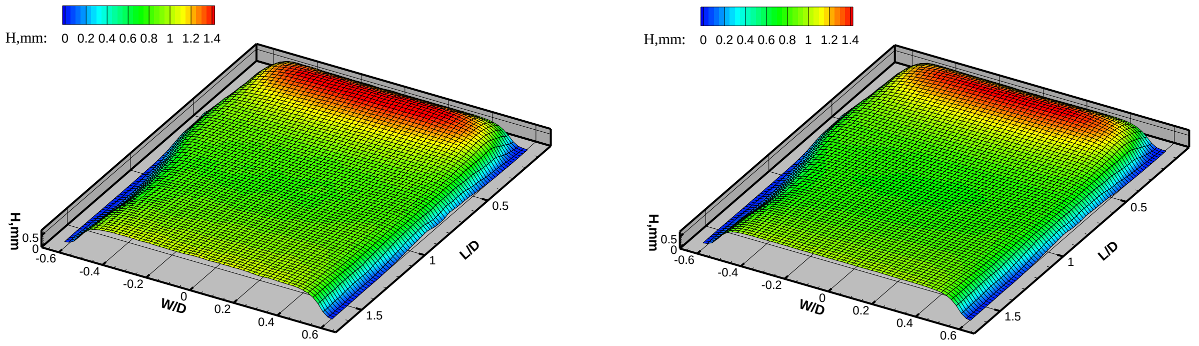

a. Instantaneous result

b. Ensemble-average result

A. $U_\infty = 10 m/s$

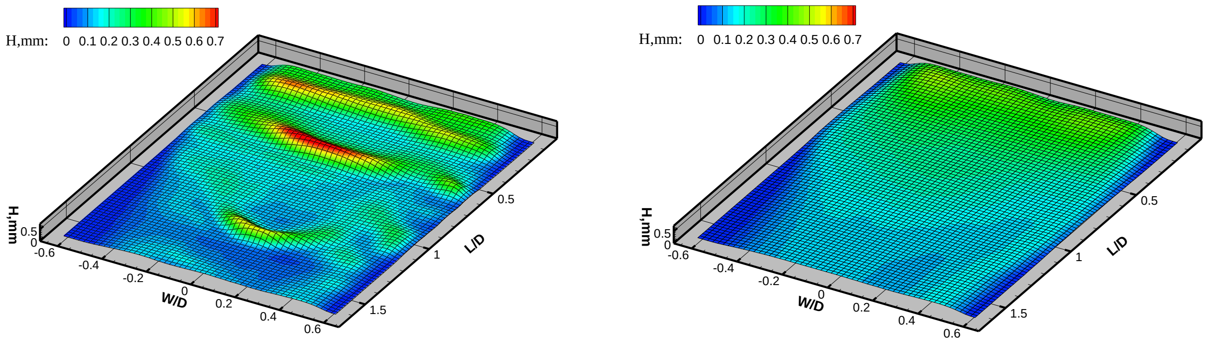

a. Instantaneous result

b. Ensemble-average result

B. $U_\infty = 15m/s$

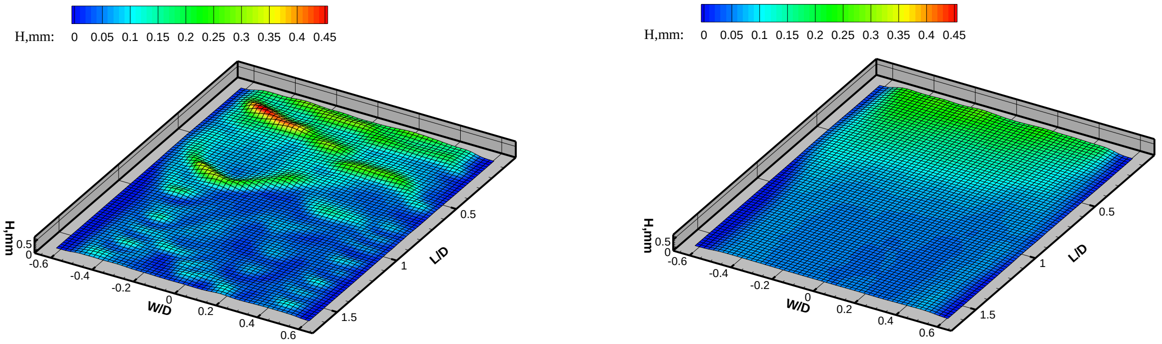

a. Instantaneous result b. Ensemble-average result

C. $U_\infty = 20m/s$

Figure 2-13 *DIP measurement results of different wind speeds at flow rate* $q = 16.7ml/min/cm$

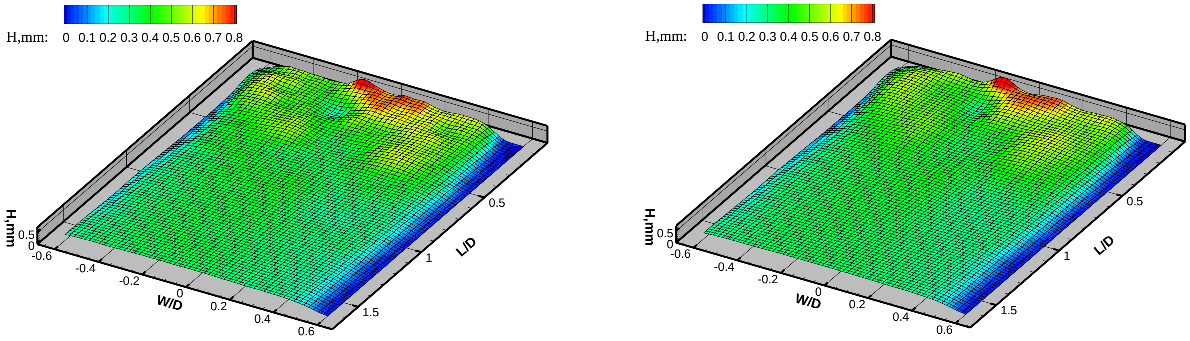

a. Instantaneous result b. Ensemble-average result

A. $U_\infty = 10m/s$

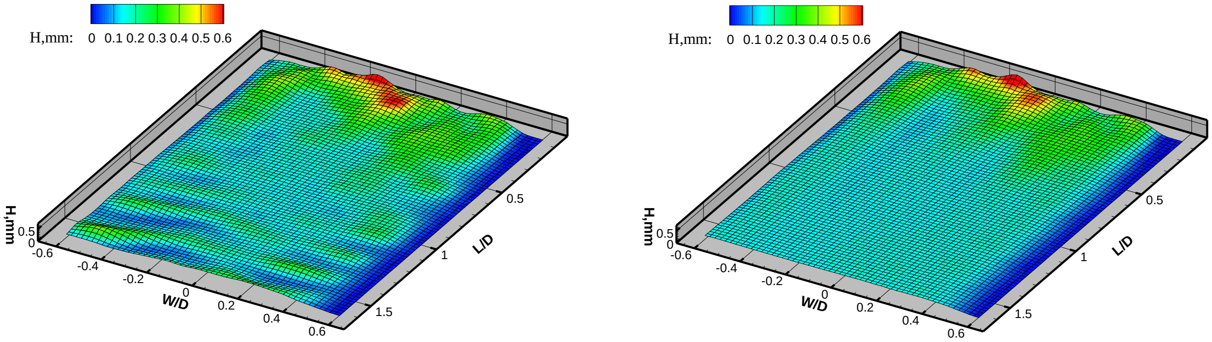

a. Instantaneous result b. Ensemble-average result

B. $U_\infty = 15m/s$

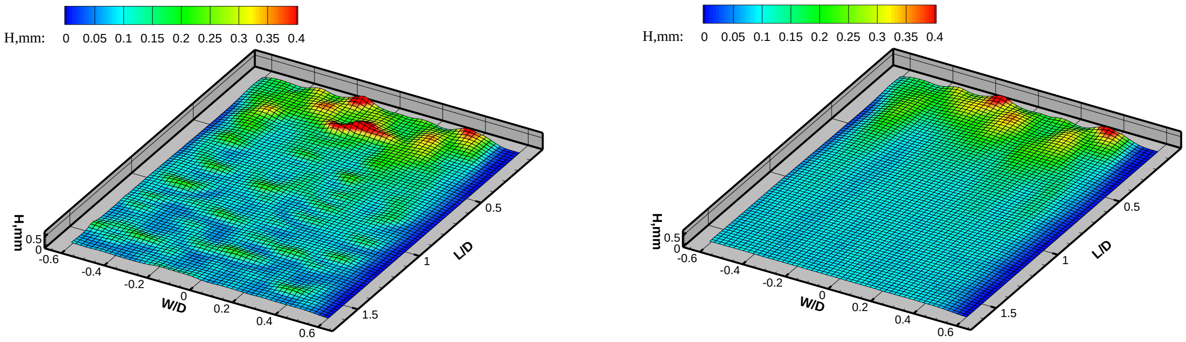

a. Instantaneous result

b. Ensemble-average result

C. $U_\infty = 20m/s$

Figure2-14 *DIP measurement results of different wind speeds at flow rate* $q = 33.3ml/min/cm$

Figure 2-15 shows the ensemble-average film thickness profiles at the centerline of the film flow under the different wind speeds and flow rates. Seen from the figure, the profiles of the thin water film generally first increased and before decreasing to a steady height with the exception of the $q = 16.7ml/min/cm$, $U_\infty = 10m/s$ case. The gradient of the curves varied slightly with wind speeds and flow rates. Seen from Fig. 2-13B, the water-air interfacial waves' amplitude of case $q = 16.7ml/min/cm$, $U_\infty = 15m/s$ were much higher. The film flows' thicknesses of larger flow rate cases are much higher than the thickness of the lower flow rate cases within the range close to water outlet hole. Average thin film thicknesses vary from 0.05-0.35mm with decreasing thickness as wind speeds and water flow rates increase. Those time-averaged film thickness profiles can be considered as a reference of two dimensional undisturbed film flow water-air interfaces.

Spectral analysis was performed to reveal the water waves evolution for case $U_\infty = 15m/s$ and $q = 16.7ml/min/cm$. Three points (L/D=0.25, W/D=0), (L/D=0.75, W/D=0) and (L/D=1.25, W/D=0) were chosen to do Fourier transform calculation. As mentioned above, our camera speed was set to 30FPS and 600 images (20s) were captured for each case, the theoretical maximum identifiable frequency is 15Hz with a resolution of 0.05Hz. An interpolation calculation was used to get film thickness at those three points. As shown in the Fig. 2-16A, the dominant frequency at point (L/D=0.25, W/D=0) is 7Hz. If there are no damping effects, the wave frequency will be preserved as the waves propagate to downstream. However, the dominant frequency at point (L/D=0.75, W/D=0) is 3.5Hz (Fig. 2-16B) and there is no obvious dominant frequency at point (L/D=1.25, W/D=0) (Fig. 2-16C). We examined the animation of our measurement result and found that the water wave amplitude will attenuate as it travels downstream. Only one out of two waves can reach point (L/D=0.75, W/D=0) without significant reduction of wave amplitude. The waves that reach point (L/D=1.25, W/D=0) occurred randomly, which induces several low frequency signals in the Fig. 2-16C.

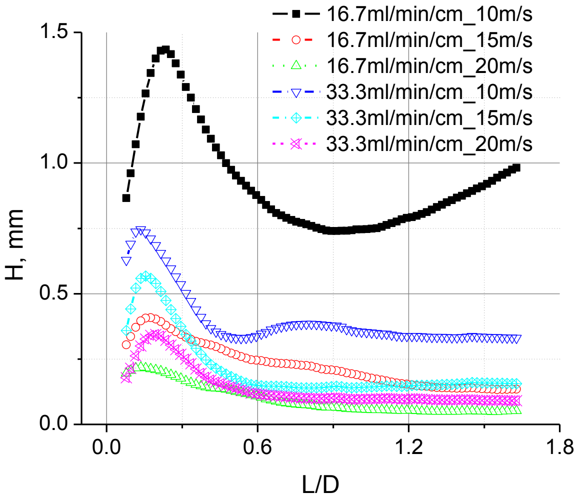

Figure 2-15 *Ensemble-averaged thin water film thickness profiles at film center line W/D=0*

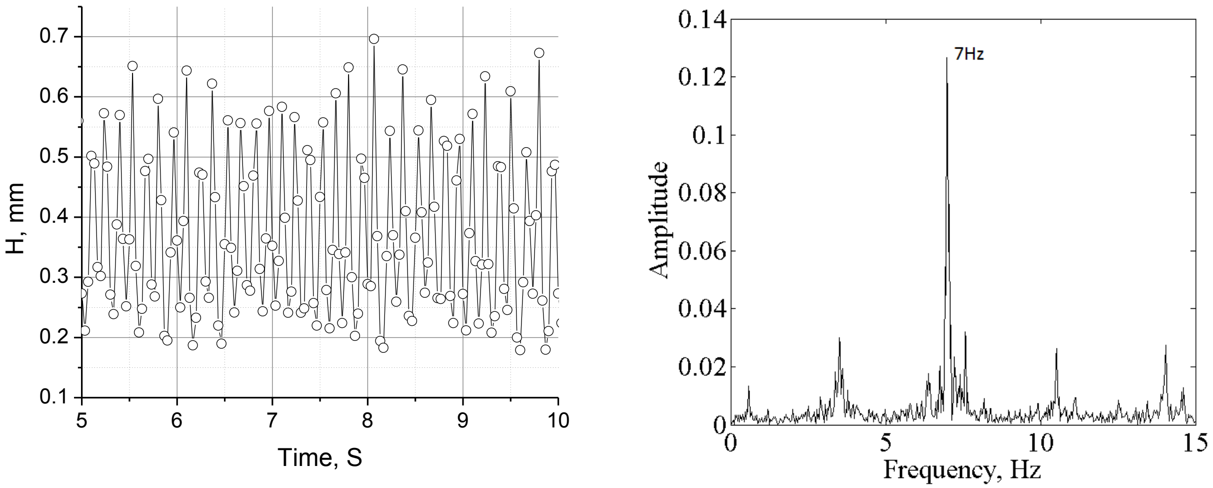

a. Time history of film thickness

b. Frequency spectrum

A. L/D=0.25D, W/D=0

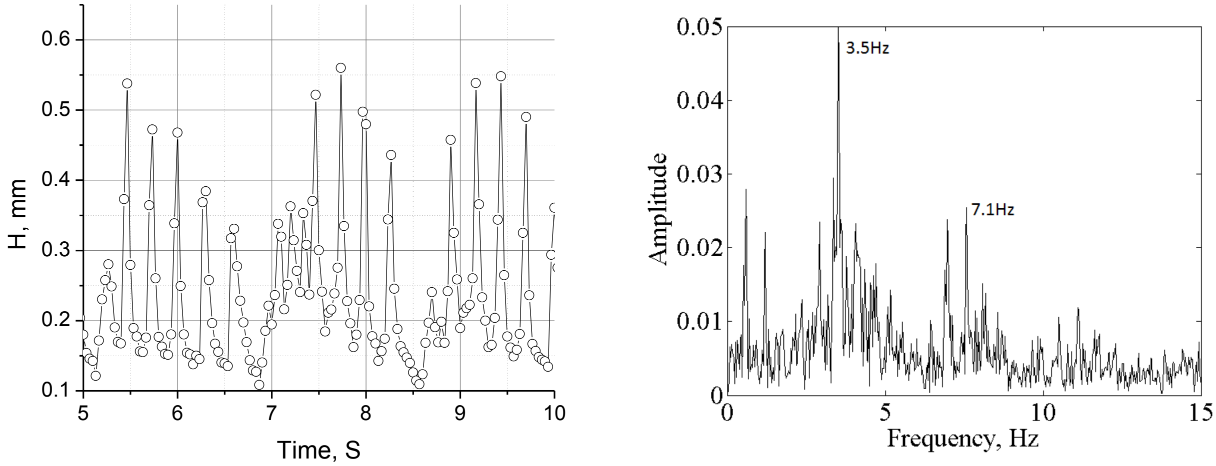

a. Time history of film thickness

b. Frequency spectrum

B. L/D=0.75D, W/D=0

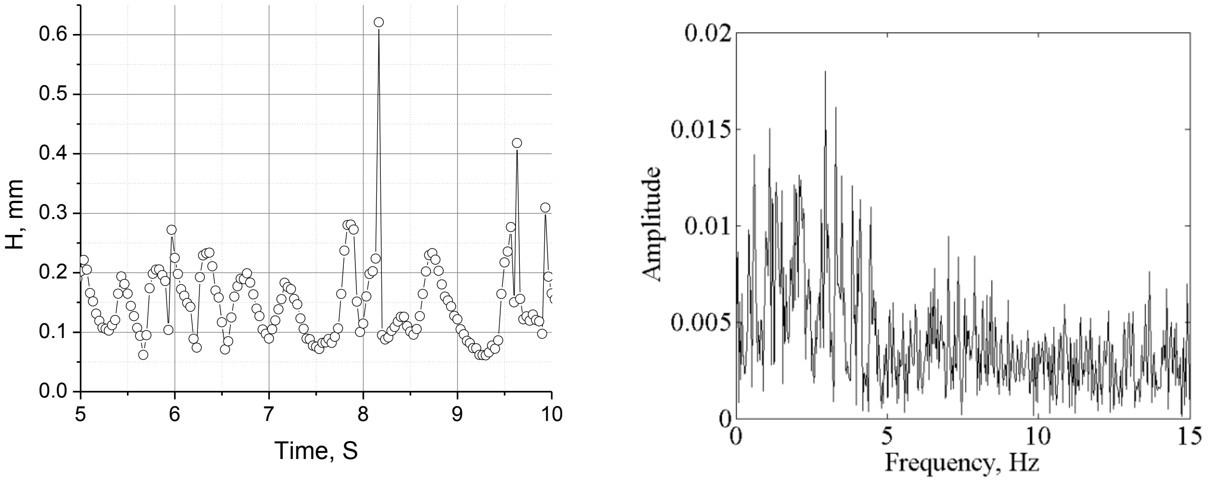

a. Time history of film thickness

b. Frequency spectrum

C. L/D=1.25D, W/D=0

Figure 2-16 *Time history of film flow thickness and wave frequency analysis*

6. Conclusions

A novel digital image projection (DIP) measurement system was developed to provide high accuracy measurement of wind-driven thin film flows. The new measurement method inherits most of the ordinary DFP technique merits such as simple set up, low cost, whole field and non-contact measurement at video speed. Compared with FTP based DFP measurement systems, the new technique proved to be more precise with a less stringent image quality requirement. Both methods were used to reconstruct a spherical cap model. The average measurement error of the DIP system was 0.04mm with a standard deviation of 0.04mm. The average measurement error of the FTP-based DFP method was 0.12mm, with a standard deviation of 0.08mm.

Wind-driven thin water film flows were measured using the DIP technique to demonstrate system's capability. Both the instantaneous and ensemble-average thin film thickness distributions were successfully reconstructed. The dynamic motion of film flow was revealed. For wind speed 10m/s cases, the results show that the water surface tension dominates the flow and makes the water-air interface shape like a flat plane. As the wind speed increases to 15m/s and 20m/s, water-air interfacial waves were observed. Those interfacial waves were generated at the range near the water outlet holes and they would attenuate and broke in to small pieces as they traveled downstream. The case of wind speed 15m/s and flow rate 16.67ml/min/cm was selected to do spectrum analysis for revealing the frequencies and transient features of those water waves. The results show that at the position L/D=0.25, the dominant wave frequency was 7Hz. At location L/D=0.75, the dominant frequency is reduced to 3.5Hz. There is no noticeable dominant frequency at location L/D=1.25. The ensemble-average thin film profiles at the centerline of film flows were also plotted. The outcomes of wind-driven thin film flows measurement demonstrate that digital image projection technique is a useful tool to investigate unsteady water-air interface behavior.

References

Adrian RJ (1991) Particle-imaging techniques for experimental fluid mechanics. Annual review of fluid mechanics 23:261-304

Boomkamp P, Boersma B, Miesen R, Beijnon G (1997) A Chebyshev collocation method for solving two-phase flow stability problems. Journal of Computational Physics 132:191-200

Burns J, Ramshaw C, Jachuck R (2003) Measurement of liquid film thickness and the determination of spin-up radius on a rotating disc using an electrical resistance technique. Chemical engineering science 58:2245-2253

Chinnov E, Kharlamov S, Saprykina A, Zhukovskaya O (2007) Measuring deformations of the heated liquid film by the fluorescence method. Thermophysics and Aeromechanics 14:241-246

Cobelli P, Pagneux V, Maurel A, Petitjeans P (2011) Experimental study on water-wave trapped modes. Journal of Fluid Mechanics 666:445-476

Cochard S, Ancey C (2008) Tracking the free surface of time-dependent flows: image processing for the dam-break problem. Experiments in Fluids 44:59-71

Gendrich C, Koochesfahani M, Nocera D (1997) Molecular tagging velocimetry and other novel applications of a new phosphorescent supramolecule. Experiments in fluids 23:361-372

Ghiglia DC, Pritt MD (1998) Two-dimensional phase unwrapping: theory, algorithms, and software. Wiley New York:, Gomit G, Chatellier L, Calluaud D, David L (2013) Free surface measurement by stereo-refraction. Experiments in fluids 54:1-11

Gorthi SS, Rastogi P (2010) Fringe projection techniques: whither we are? Optics and Lasers in Engineering 48:133-140

Hagemeier T, Hartmann M, Kühle M, Thévenin D, Zähringer K (2012) Experimental characterization of thin films, droplets and rivulets using LED fluorescence. Experiments in fluids 52:361-374

Kouyi GL, Vazquez J, Poulet J (2003) 3D free surface measurement and numerical modelling of flows in storm overflows. Flow measurement and instrumentation 14:79-87

Lel V, Al-Sibai F, Leefken A, Renz U (2005) Local thickness and wave velocity measurement of wavy films with a chromatic confocal imaging method and a fluorescence intensity technique. Experiments in fluids 39:856-864

Li F-C, Chen W-L, Li H, Zhang R (2010) An ultrasonic transmission thickness measurement system for study of water rivulets characteristics of stay cables suffering from wind–rain-induced vibration. Sensors and Actuators A: Physical 159:12-23

Liu J, Paul JD, Gollub JP (1993) Measurements of the primary instabilities of film flows. Journal of Fluid Mechanics 250:69-101

Liu J, Schneider J, Gollub JP (1995) Three-dimensional instabilities of film flows. Physics of Fluids (1994-present) 7:55-67

Liu Y, Chen W-L, Bond LJ, Hu H (2014) Development of an ultrasonic pulse-echo (UPE) technique for aircraft icing studies. 40th annual review of progress in quantitative nondestructive evaluation: Incorporating the 10th International Conference on Barkhausen Noise and Micromagnetic Testing. AIP Publishing, pp. 1757-1764

Marshall J, Ettema R (2004) Contact-line instabilities of driven liquid films. Instability of Flows

Moisy F, Rabaud M, Salsac K (2009) A synthetic Schlieren method for the measurement of the topography of a liquid interface. Experiments in Fluids 46:1021-1036

Pautsch A, Shedd T (2006) Adiabatic and diabatic measurements of the liquid film thickness during spray cooling with FC-72. International Journal of Heat and Mass Transfer 49:2610-2618

Raffel M, Willert C, Kompenhans J (1998) Particle Image Velocimetry, A Practical Guide Springer. New York

Rothmayer A, Matheis B, Timoshin S (2002) Thin liquid films flowing over external aerodynamic surfaces. Journal of engineering mathematics 42:341-357

Savelsberg R, Holten A, van de Water W (2006) Measurement of the gradient field of a turbulent free surface. Experiments in fluids 41:629-640

Schagen A, Modigell M (2007) Local film thickness and temperature distribution measurement in wavy liquid films with a laser-induced luminescence technique. Experiments in Fluids 43:209-221

Scheid B, Kabov O, Minetti C, Colinet P, Legros JC (2000) Measurement of free surface deformation by reflectance-Schlieren method Proc 3rd Eur Conf Heat Mass Transfer, Heidelberg.

Shaikh N, Siddiqui K (2010) An experimental investigation of the near surface flow over air-water and air-solid interfaces. Physics of Fluids (1994-present) 22:025103

Tsubaki R, Fujita I (2005) Stereoscopic measurement of a fluctuating free surface with discontinuities. Measurement Science and Technology 16:1894

Turney DE, Anderer A, Banerjee S (2009) A method for three-dimensional interfacial particle image velocimetry (3D-IPIV) of an air–water interface. Measurement Science and Technology 20:045403

Wanek JM, Wu CH (2006) Automated trinocular stereo imaging system for three-dimensional surface wave measurements. Ocean engineering 33:723-747

Wang B, Lohry W, Zhang S, Hu H (2012) Development of a Digital Fringe Projection Technique to Characterize the Transient Behavior of Wind-Driven Droplet/Rivulet Flows 50th AIAA Aerospace Sciences Meeting.Nashville, TN

Wang G, Rothmayer A (2009) Thin water films driven by air shear stress through roughness. Computers & Fluids 38:235-246

Yu Y, Wei S, Yang Y, Cheng X (2012) Experimental study of water film falling and spreading on a large vertical plate. Progress in Nuclear Energy 54:22-28

Zhang Q-C, Su X-Y (2002) An optical measurement of vortex shape at a free surface. Optics & Laser Technology 34:107-113

Zhang S (2010) Recent progresses on real-time 3D shape measurement using digital fringe projection techniques. Optics and lasers in engineering 48:149-158

Zhang X, Dabiri D, Gharib M (1996) Optical mapping of fluid density interfaces: concepts and implementations. Review of scientific instruments 67:1858-1868

CHAPTER 3

AN EXPERIMENTAL STUDY ON WIND-DRIVEN RIVULET FLOWS RUN BACK ALONG FLAT PLATE

Abstract: Under glaze icing condition, the icing accretion process is significantly influenced by the surface water transport behaviors. Water films, beads and rivulets are common phenomena of water runback flows. Rivulets and its subsequent icing will restrict the coming super cooled water and enhance the collection efficiency of impinging water droplets, which may cause continuous icing accretion near the rivulets. In the present study, an experimental investigation was conducted to characterize the surface wind-driven water rivulet flows over a horizontal plate. Instantaneous and time-average rivulets thicknesses were successfully reconstructed. The details of micro-structures like rivulet breaking, surface wave and rivulet meandering were clearly presented. The obtained rivulets thicknesses were further processed to get transient rivulet front velocities. A refined force-balance rivulet breaking criterion was evaluated by the measured instantaneous velocity of the rivulet fronts. The theoretical analysis qualitatively matches with the measurements. Trapped-mass effect induced by the restrain effect of meandering rivulet contact line was disclosed. A novel rivulet meandering instability threshold was developed and supported by experimental results.

1. Introduction

Rivulet flows subjected to external airflow are common features in daily life (e.g. rainwater flow on a wind shield of a vehicle) as well as in various engineering applications, such as water film heat exchangers like cooling towers, rain-wind-induced cable vibration (Chen et al. 2012, Taylor and Robertson 2011), and aircraft in heavy rain (Cao et al. 2014, Haines and Luers 1983). During glaze icing process, super cooled water beads, rivulets and film were observed by Olsen and Walker (1987). The importance of water transport behavior was disclosed by Hansman and

Turnock's experiments which showed that the surface tension of a liquid significantly alters the glaze ice shape (Hansman and Turnock 1989). The water transport behaviors directly influence the icing accretion process by redistributing the super cooled water on the airfoil surface. Besides that, the film/rivulets flow will indirectly influence the ice accretion process by interacting with local ice roughnesses. This coupled effect will change the local water droplets collection efficiency, alter the local heat transfer coefficient (Liu et al. 2015, Rothmayer and Hu 2012) and directly influence the water mass transport behavior itself by obstructing the liquid flow (Rothmayer and Hu 2014). Waldman and Hu (2015) qualitatively characterized the icing accretion process using high-speed imaging. The configuration that the rivulets would follow the leading edge film flow was clearly revealed by the high speed videos. According to the observation, the stagnated rivulets front and their subsequent icing performed as a barrier to block the coming surface water. The roughness ice range is highly suspected to be initiated by the icing accretion of stagnated film and rivulet fronts. One of the purposes of this study is to specify the rivulet/film front stagnation criterion under icing conditions.

The early investigations of the break-up of a wind-driven film/rivulet front were focused on preventing dry-patch formation on water film cooling equipments. Hartley and Murgatroyd (1964) established two film break-up criteria to determine the minimum required liquid layer thickness for dry-patch rewetting. One of them is based on the force balance (FB) analysis near the stagnation range of a dry-patch. The dry-patch breaking occurs when the inertia force surpasses the surface tension at the stagnation point. The other criterion is based on the minimization of total energy (MTE) of a stable rivulet. Both of the FB and MTE criteria are widely used and developed by following researchers. Murgatroyd (1965) refined the FB model by adding the unbalanced shear stress between the solid-liquid and liquid-gas interfaces. A character length was introduced to represent the length of unbalanced shear stress range. Murgatroy determined the shear unbalance length by fitting experimental data empirically. Penn et.al (2001) presented a work that determined the unbalanced shear length by CFD simulation. El-Genk and Sable (2001) refined the MTE model by precisely calculating the velocity distribution within the rivulets. The velocity profile was estimated by RITZ method (Finite Element Method). The refined MTE model was applied to predict the minimum film thickness of film flow on a vertical surface. El-Genk and Sable's methodology was further extended to determine the breakup of film flow subject to interfacial shear (Saber and El-Genk 2004). FB and MTE criteria are also applied to estimate the threshold film thickness of film to rivulet breaking that occurs during the water runback flow on an airfoil surface. For instance, FB criterion was used to predict rivulet formation of water runback flow on a NACA4412 airfoil (Thompson and Marrochello 1999), Al-Khalil et.al (1990) developed an anti-icing runback model based on MTE criterion.

Current FB and MTE criteria treat the stagnated rivulet front/dry patch as a smooth flat shape. In reality, hump shape rivulet front will cause an aerodynamic drag. This drag could be important, even a dominant force to overwhelm the surface tension restrain. McAlister et.al (2005) treated the wind-driven rivulet breakoff as a simple force balance between aerodynamic drag and surface tension. However, the inertia force of rivulet flow which comes from the shear stress of water-solid interface was not considered in McAlister's work. Furthermore, the rivulet flow itself is complex. The influence of micro-physical flow structures on the rivulet breaking, such as surface waves and irregular rivulet front shape is still unclear. As a result, a rivulet breaking model includes rivulets inertia, air shear stress, aerodynamic drags and combines those force terms with the transient micro-physical features of rivulet flow is highly desirable. In current study, we extend the FB rivulet model by adding the aerodynamic drag force. The micro-transient phenomena of rivulet flow are measured experimentally by digital image projection (DIP) technique. The obtained flow features are used to refine the force terms in the FB criteria. For instance, the reconstructed rivulet front shape before breaking is a hump shape whereas a flat top rivulet front was observed after breaking. As a result, the area difference between the rivulet front and rivulet body, instead of the cross-section area of the rivulet front, was suggested to use to calculate the aerodynamic drag. Those refined force terms were then evaluated by the measured rivulet stagnation points.

The other observation from current study is rivulet meandering behavior. A certain amount of water was trapped by the pinning force of the meander contact line. This water mass trapped effect directly influences the mass transport behavior during ice accretion process and provides both enough water mass and time interval for the onset of icing roughness. A quantitative model to predict meandering behavior of wind-driven rivulet flow is highly desired as well.

Gravity-driven rivulet flow meandering had been observed and experimentally investigated in the laboratory for a long time (e.g. Tanner 1960, Gorycki 1973). The following rivulet meandering investigations were focus on experimentally determining the critical flow rate and plate inclination (Culkin and Davis 1984, Nakagawa 1992, Nakagawa and Scott 1984). The systematically theoretical studies on mechanism that disturbs a straight rivulet to meander are relative slow. Kim et al. (2004) reported that the rivulet meander occurs when the tangential velocity difference across the interface surpass the capillary force due to the meander curvature. Mechanisms for meandering instability of rivulets were investigated using a Hele-Shaw cell as well (Daerr et al. 2011, Drenckhan et al. 2004). In those two investigations, the threshold of meander instability was considered as the centrifugal force overwhelms the surface tension. The centrifugal force was related to the square of the velocity difference between the rivulet mean velocity and the meander wave velocity. Grand-Piteira et al. (2006) claimed that the meandering rivulet is a simple outcome of force balance between inertia and capillarity. The onset of rivulet meandering was modeled as the force balance between the centrifugal force, capillary force (due to the meander curvature) and cross-section surface tension. Birnir et al. (2008) investigated the rivulet meandering behavior that is induced by the flow rate fluctuations. A -2/5 power-law scaling between the meander wave number and the power spectra of the deviation of rivulets from the center line was obtained experimentally and theoretically.

To the authors' knowledge, up to now, investigation on the wind-driven rivulet meandering is still blank. In this study, we present a modified model to predict the meandering behavior of wind-driven rivulet. One more aerodynamic drag term is added to the model of Grand-Piteira et al. (2006). Scaling analysis is performed to evaluate the relative importance of force terms. It is found that, under small Weber number, the capillary force due to meander curvature term and the centrifugal term can be neglected. The force balance of a stable rivulet was simplified as equilibrium between surface tension and aerodynamic drag. The new model was then used to predict the yaw angle of meander rivulet. Compared with the experimental measurement, the theoretical results provide a reasonably well estimation.

This chapter is organized in five sections as follows. Section 2 describes the experiment setup. Section 3 exhibits the transient behavior of wind-driven rivulet flow. The novel FB rivulet breaking model is proposed and evaluated with the rivulet measurements. Section 4 illustrates the rivulet meandering analysis and presents the experimental evidences for the theory. Finally, section 5 summarizes the conclusions of the study.

2. Experiment setup

The experiment setup of the rivulet flow measurements is generally the same as the film flow measurement experiment setup which was described in chapter2 (Fig. 2-11). The experiments were conducted in an open circuit low-speed wind tunnel. The wind tunnel has a plexiglas test section with dimensions of 20×14×30cm (W×H×L). Four different wind speeds 5m/s, 10m/s, 15m/s and 20m/s and two different water flow rate 100ml/min and 200ml/min were used to investigate the different behaviors of the rivulet flows. The same DIP system was installed to quantitatively investigate the dynamics of rivulet flows. A Cross line grid pattern with 1.1mm×1.1mm grid spacing was projected to flat plate model. The camera's field of view was set to 11cm×8cm. The image capture frequency was 30Hz with an exposure time of 2ms. 600 images (20s) of rivulet flow were captured for each case. The same flat plate model was used to generate the rivulet flows. The size of the flat plate was 25cm×15cm. The flat plate top surface was coated with write spray paint. A line of water outlet holes were drilled 25cm away from the leading edge. The water outlet hole has diameter 2mm. The distance between holes is 5mm. The total width of the water outlet hole array is 6cm. During the experiment, the ball valve was opened after the airflow reached steady state. The flat plate surface was kept in dry condition. The water flows were driven by the wind and rivulets were generated. The details of the experiment setup are described in chapter 2 section 4.

3. Transient behavior of rivulet flow

3.1. Transient phenomena of rivulet flows

Figure 3-1 shows the instantaneous measurement results of rivulets flow the along flat plate with a flow rate $Q = 100ml/\min$. The transient flow phenomena of the cases with a flow rate $Q = 200ml/\min$ were basically the same. L denotes the direction along stream wise and W denotes the direction along span wise. The stream wise and span wise location was normalized by the width of the water outlet holes array, which is D=6cm. The origin point of the coordinate is located in the center of the water outlet holes array (Fig. 2-12). Seen from Fig. 3-1A, under $U_\infty = 5m/s$ condition, no rivulet flow appeared. After the valve was opened, the water overflowed to all directions. Besides flowing down stream, the water flowed along the span wise and upstream directions as well. The span wise and upstream water flow was restricted by the edges of the test plate. A uniform film front slowly flowed through the entire measurement windows.

The film front was observed under a wind speed condition of $U_\infty = 10m/s$ as well (Fig. 3-1B). However, instead of smooth forward movement, the film front was pushed forward by the coming surface wave crest. Sometimes, the surface wave could not break the film front contact line. The wave was then reflected backward and merged with the next coming surface wave. After that, the merged wave crest reached the film front again and broke the surface tension limitation. As a result, the film front movement was a pause-move process. As the height of the film front was not the same along the span wise direction, the local abrupt fronts would lead to a contact line push out. Then the coming water flow tend to flow in to the generated local extrusion which made the local extrusion range grew bigger. Once the contact line boundary of the extrusion became steep enough, the film flow broke in to a wide rivulet. After that, the surface wave amplitude decreased a lot and the rivulet flow became stable.

Only a short film flow section was detected under wind speed $U_\infty = 15m/s$ (Fig. 3-1C). Two rivulets were generated at edges of the film front. The rivulet front was stagnated if the rivulet front was flat. The rivulets flowed downstream with ridge like rivulet fronts. It took a while for the rivulet head to raise high enough. Then the high-rise rivulet front suddenly broke and rivulet flowed forward a certain distance. As the break of the rivulet front was similar to a spray phenomenon, the flow paths of each rivulet were kind of irregular. The flow configuration became stable within a short time (2s to flow out the measurement windows). Surface waves were clearly detected on both of the rivulets. The rivulet width decreased along the stream wise direction.

The rivulets evolution process under wind speed $U_\infty = 20m/s$ is displayed in Fig. 3-1D. Right after the water value was opened, tiny rivulets were generated for every individual water outlet hole. Those tiny rivulets merged with each other as the rivulets head grew large enough to occupy the space between rivulets. The rivulet paths were much more irregular compared with the $U_\infty = 15m/s$ case. The rivulet width decreased as it flowed downstream too. The quantitative discussion of the runback process of rivulet flow can be found in the following paragraphs.

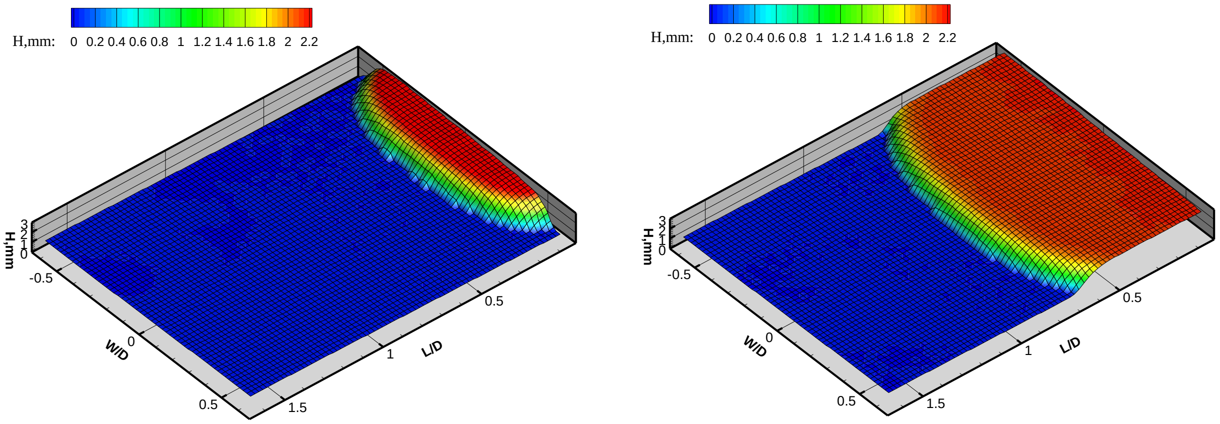

a. t=2s b. t=8s

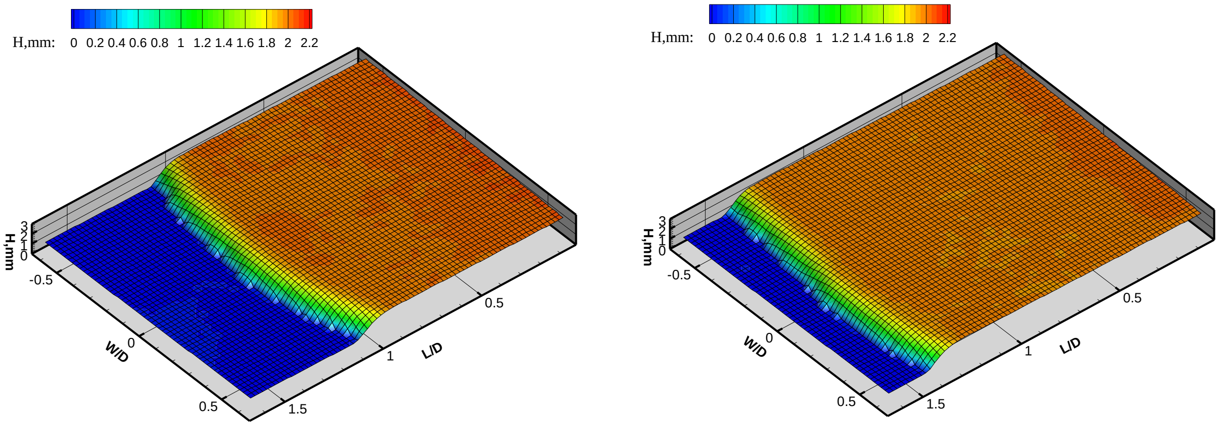

c. t=14s d. t=20s

A. $U_\infty = 5m/s$, Q=100ml/min

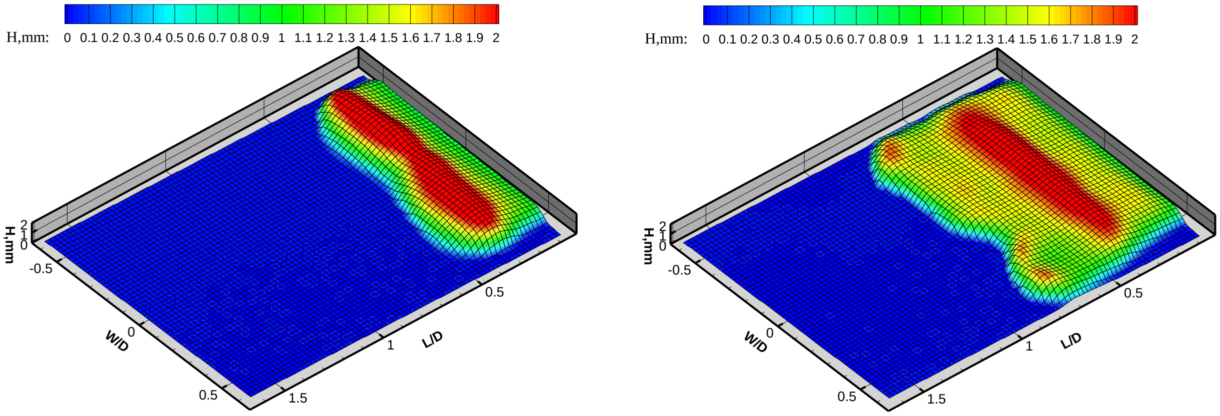

a. t=2s b. t=4s

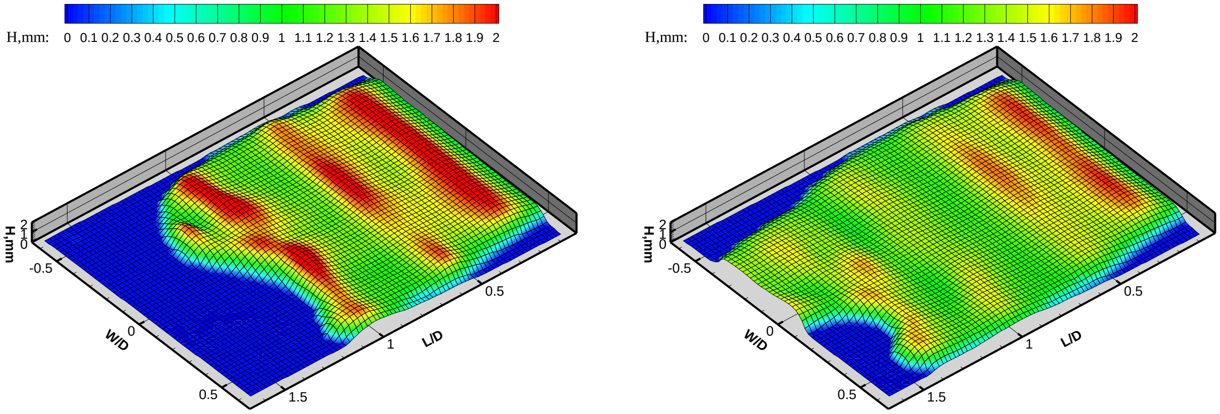

c. t=6s d. t=8s

B. $U_\infty = 10m/s$, Q=100ml/min

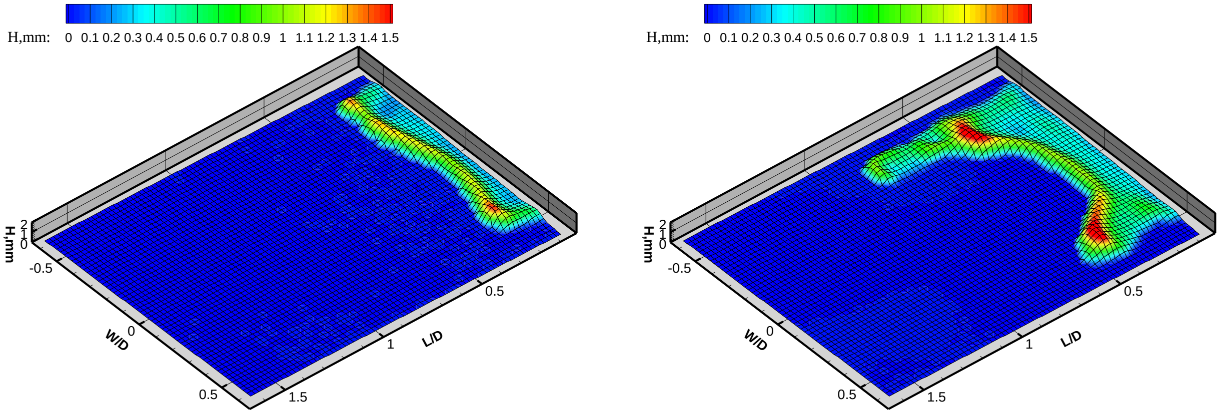

a. t=0.5s b. t=1.0s

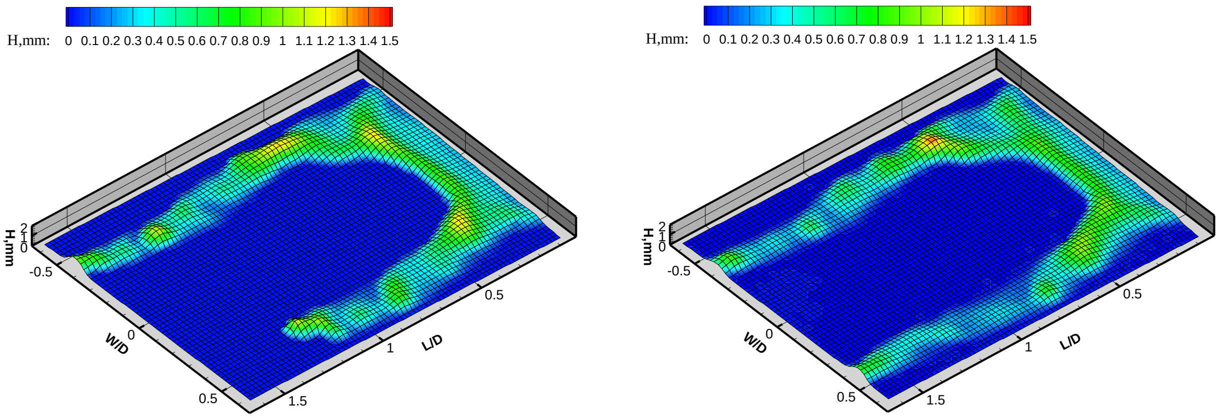

c. t=1.5s d. t=2.0s

C. $U_\infty = 15m/s$, Q=100ml/min

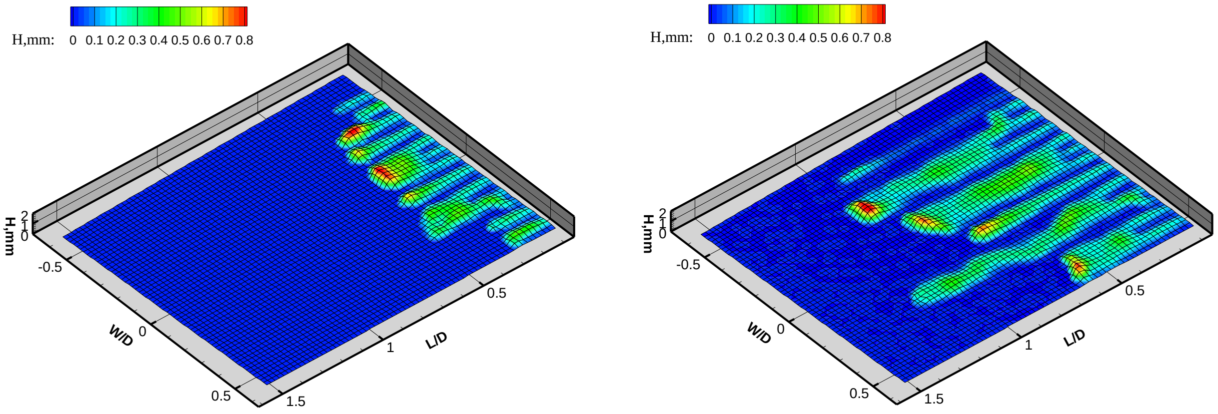

a. t=0.5s b. t=1.0s

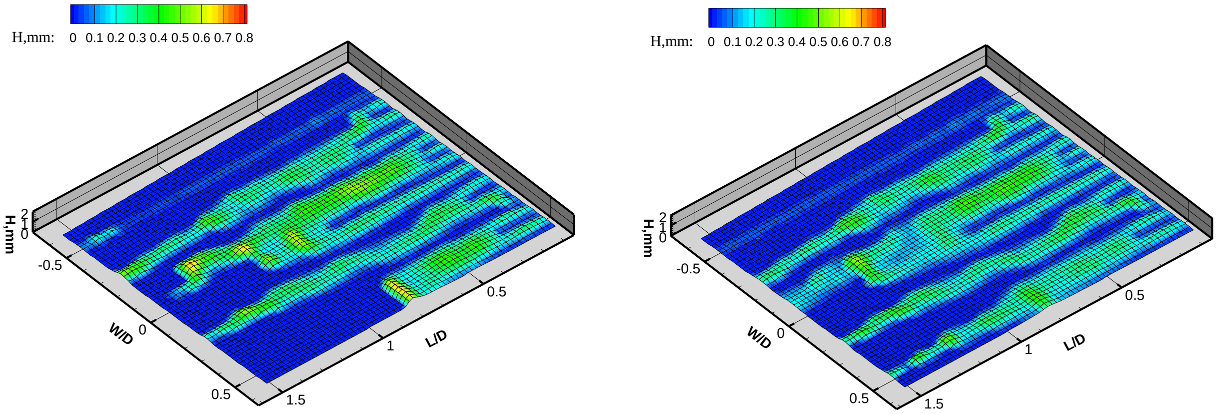

c. t=1.5s d. t=2.0s

D. $U_\infty = 20m/s$, Q=100ml/min

Figure 3-1 *Rivulet flows run back process under different wind speeds*

3.2. Rivulet/Film front moving process under low wind speed

Figure 3-2 shows the transient process of rivulet flow under wind speed $U_\infty = 5m/s$. The entire upper surface of the test model had been wetted due to the wind speed was low. As a result the generated "rivulet" was actually film flow. As seen in Fig. 3-1A, the film front was an arc shape. The film front locations shown in Fig. 3-2A are the peak locations of the film front. As the film overflowed the whole test plate, the film width was 15cm. The corresponding unit width film flow rate was $q = 6.7 ml / \min / cm$ and $q = 13.3 ml / \min / cm$. The film front location profile is a linear curve under a flow rate condition $q = 13.3 ml / \min / cm$. For the $q = 6.7 ml / \min / cm$ case, the film front is also a linear curve when $t > 4s$. That indicates that the film front generally moved with a constant speed. Figure 3-2B displays the film thickness profiles. The plotted film thickness is the span wise average film thickness at a certain time. The film thicknesses are generally a constant value besides the range near the water outlet holes. The film thicknesses are about 2mm for both of the flow rates $q = 6.7 ml / \min / cm$ and $q = 13.3 ml / \min / cm$. It indicates that stable film flows were detected during the experiment (i.e. the film thickness and film front shape was not changed as it flowed downstream). A sixth order polynomial is used to fit the film front locations. The film front velocity and acceleration are 1st and 2nd order derivatives of the fitting curves. The average film front velocities of flow rate $q = 6.7 ml / \min / cm$ and $q = 13.3 ml / \min / cm$ are 0.0042m/s and 0.0127m/s respectively. Seen from Fig. 3-2C, the film front acceleration was less than 0.003m/s^2 for most of the time. As a result, the moving film can be treated as uniform motion.

The Reynolds number of the film flow base on the unit width flow rate is $\mathrm{Re}_f = 11$ for flow rate $q = 6.7 ml / \min / cm$. By doing scaling analysis, the ratio of inertia component and viscous component can be written as:

$$\frac{u_w \dfrac{\partial u_w}{\partial x}}{\nu_w \dfrac{\partial^2 u_w}{\partial y^2}} \sim \frac{U_w H}{\nu_w} \frac{H}{L} = \mathrm{Re}_f \frac{H}{L} \tag{3.1}$$

Where ν_w represents the water kinetic viscosity, x and y are local coordinates that are tangent and normal to the flow direction. U_w, H and L denote the character value of film velocity, film thickness and stream wise length scale respectively. The film thickness is approximately 2mm. Character length L can be considered as 200mm, which is 100 times of the film thickness. According to (3.1), the inertia component is negligible for the current analysis. The momentum equation and boundary conditions to describe the film flow can be express as the following equations:

$$\nu_w \frac{\partial^2 u_w}{\partial y^2} = \frac{1}{\rho_w} \frac{\partial p}{\partial x} \tag{3.2}$$

$$\mu_w \frac{\partial u_w}{\partial y}\bigg|_{y=H} = \tau_a \tag{3.3}$$

$$u_w\big|_{y=0} = 0 \tag{3.4}$$

Equation (3.3) represents the shear stress is continuous at the air-water interface; where τ_a is the air shear stress at the air-water interface. Equation (3.4) is the no slip boundary condition. Suppose the pressure gradient is a constant value. The solution of equation (3.2) is a Poiseuille flow velocity profile:

$$u_w = \frac{1}{2\mu_w} \frac{\partial p}{\partial x} y^2 + \left(\frac{\tau_a}{\mu_w} - \frac{\partial p}{\partial x} \frac{H}{\mu_w} \right) y \tag{3.5}$$

As the film surface is smooth, the unit width pressure difference is caused by the water static pressure difference. The unit width pressure difference can be expressed by:

$$\frac{\partial p}{\partial x} = \rho_w g \frac{\left(h_{x+\Delta x} - h_x \right)}{\Delta x} \approx \rho_w g S_f \tag{3.6}$$

Where g is the acceleration of gravity, S_f denotes the slope of film surface which is a negative value in this analysis. The unit width flow rate can be obtained by integrating the velocity profile:

$$q = \int_0^H \rho_w u dy = \frac{1}{2}\frac{\tau_a \rho_w}{\mu_w} H^2 - \frac{1}{3}\frac{\rho_w^2 g S_f H^3}{\mu_w} \qquad (3.7)$$

Seen from equation (3.7), the flow rate induced by the pressure difference is proportional to the 3rd order of film thickness and the slope of the film surface S_f. That means a slight increase of the film thickness may result in a huge increase of flow rate. The flow rate is also linearly changed with the air shear stress τ_a. Seen form Fig. 3-2B, the span wise average film thickness of $q = 6.7 ml/\min/cm$ at point t=20s, L=50mm is 2.0mm, meanwhile the span wise average film thickness at the same point of $q = 13.3 ml/\min/cm$ is 2.2mm. The flow rate is doubled. However the film thickness is just increased by 10%.

Figure 3-2D shows the time history of film front contact angle. A 2nd order polynomial was used to fit the film front profile at the leading point of the film front. The contact angle is the angle between the polynomial tangent line and the bottom line of the test plate. The time average contact angle of $q = 6.7 ml/\min/cm$ was $\theta = 40.0^0$. The time average contact angle of flow rate $q = 13.3 ml/\min/cm$ was $\theta = 42.5^0$. The relationships between dynamic contact angle θ and contact line speed V_c (note that surface tension and water dynamic viscosity are constants, V_c represents the Capillary number) are generally empirical formulas (Bracke et al. 1989, Hoffman 1975, Johnson et al. 1999). Those investigations showed that the dynamic contact angle increases with contact line speed. Compared with the contact line speed of those investigations, the contact line speed in current study is a small value. A small change in dynamic contact angle is predictable.

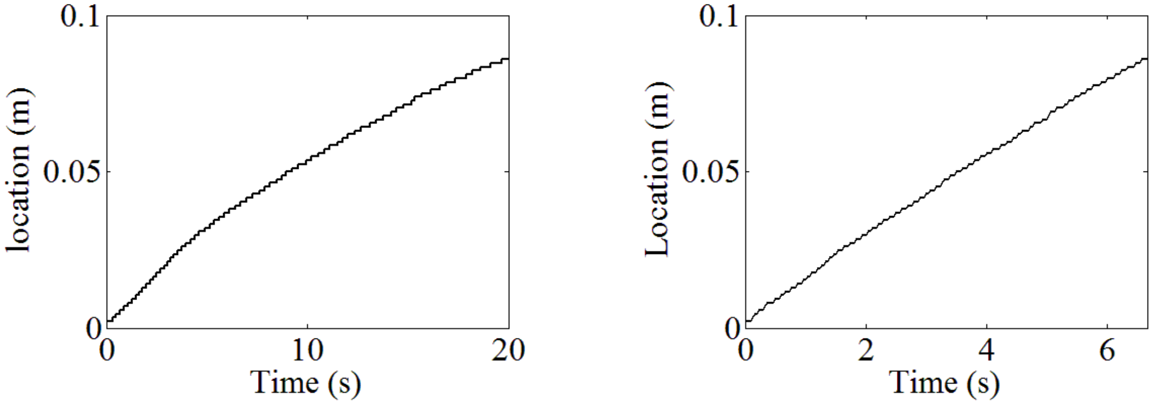

a. Q=100ml/min b. Q=200ml/min

A. Film front location

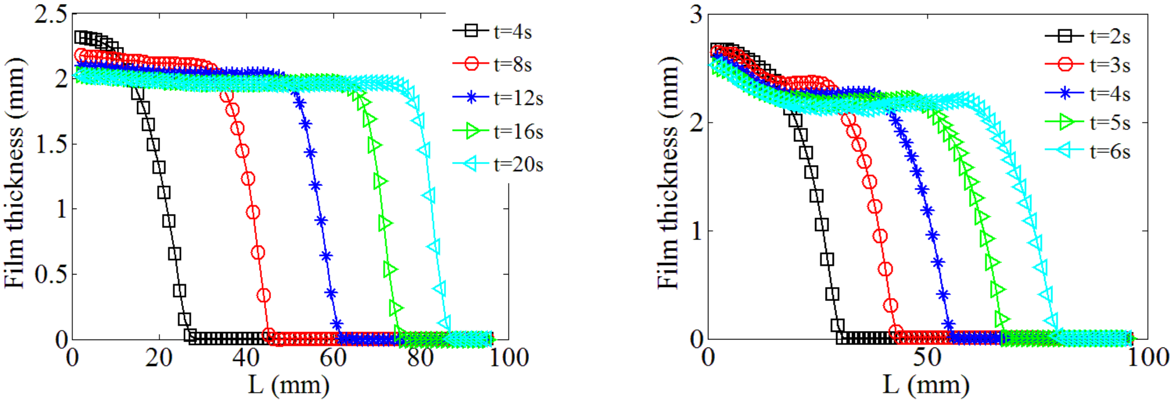

a. Q=100ml/min b. Q=200ml/min

B. Span wise average film thickness profile

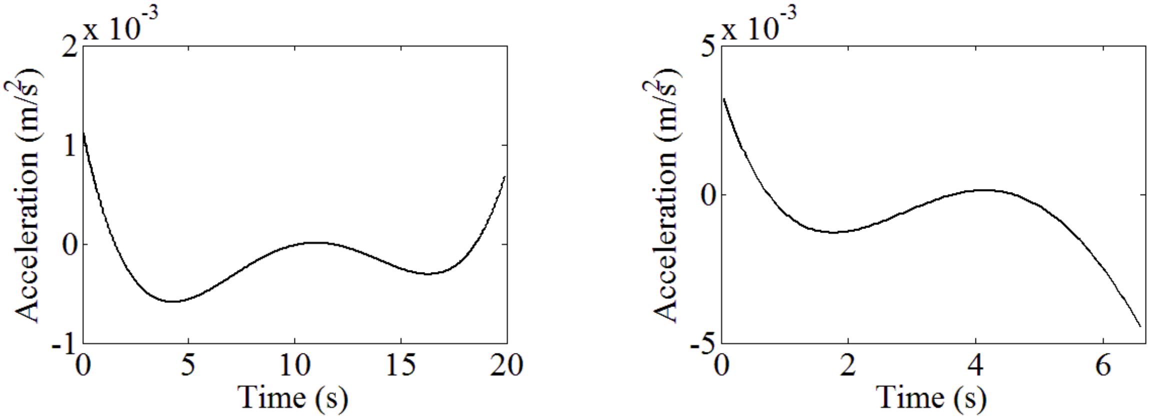

a. Q=100ml/min b. Q=200ml/min

C. Film front acceleration

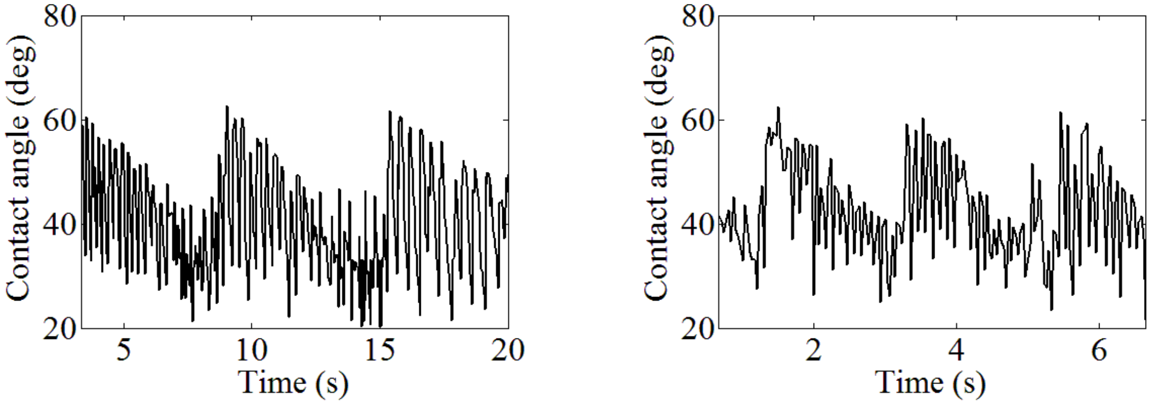

a. Q=100ml/min b. Q=200ml/min

D. Film front contact angle

Figure 3-2 *Transient process of film flow under wind speed* $U_\infty = 5m/s$.

3.3. Force balance rivulet breaking criterion

Hartley and Murgatroyd (1964) presented a criteria about the rivulet break-up. The criteria is aimed to predict the rewetting behavior of a dry patch formed in thin film flow. The criterion is from the force balance at the upstream location of a dry patch. The movement of the rivulet/film contact line can be considered as the same process as the dry-patch rewetting. In Hartley and Murgatroyd's analysis, the dry patch will be rewetted when the static pressure force, which is induced by the water kinetic energy, exceeds the restrain force caused by the surface tension:

$$t_\sigma = \int_0^H 0.5\rho_w u_w^2 dy = p_w \tag{3.8}$$

t_σ is the restraining force due to surface tension. Hartley and Murgatroyd simplified the three dimensional geometry to a two dimensional problem and assumed there is no hump shape at the dry patch front, as a result the restrain force due to the surface tension could be written as (Fig. 3-4):

$$t_\sigma = \sigma(1-\cos\theta) \tag{3.9}$$

Supposing that the film flow was laminar and the linear liquid velocity profile hypothesis within the film was applied. The static pressure could be written as:

$$p_w = \frac{\rho_w \tau_a H^3}{6\mu_w^2} \tag{3.10}$$

In equation (3.10), p_w is the water static pressure. u_w is the water velocity within the rivulet flow. For three dimensional rivulet shapes, a bead shape head usually occurs at the rivulet front. This high rise hump will lead to a shape drag. McAlister et. al (2005) introduced a model for rivulet head break off. One of the objectives of their model was to describe the periodic breakoff of the rivulet heads they observed during their experiments. The rivulet head shape was simplified as a semi-ellipsoid shape with semi-axis length H and W, where H is the rivulet head height, W is the rivulet head width. The aerodynamic drag was then modeled as:

$$F_d = \frac{1}{2}\rho_a U_\infty^2 (\frac{\pi}{2} WH) C_d \tag{3.11}$$

Where C_d is the drag coefficient for air flow past a bead shape. It depends on the rivulet head shape and the Reynolds number of the air flow. McAlister recommended $C_d = 0.6$ by performing a numerical computation on a rigid hemisphere shape. The surface tension force on the rivulet head was approximated by:

$$T_\sigma = W\sigma(\cos\theta_r - \cos\theta) \tag{3.12}$$

Where θ_r denotes the receding contact angle. No static pressure induced by the rivulet main flow was considered in McAlister's paper. As large bead shape rivulet front was assumed in McAlister's analysis, the water static pressure may not be important.

According to the observation of current experiments, the wind-driven rivulet flow exhibited complex phenomena like smooth film flow, oscillating rivulet front breakup, rivulet meandering and rivulet surface wave. The restrain force due to the surface tension T_σ and the advancing force from the aerodynamic drag are influenced by the rivulet head shape. Water static pressure p_w is highly dependent on the velocity profile with in the rivulet flow (i.e. linear velocity assumption may not hold when high amplitude surface waves appear). As a result, it is very hard to establish a well-defined accurate model to describe the diverse motions of the rivulets. In this work, we try to refine the rivulet break up criteria. The balance of surface tension, aerodynamic drag due to the head shape of rivulet and water static pressure force is used in the new criterion. However the new criterion is only aimed to roughly predict the tendency of the rivulet behavior. The force terms in the new criteria are only an approximation of the forces acting on the rivulet.

Seen from Fig. 3-2, there were three rivulet front structures: smooth film front shape, top flat bead shape ($W/\mathrm{H}>5$) and semi-ellipsoid shape. The rivulet front shape was significantly influenced by the Reynolds number. Obviously, the rivulet head changed from a smooth film front to a semi-ellipsoid shape as wind speed increased. The rivulet head shape was also affected by the rivulet Weber number which is defined as $We=\frac{\rho_w \bar{u}_w^2 H}{\sigma}$. The rivulet head would tend to be more three-dimensional for a larger Weber number. For instance, view from the top view plot, the rivulet front line displayed a larger radian arc for higher flow rate (Left column of Fig. 3-6).

Equation (3.9) could be a good estimation of restrain force induced by surface tension. Equation (3.9) is built to give the restrain force due to surface tension for two dimensional smooth film front. For three-dimensional rivulet shape, the character length scale L is much larger than the rivulet height scale H, therefore the receding contact angle θ_r approachs zero. Suppose a semi-cylinder rivulet connects with a semi-sphere head shape, the restrain force caused by the surface tension at the rivulet front is $T_\sigma=\frac{\pi}{2}W\sigma-\cos\theta W\sigma$. It is still the same order of $T_\sigma=\sigma(1-\cos\theta)W$.

The water static pressure force at the stagnation point is come from the water kinetic energy difference between the rivulet head and the rivulet body. The linear velocity profile $u_w = \frac{\tau_a y}{\mu_w}$ is used to calculate the static pressure:

$$P_w = \sum_{y=0}^{y=H} \frac{\rho_w}{2} \left(\frac{\tau_a y}{\mu_w} \right)^2 w_y \Delta y \tag{3.13}$$

Where w_y is the rivulet width at the y location (Fig. 3-3). w_y can be obtained by the average of the measured rivulet profiles. The integration of equation (3.13) needs to be calculated numerically. Equation (3.13) did not consider the influence of rivulet profile on the velocity field within the rivulet. The two-dimensional velocity distribution within the rivulet can be determined by the x direction Laplace equation:

$$\frac{\partial^2 u_w}{\partial y^2} + \frac{\partial^2 u_w}{\partial z^2} = 0 \tag{3.14a}$$

$$u_w \big|_{y=0} = 0 \tag{3.14b}$$

$$\left. \frac{\partial u_w}{\partial z} \right|_{z=0} = 0 \tag{3.14c}$$

$$\mu_w \frac{\partial u_w}{\partial r} = \tau_a \tag{3.14d}$$

Equation (3.14b) is the no-slip condition at the water-solid interface and (3.14c) assumes the velocity is symmetric with the rivulet centerline. (3.14d) indicates the shear stress at the air-water interface is continuous where the r is radial direction (normal to local water-air interface). Al-Khalil et. al (1990) presented a method to numerically solve equation (3.14). According to Al-Khalil's solution, the two-dimensional velocity distribution is generally the same as the linear velocity profile $u_w = \frac{\tau_a y}{\mu_w}$ for big rivulet width-height ratio (W/h>5). Seen from Fig. 3-1, the three-dimensional semi-ellipsoid shape only appeared at the rivulet front. The rivulet width was generally much larger than the rivulet height at the rivulet body part. If big width-height ratio is a common feature of wind-driven rivulets, equation (3.13) can perform well.

The aerodynamic force due to the front hump shape can be estimated by the following equation:

$$F_d = \frac{1}{2}\rho_a U_\infty^2 \Delta A C_d \tag{3.15}$$

In equation (3.15), ΔA is the area difference between the rivulet body and the rivulet hump front (Fig. 3-3) which can be determined by the rivulet measurement result. Marshell and Ettema (2004) approximated the flow over the rivulet head by air flow over rigid hemi-ellipsoids with different aspect ratios (Marshall and Ettema 2004). They did numerical computations and the result showed that the C_d value was around 0.6. The obtained air pressure distribution showed that the high pressure region occurred near the substrate of semi-ellipsoid shape. Figure 3-4 shows a typical rivulet break procedure. The flat rivulet front shape after the breaking process indicates that the aerodynamic force acted on the bottom part of the rivulet front. The measurement results qualitatively match with Marshell and Ettema’s work. We can see that the mean thickness of the rivulet body part account for 50% of the maximum thickness of the rivulet head. For low speed case, the smooth film front is driven by the shear stress at the water-air interface. Equation (3.15) gives a zero aerodynamic drag for that case. It is reasonable to use the area difference to evaluate the aerodynamic force. In sum, the neutral equilibrium of rivulet motion can be represented by:

$$W\sigma(1-\cos\theta) = \sum_{y=0}^{y=H} \frac{\rho_w}{2}\left(\frac{\tau_a y}{\mu_w}\right)^2 w_y \Delta y + \frac{1}{2}\rho_a U_\infty^2 \Delta A C_d \tag{3.16}$$

For two-dimensional film front shape and top flat bead shape rivulet, equation (3.16) can be reduced to two dimensional force balance:

$$\sigma(1-\cos\theta)=\frac{\rho_w\tau_a H_{rb}^3}{6\mu_w^2}+\frac{1}{2}\rho_a U_\infty^2(\mathrm{H}_{rf}-\mathrm{H}_{rb})C_d \tag{3.17}$$

In equation (3.17), H_{rf} is the maximum rivulet front thickness and H_{rb} is the rivulet body thickness.

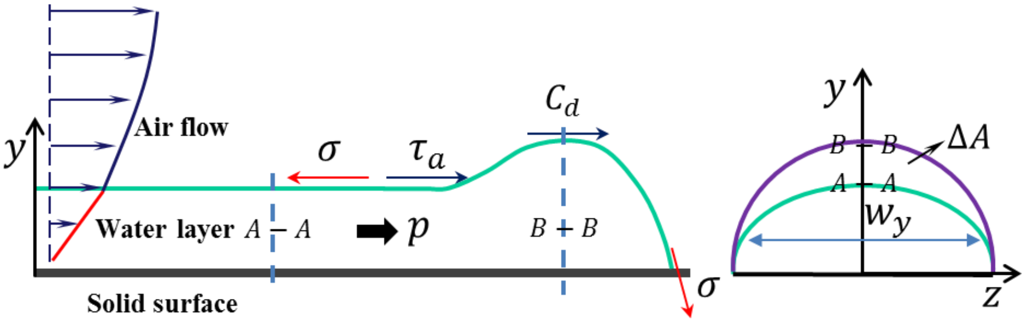

Figure 3-3 *sketch of force balance at the rivulet front*

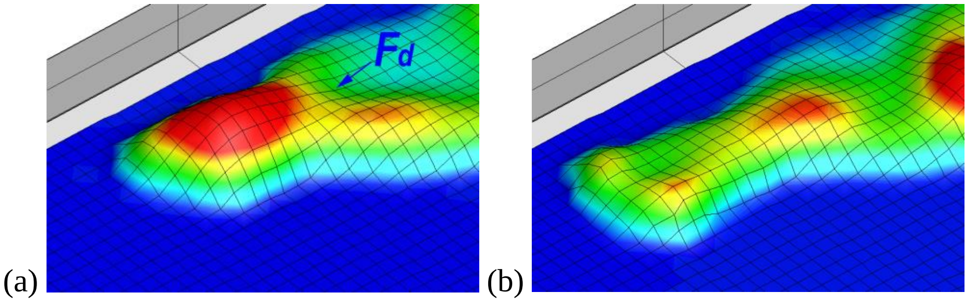

Figure 3-4 *measurement result of rivulet front break,* $U_\infty=15m/s, Q=100ml/\min$. *(a) Rivulet front before breaking. (b) Rivulet front after breaking*

The obtained transient rivulet thickness distribution images were further processed to get transient rivulet contact line peak location and contact line speed. As the wind-driven rivulet flow path was random, the time-averaged rivulet thickness configuration was used to define the rivulet front capture windows. As displayed in Fig. 3-5, the time-averaged rivulet thickness is plotted as a gray scale map. Then rivulets were numbered based on the wetted area information at the outlet of the measurement windows. The width of each time-averaged rivulet was used as a rivulet front capture windows (Blue line in Fig. 3-5). The transient water-solid contact line (red line in Fig. 3-5) was found by searching for the points where the rivulet thickness was bigger than 0.05mm. The local rivulet front peak points were the maximum points within the capture windows. Notice that the phenomena like film fronts breaking into rivulets and rivulets combination happened in the upstream range of the rivulets flow. Those phenomena will change the rivulet number. For the current study, this changing of rivulet number can not be represented. The capture windows size within the upstream range will be the width of the rivulets at the position of where the rivulet breaking or rivulet merging happened (Blue line and arrow in Fig. 3-5). The peak points of transient water-solid contact line within the capture windows were considered as the rivulet peak points. Once the rivulets peak locations were determined, the rivulets velocities were approximated by the difference of two successive peak locations divided by the measurement time interval.

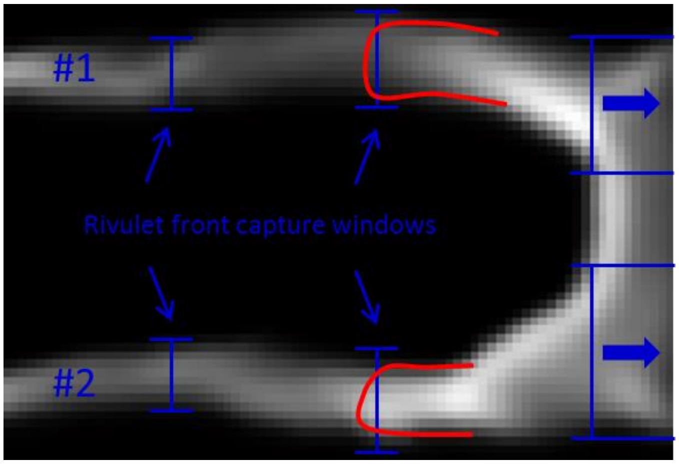

Figure 3-5 *sketch of how to find peak contact line location of rivulet flow*

The transient process of rivulet flow under wind speed $U_\infty = 10 m/s$ is revealed in Fig. 3-6. The left column of Fig. 3.6 shows the snapshot of transient rivulet fronts. The rivulet front locations can be found in the second column of Fig. 3-6 and the rivulet velocities are shown in the third column of the figure. As discussed above, the rivulet front moving was a pause-move process. This process was significantly influenced by the surface wave behavior. The stalled water-solid contact line broke up when the surface wave crest reached the contact line. The moving of the dynamic contact line would also be accelerated when the wave crest reached to the contact line. The rivulet stagnation phenomenon is clearly revealed by the zero velocity points in the velocity history profile shown in Fig. 3-6. The rivulet head break-up and accelerations are displayed as the velocity peak points in Fig. 3-6A.c. Seen from Fig. 3-6A.c, the stagnation period for the flow rate $Q = 200ml/\min$ case is much shorter than the $Q = 100ml/\min$ case. Although the rivulet flow is influenced by the surface waves and displays unsteady phenomena, the final rivulet front history shows a straight line shape. It indicates the tiny flow structures like surface wave and irregular rivulet front contact line will not influence the flow for a long time scale. The average rivulet velocities are 0.014m/s and 0.044m/s for flow rates of $Q = 100ml/\min$ and $Q = 200ml/\min$ respectively.

Seen from Fig. 3-6, the generated rivulet front during the experiment can be characterized as a wide two-dimensional film front shape for the $Q = 100ml/\min$ case and top flat bead shape ($\mathrm{W/H} \sim 6$) for $Q = 200ml/\min$. Equation (3.17) is used to do the force analysis near the rivulet front. In fact, the rivulet width of the $Q = 200ml/\min$ case was doubled during its moving process. However, the rivulet front moving velocity was the same. It indicates the rivulet width-depth ratio $\mathrm{W/H}$ will not significantly influence rivulet flow process when rivulet width is much larger than rivulet depth. The time-average rivulet front contact angles were 53° and 54° for flow rates of $Q = 100ml/\min$ and $Q = 200ml/\min$ respectively. Then the restrain term due to the surface tension $t_{\sigma} = (1 - \cos\theta)\sigma$ was roughly the same for both of the flow rates. Meanwhile, the typical rivulet body thickness for flow rate $Q = 100ml/min$ was 1.2mm and 1.5mm for flow rate $Q = 200ml/min$. The typical maximum rivulet front thicknesses H_{rf} for both of the flow rates ranged from 2.5mm-3.5mm. The aerodynamic drags induced by the rivulet front shape were about the same for both of the flow rate. The height differences between rivulet front and rivulet body were $\mathrm{H}_{rf} - \mathrm{H}_{rb} \sim 1mm$. The shape drag coefficient C_d is around 0.6 from Marshall and

Ettema's numerical calculation (Marshall and Ettema, 2004). The aerodynamic drag term was approximately $f_d \sim 0.036N/m$ and the surface tension restrain force was about $t_\sigma \sim 0.04N/m$, which means the aerodynamic drag and surface tension restrain were roughly in a balanced condition. As water static pressure p_w is proportional to H_{rb}^3, the propulsion pressure from the dynamic energy of the rivulet body is two times higher for the flow rate $Q = 200ml/min$ case. This higher static pressure causes the rivulet front contact line keep moving forward. Due to the observation, for the flow rate $Q = 200ml/\min$ case, the rivulet front contact line would only stagnate when the coming surface wave crest approached but did not yet reach the rivulet front (Fig. 3-6.B.a). At that moment, the rivulet head had a flat top surface; the aerodynamic drag at the rivulet head was significantly undermined and the force balance is under the moving criteria of equation (3.17).

Figure 3-7 shows the rivulet fronts and velocities time history under wind speed 15m/s and 20m/s. The left column of Fig. 3-7 indicates the rivulets identifier; the rivulets are all numbered by the increase of the y axis in the image coordinate. The second and third column of Fig. 3-7 shows the time history of rivulet front location and rivulet head velocity respectively. As the wind speed increases, a smaller rivulet head size will be enough to break the force balance criteria. Rivulets breaking and merging become common phenomena. Although the generated rivulets showed different behaviors under the same experimental condition, the results still prove that the rivulet velocity monotonically increases with wind speed and liquid flow rate. Seen from the second column of Fig. 3-7, the flow paths of rivulet #1, #2 under condition $U_\infty = 15m/s, Q = 200ml/\min$, rivulet #2, #4 under condition $U_\infty = 20m/s, Q = 100ml/\min$, rivulet #5, #6 under condition $U_\infty = 20m/s, Q = 200ml/\min$ are basically the same. Similar to the moving rivulet head profiles of the $U_\infty = 10 m/s$ cases, the moving profiles of those rivulet pairs are straight lines as well. As discussed in the $U_\infty = 10 m/s$ cases, for long timescales, the rivulet front moving velocity is stable the other time, which supports that the micro-structures of rivulet flow will not turn the flow into a periodic motion. It seems the rivulet contact line moving process under-goes an energy balance process at the rivulet front that is the dynamic energy of the rivulet plus the energy absorbed from the air flow balance with the energy that is required to wet the surface. Meanwhile, the transient velocity histories of those rivulet pairs are quite different. The velocity profiles exhibit zig-zig shapes. It reveals the rivulet front velocity is accelerated by the wave crest and decelerated by the wave trough. The mismatch of rivulet front velocity indicates this acceleration and decelerations effect is random and makes the transient velocity unpredictable for a short timescales.

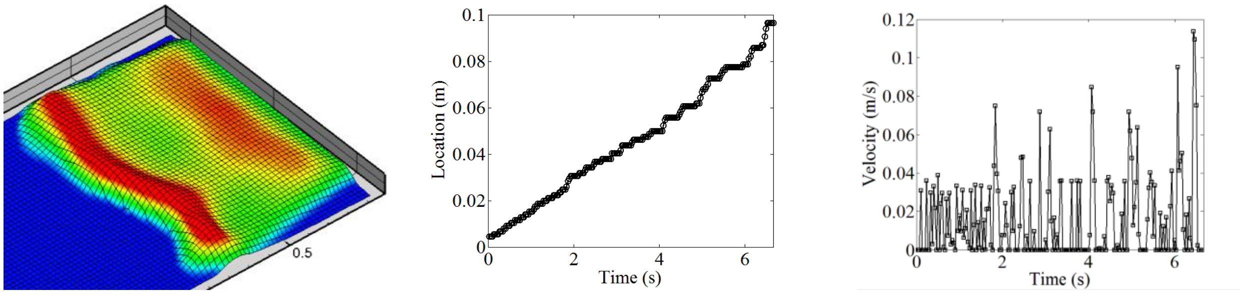

(a) Rivulet front snapshot (b) Rivulet head location (c) Rivulet head velocity

(A) $U_\infty = 10 m/s$, Q=100ml/min

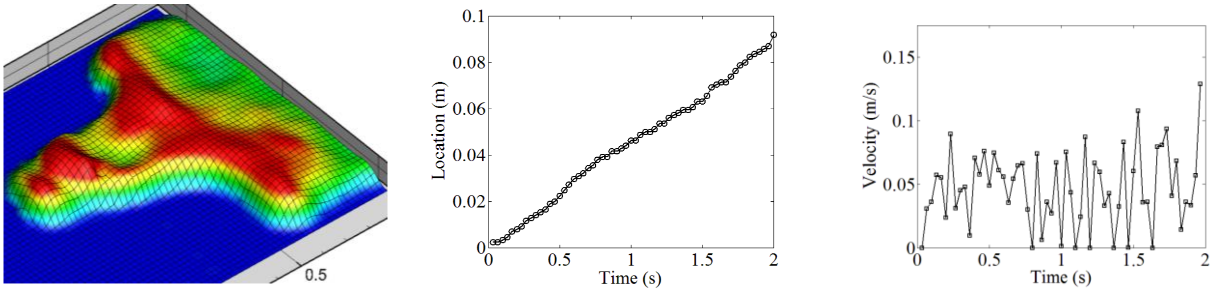

(a) Rivulet front snapshot (b) Film front location (c) Film front velocity

(B) $U_\infty = 10 m/s$, Q=200ml/min

Figure 3-6. *Rivulet front location and velocity under wind speed* $U_\infty = 10 m/s$.

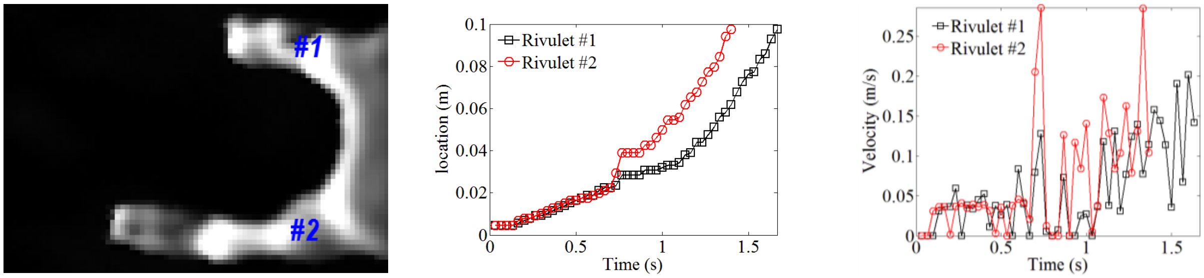

(a) Rivulet number indicator (b) Rivulet head location (c) Rivulet head velocity

A. $U_\infty = 15m/s, Q = 100ml/\min$

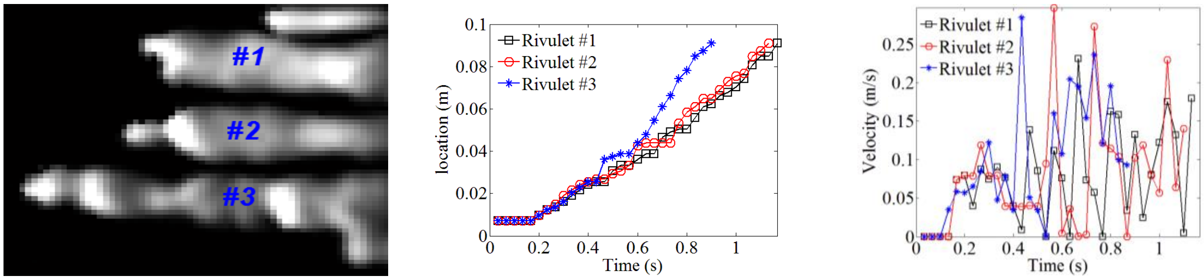

(a) Rivulet number indicator (b) Rivulet head location (c) Rivulet head velocity

B. $U_\infty = 15m/s, Q = 200ml/\min$

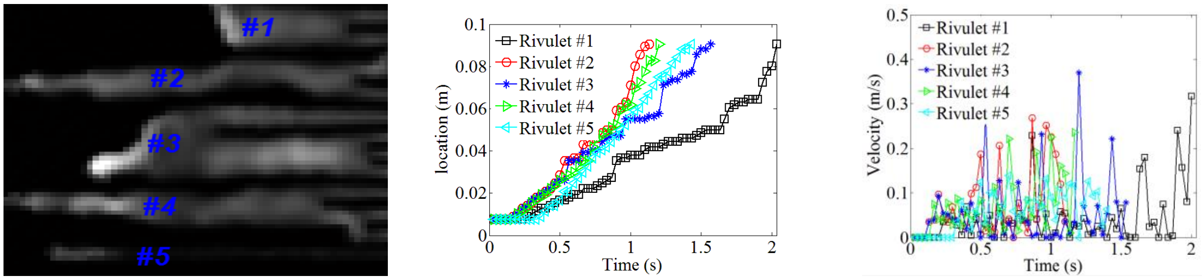

(a) Rivulet number indicator (b) Rivulet head location (c) Rivulet head velocity

C. $U_\infty = 20m/s, Q = 100ml/\min$

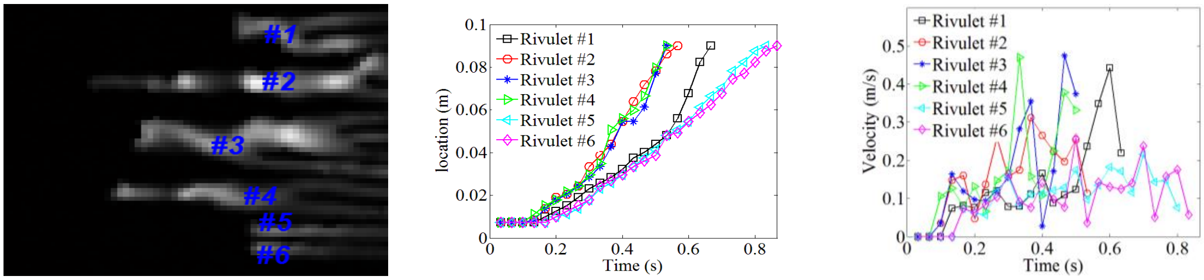

(a) Rivulet number indicator (b) Rivulet head location (c) Rivulet head velocity

D. $U_\infty = 20m/s, Q = 200ml/\min$

Figure 3-7 *Rivulet head transient location and velocity history.*

4. Wind-driven rivulet meandering behavior

4.1. Theory of meandering stability of rivulet flow

Figure 3-8 shows the time-average rivulet thickness distributions under different wind speeds and flow rates. After the steady-state rivulet configurations were formed, 500 measurements were taken to do the time-average rivulet thickness calculation. As shown in Fig. 3-8.a and 3-8.b, the rivulet surfaces were flat and smooth for wind speed $U_{\infty} = 10 m / s$. The rivulet thicknesses were uniform along the transverse direction and slightly decreased along the longitudinal direction. Unlike the straight cylindrical rivulets we observed on the an airfoil surface(Zhang and Hu 2014), meandering rivulets were observed for high wind speeds. Local rivulet humps were generated near the meandered rivulets. Similar to the film flow water trapping effect induced by the local roughness (Rothmayer and Hu 2014), a certain amount of water mass was held in place near the meandered rivulet contact lines as well. This mass trapping effect dose not significantly affect the rate of the mass transport. However it directly holds a certain fraction of the water mass and may create a time lag as the trapped water accumulates near the meandered contact line. Local supper cold water supply and enough time for icing are the necessary conditions for local icing accretion. The meandering of rivulets provides both of the conditions and hence could be an onset perturbation of roughness ice generation during the aircraft icing process.

Rivulet meandering behaviors can be revealed more clearly in Fig. 3-10. In Fig. 3-10, the maximum rivulets thickness lines are plotted on the plan view of the gray-scale time-average rivulet thickness contour maps. The maximum rivulet thickness lines were obviously detached from the centerlines of rivulets. Arc structures were shown even the rivulet edges were seemed straight. According to the observation, rivulets meandering were initiated by two effects: (i) rivulet front thickness is not uniform along the transverse direction, which cause the rivulet front break at the local peak height location and generates an irregular rivulet head shape; (ii) Rivulets merge itself is a meandering behavior. Film to rivulet breaking can be considered as a special case of effect (i). It is easier to form a local hump for a wide rivulet. So the meandering behavior is easier to be initiated for wide rivulets. It is proved by Fig. 3-8.e and Fig. 3-8.f, where no meandering phenomenon is observed for thin rivulets. Le Grand-Piteira et al. (2006) modeled the onset of gravity driven rivulet meandering as a balance between inertia force and capillary force at a cross-section of rivulet:

$$\rho_w \frac{Q^2}{AR_m} = \sigma \frac{C(\bar{\theta})W}{R_m} + \sigma(\cos(\theta_r) - \cos(\theta_a)) \tag{3.18}$$

Where R_m denotes the initial radius of curvature (Fig. 3-9), $\bar{\theta}$,θ_a, θ_r denotes the average contact angle, advancing contact angle, receding contact angle of the transverse rivulet cross section respectively. $f_\sigma = \sigma(\cos(\theta_r) - \cos(\theta_a))$ is the surface tension force. $f_c = \rho_w \frac{Q^2}{AR_m}$ is the centrifugal force. $ts_\sigma = \sigma \frac{C(\bar{\theta})W}{R_m}$ is the straightening force induced by the capillary force along the rivulet longitude direction (Fig. 3-9), $C(\bar{\theta}) = \frac{\bar{\theta}}{\sin\bar{\theta}} - \cos\bar{\theta}$ is a constant. Differ from the gravity-driven rivulet flow; the aerodynamic drag occurs in a wind-driven rivulet flow. Seen from Fig. 3-9, ts_σ is always straighten the rivulet flow. f_c tends to force a rivulet flow transverse. The aerodynamic drag term stabilizes the rivulet flow when the rivulet flow away from the curvature center and destabilizes the rivulet flow when the rivulet flow toward the curvature center. It should be noticed that the aerodynamic term always pushes the rivulet flow along stream wise direction. This effect tends to regular the meandered rivulets back to the stream wise direction. The force balance for the wind-driven meander rivulet flow can be described by the following equations:

$$\rho_w \frac{Q^2}{AR_m} \pm \frac{1}{2}\rho_a U_\infty^2 H_{rb} C_d \sin(\varphi) = \sigma \frac{C(\bar{\theta})W}{R_m} \pm \sigma(\cos(\theta_r) - \cos(\theta_a)) \tag{3.19}$$

In equation (3.19), $f_d = \frac{1}{2}\rho_a U_\infty^2 A C_d$ is the aerodynamic drag, A is the cross section area of the rivulet, φ is the angle between rivulet and stream line. Scale analysis was performed to compare the terms in equation (3.19). The ratio of centrifugal force to capillary force induced by the curvature is:

$$f_c / ts_\sigma = \rho_w \frac{Q^2}{AR_m} \Big/ \sigma \frac{C(\bar{\theta})W}{R_m} = \rho_w Q^2 \big/ A\sigma C(\bar{\theta})W \approx We_r \big/ 2C(\bar{\theta}) \tag{3.20}$$

In equation (3.20), the rivulet area was approximated by $A = 0.5WH$. The obtained equation shows that the relative importance of centrifugal force to capillary force is determined by the rivulet Weber number and the average contact angle. The average contact angle of the rivuelt cross section can be estimated by $\bar{\theta} = \arcsin(4HW/(4H^2 + W^2))$. Using $W/H = 5$, we get $\bar{\theta} = 44^\circ$ and $C(\bar{\theta}) = 0.28$. The actually measured rivulet width to height ratio was bigger than 5, typical $C(\bar{\theta})$ value was smaller than 0.28. For the current work, the typical rivulet Weber number was 0.3-0.7. Hence, the centrifugal force was the same order as capillary force.

The ratio of capillary force to surface tension at the rivulet cross section is:

$$ts_\sigma / f_\sigma = C(\bar{\theta})W/R_m (\cos(\theta_r) - \cos(\theta_a)) \tag{3.21}$$

The meander curvature R_m was generally much larger than the rivulet width. The typical value of $\cos(\theta_r) - \cos(\theta_a)$ would be about 0.5 which is about twice of $C(\bar{\theta})$. Then the capillary force term can be neglected. From (3.20), for a rivulet flow with a Weber number value smaller than 1, the centrifugal force is negligible as well. Then the rivulet flow is in a balance between aerodynamic drag and surface tension term. The maximum meandered yaw angle φ could be predicted by the following equation:

$$\varphi = \arcsin(2\sigma(\cos(\theta_r) - \cos(\theta_a)) / \rho_a U_\infty^2 H C_d) \tag{3.22}$$

For higher wind speeds, the aerodynamic drag is larger than the surface tension. The transverse component of aerodynamic drag is large enough to turn the meander rivulet back to streamwise direction. Comparable to the damping term in the oscillation system, meandering rivulets will flow back to the stream line due to the damping of the aerodynamic drag. The maximum meander yaw angle decreases with wind speed increases. Both of the aerodynamic damping phenomenon and yaw angle decreasing phenomenon are qualitatively shown in Fig. 3-8.

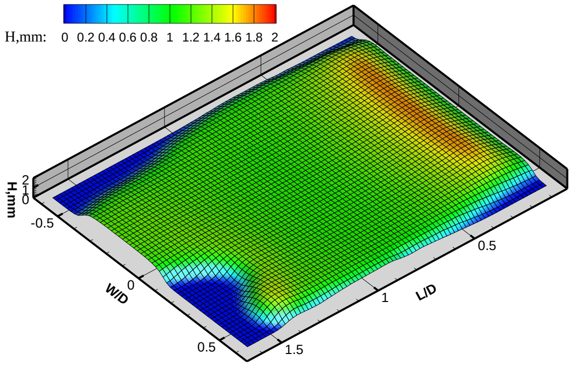

a. 100ml/min, $U_\infty = 10 m/s$

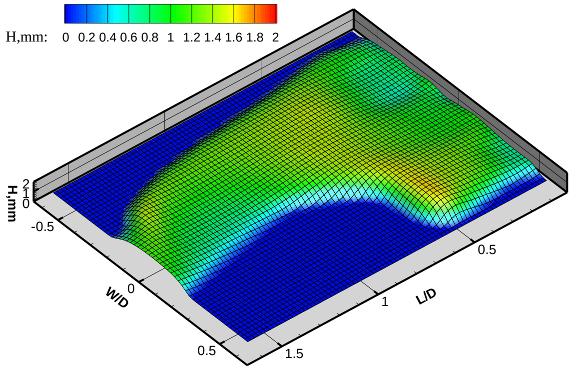

b. 200ml/min, $U_\infty = 10 m/s$

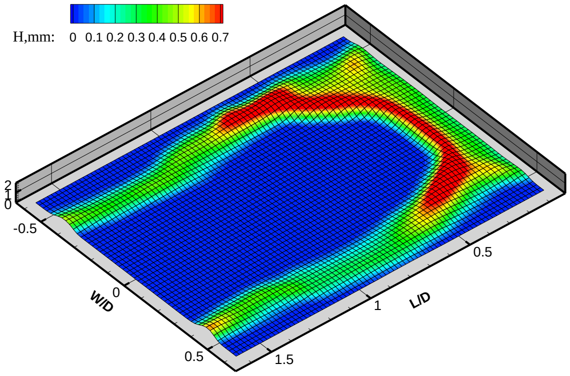

c. 100ml/min, $U_\infty = 15 m/s$

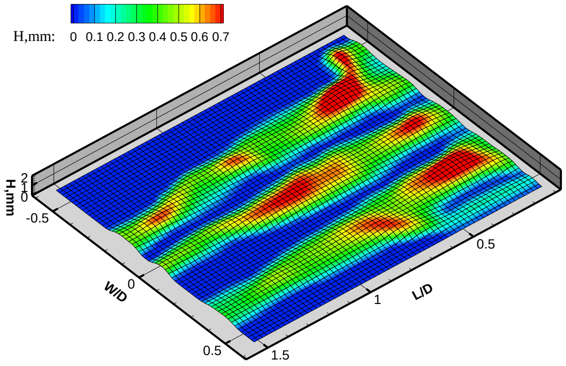

d. 200ml/min, $U_\infty = 15 m/s$

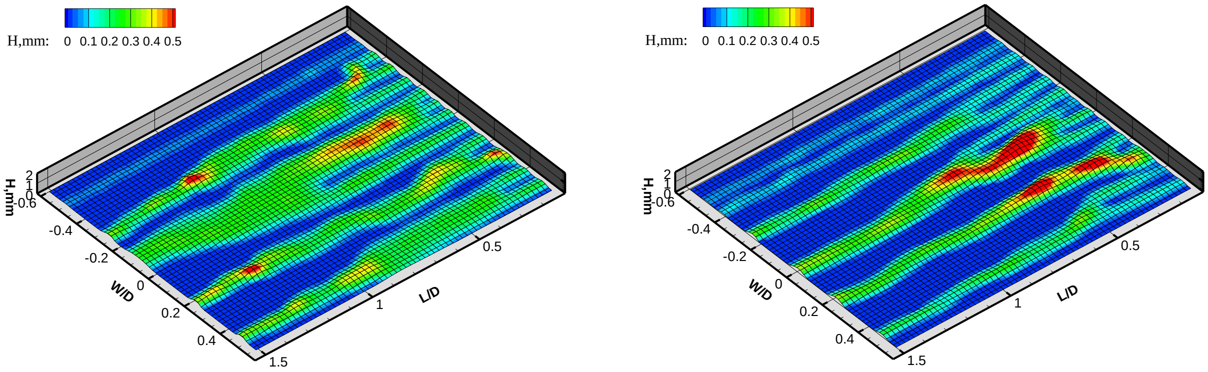

e. 100ml/min, $U_\infty = 20m/s$ f. 200ml/min, $U_\infty = 20m/s$

Figure 3-8 *Time average result of rivulet flows*

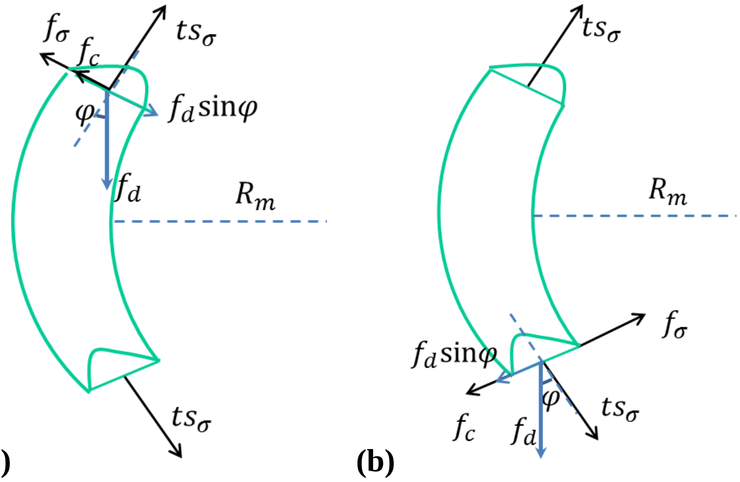

Figure 3-9 *Force acting on a meander, in the plane of the plate. The meander curvature stabilize the rivulet both in (a) and (b). Aerodynamic drag affects rivulets along stream wise direction. It stabilizes the rivulets in (a) and destabilizes the rivulet in (b). But it always drives the rivulets flow along stream wise.*

4.2. Experiment evidences of meandering instability theory

The meandering behavior of rivulet #1 under the condition $U_\infty = 15m/s, Q = 100ml/\min$ was selected as an example to validate equation (3.19) and (3.22). The rivulet meander was initialized by the film-rivulets breaking process. The rivulet width was about $W = 12mm$ and rivulet meandering curvature radius was about $R_m = 45mm$ (suppose the meander rivulet was an arc line). The cross-section area and rivulet height decreased with stream wise distance. The typical value of the rivulet area and height were $A = 0.03cm^2$ and $H = 1mm$ respectively. The rivulet

Weber number was roughly estimated as $We = 0.77$. Under this Weber number, aerodynamic drag and cross-section surface tension acted to control the rivulet flow. The maximum yaw angle occurred near the film braking point (Fig. 3-10a).

The actual estimation of capillary term, centrifugal term, surface tension term were 0.0052N/m, 0.005N/m and 0.035N/m respectively. Compare with the surface tension, the capillary force and centrifugal force were small values and could be neglected (Actually they canceled out each other in this case). Using equation (3.22), supposed $C_d = 0.6$, the calculated maximum yaw angle φ was 23.4^0. The actual measured yaw angle based on the maximum rivulet thickness line was 24.5^0. The same process was used to calculate the maximum raw angle of rivulet #2 shown in Fig. 2-10a. The height difference at the rivulet hump was used to do the estimation, which was $\Delta H = 0.5mm$. The obtained maximum yaw angle was 41^0 whereas the measured yaw angle was 36^0. The comparisons prove that equation (3.22) can quantitatively predict the meander yaw angle.

Figure 3-11 shows the rivulet profiles of rivulet #1 at locations L/D=0.35 and L/D= 1.2 (Fig. 3-10). Ten successive measured rivulet profiles are plotted. As display in Fig. 3-11, the surface tension term f_σ at the rivulet cross-section was always opposite to the aerodynamic drag at the same location, hence the capillary term ts_σ and centrifugal term f_c must be small components at that point, which is confirmed with the scaling analysis. The f_σ term was not always stabilizing the meander rivulet, which is different from the common sense.

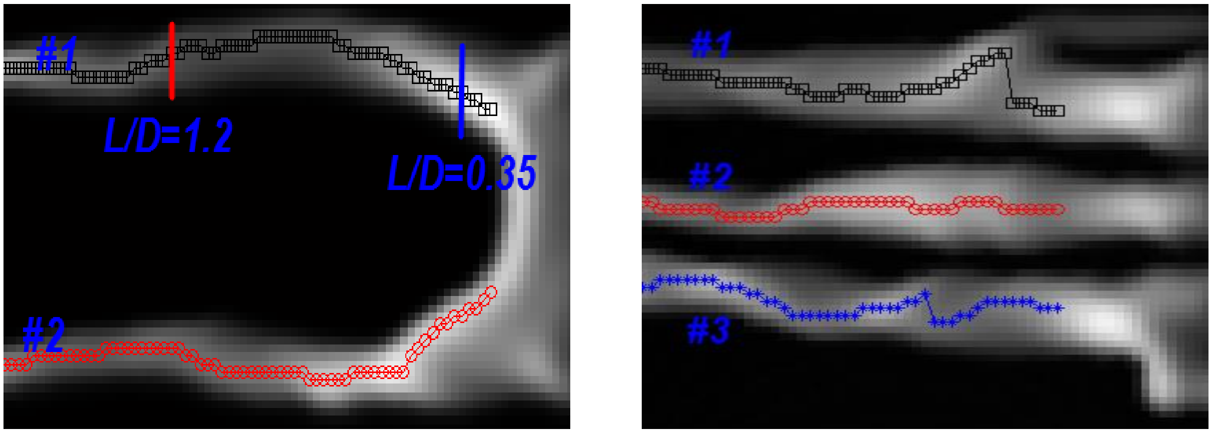

a. 100ml/min, $U_\infty = 15m/s$ b. 200ml/min, $U_\infty = 15m/s$

Figure 3-10 *Rivulet maximum height location*

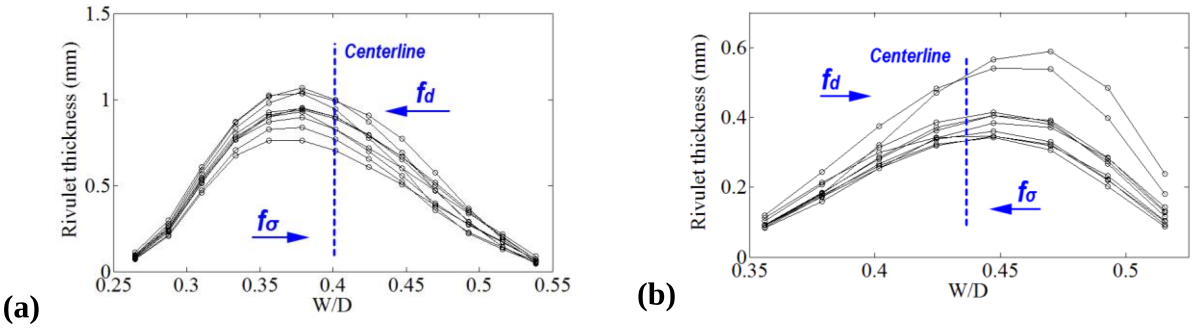

Figure 3-11 *Influence of aerodynamic force on rivulet cross-section profile. (a) Rivulet profile of Rivulet #1 at L/D=0.35 (blue line in Fig.3-10). (b) Rivulet profile of Rivulet #1 at L/D=1.2(red line in Fig.3-10) Ten successive measurements are plotted. The flow condition is* $U_\infty = 15m/s, Q = 100ml/\min$.

One more interesting phenomenon, transverse oscillation, was observed from the measurement results. This transverse oscillation is suspected to be related to the rivulet meandering. The time history of the rivulet thickness, the rivulet spanwise maximum thickness location, and the rivulet area, at the location L/D=1.0 are plotted in Fig. 3-12. The oscillation frequencies were obtained by using spectral analysis. It was found that the oscillation frequencies of those three vibrations are the same $f = 7.44Hz$. Cross-correlation calculations were performed to check the relevance of those three vibrations. The result showed that the oscillations of the rivulet thickness and rivulet area were phase coherent, which proves the surface wave is vibration primary at vertical direction. Unfortunately, the correlation coefficient of the rivulet thickness and rivulet transverse maximum rivulet thickness location was small (<0.1). However, it does not mean the transverse oscillation was irrelevant to the vertical vibration. Actually, due to the limitation of the measurement spatial resolution (1.2mm), only several transverse locations were recorded in Fig. 3-12. Correspondingly, only several separated phase values were recorded (Fig.3-12b) which may cause the low correlation coefficient. The possible reason of this transverse vibration is still unclear and needed to further investigate.

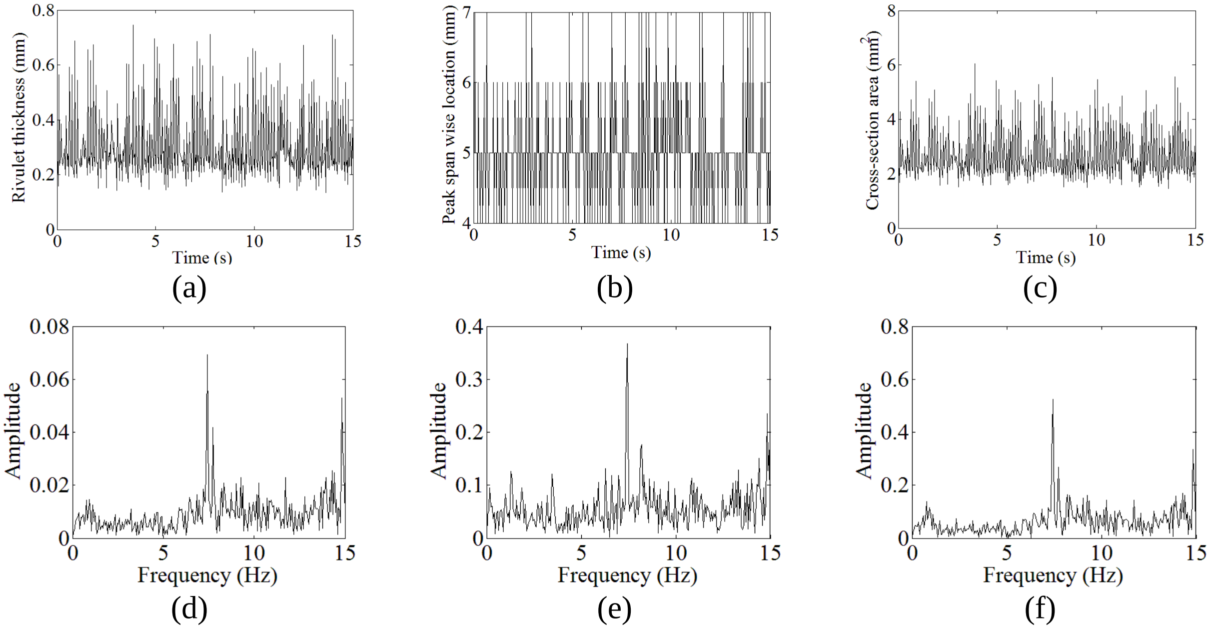

(a) (b) (c)

(d) (e) (f)

Figure 3-12. *Spectrum analysis of rivulet #1 under wind speed* $U_\infty = 15 m/s$, *Q=100ml/min condition (Fig3-10.a). (a) Time history of rivulet thickness. (b) Time history of span wise maximum rivulet thickness location. (c) Time history of rivulet cross-section area. (d) Frequency spectrum of rivulet thickness. (e) Frequency spectrum of span wise peak location. (f) Frequency spectrum of rivulet cross section area*

5. Conclusions

An experimental study is reported to characterize the runback behaviors of the wind-driven rivulet flows on a flat plate. By using the DIP system, rivulet thickness measurements are achieved under a variety of wind speeds and flow rates. The time-resolved measurements including the time histories of rivulet front contact angles, locations and velocities were well performed. Micro-physical phenomena like rivulet breaking, surface wave and rivulet meandering were clearly reconstructed. Those micro-structures were utilized to refine the force-balance rivulet breaking criterion. Wind-driven rivulet meandering instability were observed and theoretically clarified. A novel rivulet meandering stability criterion is developed and supported by the experiment results. The conclusion derived from the experiments can be summarized as follows:

- Using DIP system, the transient behaviors of wind-driven rivulet flows were characterized by the detailed measurement of multi-quantities including rivulet thickness, water-solid contact line, and the location, velocity and advancing contact angle of rivulet front. With wind speed increase, the rivulet front shape evolves from film front to flat top bead shape and then to ellipsoid bead shape. The steady-state rivulet body has a large height-to-width ratio.

- For low wind speed ($U_\infty = 5m/s$), film flow were observed. The film front underwent a uniform motion. The film thickness was influenced by the pressure gradient induced by the gravity. For wind speeds $U_\infty = 10m/s$ and $U_\infty = 15m/s$, the moving of rivulet contact line was a pause-move process which was significantly influenced by the surface waves. The rivulet front stagnated and then rose to a hump shape. Once the rivulet front grew high enough, the rivulet front contact line suddenly broke and moved forward. For high wind speed $U_\infty = 20m/s$, the rivulet motion accelerated as the wave crest reached the rivulet front and decelerated as the wave trough reached the rivulet front.

- The obtained rivulet thickness was further processed to get transient rivulet front locations and velocities. The rivulet moving phenomena are distinctly reflected by the obtained time history of rivulet front transient velocities. The zero rivulet front velocity represents the rivulet front stagnation whereas an abruptly velocity increase represents the rivulet front breaking. The zig-zig rivulet front velocity profile represents the acceleration and deceleration effects caused by surface waves. Although the transient velocities varied with time, the rivulets front location time histories are straight lines, which indicates for a relative long timescale, the wind-driven rivulets flows are uniform motions. The micro-flow structures like surface waves and irregular rivulet fronts will influence the transient behavior of a rivulet but have limit effect on the rivulet motion for a long timescale.

- The behavior of transient rivulet flow subject to the external airflow had been modeled by a balance of surface tension, static pressure induced by the dynamic energy of rivulet flow, and aerodynamic drag due to shape of rivulet. The individual force term is evaluated by the flow features observed during the experiment. For instance, as the height-width ratio of steady-state rivulet body is large, linear velocity profile is accurate enough to present the velocity distribution within the rivulet. Flat rivulet top surfaces were observed after rivulets breaking which demonstrates the aerodynamic drag acts on the bottom of the rivulet front. The area different between the rivulet front and the rivulet body should be used to estimate the aerodynamic drag. The rivulet breaking criterion qualitatively matches with experiment result.

- Time-average rivulet thickness distributions are determined after the steady-state rivulets configurations are formed. Mass-trapping effect induced by the rivulets meandering is revealed by the observed localize rivulet humps near the meandered contact line. The initial rivulets meandering are caused by two reasons: irregular rivulet front contact line caused by the rivulet breaking, and rivulets merging. Rivulet meandering instability threshold is modeled as a simple force balance between inertia, capillary force, and aerodynamic drag. If the Weber number of a rivulet flow is smaller than 1 and the width-to-height ratio of rivulet body is bigger than 5, the force balance of meandered rivulet is further simplified to a balance between surface tension at the rivulet cross-section and the aerodynamic drag. The theoretical analysis is consistency with experiment results.

References

AI-Khalil K, Keith Jr T, De Win K (1990) Development of an Anti-Icing Runback Model. 28th Aerospace sciences meeting, Reno, NV

Birnir B, Mertens K, Putkaradze V, Vorobieff P (2008) Meandering fluid streams in the presence of flow-rate fluctuations. Physical review letters 101:114501

Bracke M, De Voeght F, Joos P (1989) The kinetics of wetting: the dynamic contact angle Trends in Colloid and Interface Science III. Springer, pp. 142-149

Cao Y, Wu Z, Xu Z (2014) Effects of rainfall on aircraft aerodynamics. Progress in Aerospace Sciences 71:85-127

Chen W-L, Tang S-R, Li H, Hu H (2012) Influence of Dynamic Properties and Position of Rivulet on Rain–Wind-Induced Vibration of Stay Cables. Journal of Bridge Engineering 18:1021-1031

Culkin JB, Davis SH (1984) Meandering of water rivulets. AIChE journal 30:263-267

Daerr A, Eggers J, Limat L, Valade N (2011) General mechanism for the meandering instability of rivulets of Newtonian fluids. Physical review letters 106:184501

Drenckhan W, Gatz S, Weaire D (2004) Wave patterns of a rivulet of surfactant solution in a Hele-Shaw cell. Physics of Fluids (1994-present) 16:3115-3121

Gorycki MA (1973) Hydraulic drag: a meander-initiating mechanism. Geological Society of America Bulletin 84:175-186

Haines P, Luers J (1983) Aerodynamic penalties of heavy rain on landing airplanes. Journal of Aircraft 20:111-119

Hansman RJ, Turnock SR (1989) Investigation of surface water behavior during glaze ice accretion. Journal of Aircraft 26:140-147

Hartley D, Murgatroyd W (1964) Criteria for the break-up of thin liquid layers flowing isothermally over solid surfaces. International Journal of Heat and Mass Transfer 7:1003-1015

Hoffman RL (1975) A study of the advancing interface. I. Interface shape in liquid—gas systems. Journal of Colloid and Interface Science 50:228-241

Johnson M, Schluter R, Miksis M, Bankoff S (1999) Experimental study of rivulet formation on an inclined plate by fluorescent imaging. Journal of Fluid Mechanics 394:339-354

Kim H-Y, Kim J-H, Kang BH (2004) Meandering instability of a rivulet. Journal of Fluid Mechanics 498:245-256

Le Grand-Piteira N, Daerr A, Limat L (2006) Meandering rivulets on a plane: A simple balance between inertia and capillarity. Physical review letters 96:254503

Liu Y, Waldman R, Hu H (2015) An Experimental Investigation on the Unsteady Heat Transfer Process over an Ice Accreting NACA 0012 Airfoil 53rd AIAA Science and Technology Forum and Exposition. Kissimmee, Florida

Marshall JS, Ettema R (2004) Rivulet Dynamics with Variable Gravity and Wind Shear. In: No.440 ITr (ed).

McAlister G, Ettema R, Marshall J (2005) Wind-driven rivulet breakoff and droplet flows in microgravity and terrestrial-gravity conditions. Journal of fluids engineering 127:257-266

Murgatroyd W (1965) The role of shear and form forces in the stability of a dry patch in two-phase film flow. International Journal of Heat and Mass Transfer 8:297-301

Nakagawa T (1992) Rivulet meanders on a smooth hydrophobic surface. International journal of multiphase flow 18:455-463

Nakagawa T, Scott JC (1984) Stream meanders on a smooth hydrophobic surface. Journal of Fluid Mechanics 149:89-99

Olsen W, Walker E (1987) Experimental evidence for modifying the current physical model for ice accretion on aircraft surfaces. NASA TM-87184

Penn DG, de Bertodano ML, Lykoudis PS, Beus SG (2001) Dry patch stability of shear driven liquid films. Journal of fluids engineering 123:857-862

Rothmayer AP, Hu H (2012) Solutions for two-dimensional instabilities of ice surfaces uniformly wetted by thin films. 4th AIAA Atmospheric and Space Environments Meeting. New Orleans, LA

Rothmayer AP, Hu H (2014) On the numerical solution of three-dimensional condensed layer films. 6th AIAA Atmospheric and space environments conference. Atlanta, GA

Saber HH, El-Genk MS (2004) On the breakup of a thin liquid film subject to interfacial shear. Journal of Fluid Mechanics 500:113-133

Tanner WF (1960) Helicoidal flow, a possible cause of meandering. Journal of Geophysical Research 65:993-995

Taylor IJ, Robertson AC (2011) Numerical simulation of the airflow–rivulet interaction associated with the rain-wind induced vibration phenomenon. Journal of Wind Engineering and Industrial Aerodynamics 99:931-944

Thompson BE, Marrochello MR (1999) Rivulet formation in surface-water flow on an airfoil in rain. AIAA journal 37:45-49

Waldman RM, Hu H (2015) High-speed imaging to quantify the transient ice accretion process on a naca 0012 airfoil.53rd AIAA Aerospace sciences meeting, Kissimmee, Florida

Zhang K, Hu H (2014) An experimental study of the wind-driven water droplet/rivulet flows over an airfoil pertinent to wind turbine icing phenomena. ASME 2014 4th Joint us-european fluids engineering division summer meeting collocated with the asme 2014 12th International conference on nanochannels, microchannels, and minichannels. american society of mechanical engineers, pp. v01dt39a001-v001dt039a001

CHAPTER 4

AN EXPERIMENTAL STUDY OF WIND-DRIVEN WATER FILM FLOWS OVER ROUGHNESS ARRAY

Abstract: Surface roughness is generated during an ice accretion process. The roughness over an ice accreting surface blocks the surface water film/rivulet flows and subsequently affects the surface water mass transport behavior. In the present study, an experimental investigation was conducted to quantify the transient behaviors of the surface water flows over rough surfaces in order to examine the water mass trapped effect due to the presence of roughness arrays. A novel digital image projection (DIP) system was developed and applied to achieve time-resolved measurements of the thickness distributions of the unsteady surface water film flows over the roughness array. PIV measurements were performed to characterize the airflow boundary layer over tested surfaces (i.e., flat plate surface, film flow surface, in front of and at back side of roughness). In comparison with the baselines of the film thickness distributions of film flow over a flat plate, the measurement results reveal clearly that, at relatively low wind speed, the mass trapped effect occurs in front of the roughness array where the roughness array would perform as a dam to block the wind-driven water film flow. For the cases with higher wind speeds, the trapped water mass was found to stagnate mainly at the backside of the roughness array. The time-averaged mass trapping ratio was found to be sensitive to the wind speed, but less sensitive to the flow rate of the water film flow. A longer roughness area will decrease the water mass trapped effect.

1. Introduction

Aircraft icing occurs when a cloud of super-cooled droplets impinge and freeze onto the airplane surfaces during flight (Gent et al. 2000). In glaze icing conditions, water beads, rivulet and film flows run back along the airfoil surface (Olsen and Walker 1987). Semi-regular roughness elements are often observed during ice accretion process (Anderson and Ruff 1998, Shin 1996). The behaviors of surface water runback flows will redistribute the impinging water mass and disturb the local flow filed, as a result, directly influence the ice accretion process. On the other hand, surface water flow will indirectly influence the ice accretion process due to its interaction with local ice surface roughness. Surface ice roughness will modify the local convective heat transfer coefficient. Furthermore, surface roughness will choke a certain amount of water mass in place near the roughness elements. Matheis and Rothmayer (2003) refer to such phenomena as the water mass trapping effects.

Wang and Rothmayer (2009) presented a numerical work to simulate thin water films and beads flow through a small roughness field. Rothmayer and Hu (2013) reported two numerical algorithms to solve the weak and strong lubrication problems for three dimensional linearized condensed layer films. The transient phenomena of thin water film flows over a roughness array were simulated in order to compare those two algorithms. However, there is no direct experimental evidence to verify the numerical simulation results related to this micro-transient phenomenon. Advanced experimental techniques capable of providing accurate measurements to qualify the interaction effects of thin film flow and roughness elements are highly desirable.

With this in mind, a novel digital image projection (DIP) system was developed and applied to achieve time-resolved measurements of the thickness distributions of the unsteady surface water film flows over a test surface for the cases with and without rough array. The DIP technique used in the present study is based on the principle of structured light triangulation in a similar manner as a stereo vision system but replacing one of the cameras for stereo imaging with a digital projector. The digital projector projects line patterns of known characteristics onto the test specimen (i.e., a water droplet/rivulet on a test plate for the present study). The pattern of the lines is modulated from the surface of the test object. By comparing the modulated pattern and a reference image, the 3D profile of the test object with respect to the reference plane (i.e., the thickness distribution of the water droplet/rivulet flow) can be retrieved quantitatively and instantaneously. The fundamental principles and more details of the technique including image correlation algorithm, displacement to height calibration procedure, accuracy verification and sample measurements about wind-driven film flow over flat plate were described in our previous paper (Zhang et al. 2013).

In order to quantitatively examine the water mass trapped effects due to the presence of the local ice roughness, in the present study, the DIP technique is used to achieve whole-field thickness measurement of the wind-driven surface water film flows over a rouged surface. The airflow boundary layers were measured by PIV technique to investigate the possible reasons of this trapped effect. Both the water mass trapping effect and the transient behaviors of surface waves are characterized based on the quantitative DIP measurement results (i.e., film thickness, water mass trapped ratio, surface wave frequency, wave length). The water mass transport behavior revealed from the present experimental study will be used to validate and verify the numerical simulation results reported in previous studies.

2. Experiment setup

Figure 4-1 illustrates the schematic of the DIP experiment setup used in the present study. The experiment was conducted in an open circuit low-speed wind tunnel. The wind tunnel has a Plexiglas test section with a dimension of 300×200×140mm (L×W×H). As shown in Fig. 4-2, a flat plate with a dimension of 250×150 mm (L×W) was flush mounted at the bottom of test section. The test models were 3D printed by using a rapid prototyping machine with white coating to enhance the diffuse reflectivity for the DIP measurements. The water film flow was injected from a water outlet holes array, which has 23 uniformly distributed liquid outlet holes. The array is located of at the entrance of the test plate model. The water outlet holes have a dimension of a array width W=7.9cm, a hole distance 3.5mm, and a hole diameter 2.0 mm. The water flow was supplied to the test model from a water tank through a flow meter (Omega FLR1010T-D), which can provide a fine measurement of the water flow rate. Two guide vanes were mounted at two sides of the test plate in order to generate a uniform water film flow on the test plate. A rounded edge was designed at the end of the test plate to ensure a smooth outflow as the water film flow left the test plate.

As suggested by (Cobelli et al. 2009), a small amount of flat white latex dye was added into the water in order to enhance the diffusive reflection on the liquid surface for the DIP measurements. It should be noted that, the addition of the dye might change the physical properties of water, which would affect the behavior of the water film flows over the test plate. However, for the present study, with a low concentration of dye premixed within water (<1.0% in volume), the effects of the added dye for DIP's measurements on the physical properties of water and the dynamic behaviors of the unsteady wind-driven surface water flows over the test plate are believed to be relatively small. In the present study, three different wind speeds 10m/s, 15m/s, 20m/s and three flow rates 12.7ml/min/cm, 25.3ml/min/cm, 38.0ml/min/cm were employed during the experiments.

For the test cases to study wind-driven water film flow over roughed surface, two insert blocks with roughness arrays, as shown in Fig. 4-2(b, c), were installed in the center of the test plate. One relatively short roughness array block has 5 rows of staggered roughness pattern whereas the longer roughness array block has 13 rows of staggered roughness pattern. The diameter of a roughness element is D=2mm. The spacing between roughness elements is 1.2D.

The height of the roughness is H_r =1mm. The corresponding H_r/δ ranged from 0.18 to 0.26, where δ is the boundary layer thickness. As suggested in (Rothmayer and Hu 2013), the roughness height distribution of a single roughness element was defined by equation (4.1),

$$h_l(x_r, y_r) = H_r \sum_{i=1}^{N} \exp\left[-\sum_{j=1}^{m} \frac{(r_i / R_i)^{2j}}{2j}\right] \tag{4.1}$$

Where N is the number of roughness elements, H_r denotes the roughness peak height, R denotes the radius of a roughness element, r_i denotes the distance from the center of ith roughness element to the point (x, y), $m = 6$ in the present study. The obtained single roughness geometry profile was used to generate the roughness array models by using Solidworks software.

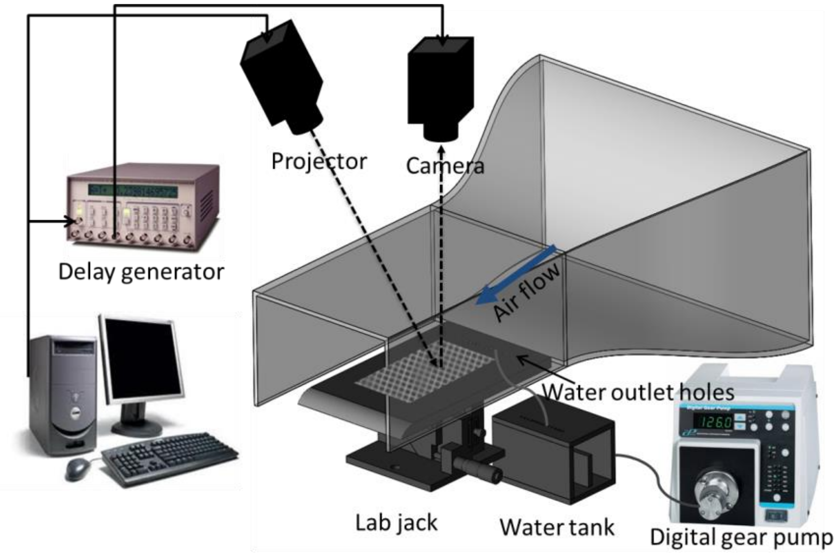

Figure 4-1 *Experiment setup used in the present study*

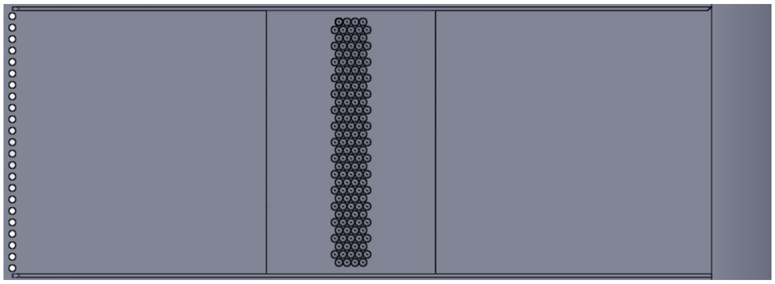

(a)

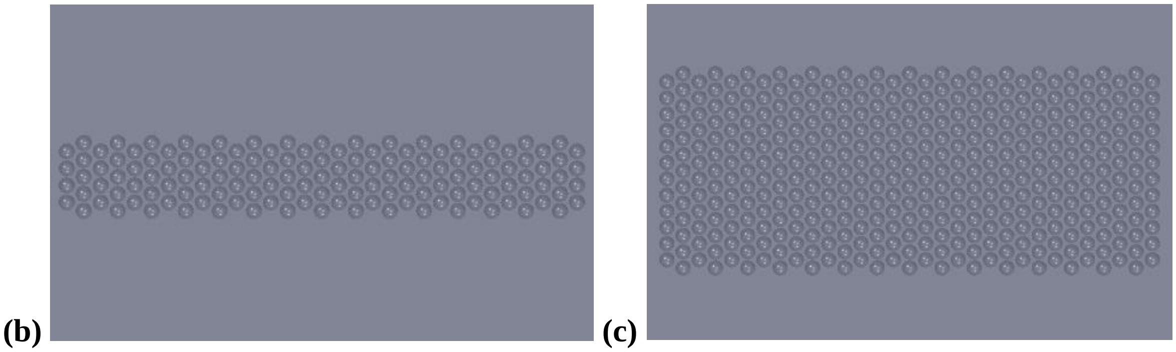

Figure 4-2 *Models used in the present study. (a) Test plate geometry. (b) Zoom-in view of the short roughness array. (c) Zoom-in view of long roughness array.*

In the present study, A Digital DLP projector was used to project grid cross line into the test plate. A CCD camera (1280×1024) with a M3514-MP lens (F/1.4, f=16mm) were used for the image acquisition. The CCD camera and the projector were synchronized by using a digital delay generator. The frame rate of the CCD camera was set to 60.0 Hz with 1.5ms exposure time. The measurement window was centered at the roughness array center with a window size of approximately 80mm×64mm. The projected grid size was about 15×15 pixels (i.e., 1×1mm in physical domain), which was also the interrogation window size of the cross-correlation calculation used during the data processing of the DIP measurements. The CCD camera and the projector were aligned along the spanwise direction in order to suppress the strong mirror reflection on the water film surfaces.

During the experiments, a relatively low free stream velocity of the airflow (i.e., $U_\infty = 5m/s$) and relatively high water flow rate (i.e., water flow rate of $q = 38.0ml/min/cm$) were used to enable the water flow to wet the whole test plate at first. Then, the wind speed was adjusted to 20m/s to generate uniform thin water film flow on the test plate. Finally, the wind speed and water flow rate were set to the desired values. For each test case, 600 images (10s) were collected after the water film flow reached to the steady state condition. The DIP image processing was performed by correlating each acquired image with the reference image to determine the film thickness distributions instantaneously. The obtained DIP measurement results were interpolated to regular grid points for further analysis. It should be noted that the wind-driven film thickness is very thin (<1mm). Although, the test plate was carefully adjusted to be leveled with the wind tunnel bottom, the obtained film thicknesses were not the same if the test plate was reinstalled in the wind tunnel. This inconsistency will cause a bias error for the values of water mass trapped ratio. The film flows over the flat plate without the roughness array were measured twice to guarantee that the comparison between film flow over the flat plate and over the short roughness array as well as the comparison between the film flow over the flat plate and over long roughness array are two measurement pairs. Due to the shadow effect caused by the roughness array, the DIP measurement results within the roughness range were not accurate. In the following section, those DIP measurement results are provided only as a reference.

The water film flows over the test plate were driven by the airflow through the shear stress at the air-water interface. In the present study, a high-resolution digital Particle Image Velocimetry (PIV) system was used to reveal the flow characteristics of the boundary layers over the film surface and over roughness arrays. Figure 4-3 shows the schematic of experimental setup used for the PIV measurements. During the PIV measurements, the airflow was seeded with ~1μm oil droplets by using a fog generator. Illumination was provided by a double-pulsed Nd:YAG laser (New wave Gemini 200) adjusted on the second harmonic and emitting two pulses of 200 mJ at the wavelength of 532 nm. A high-resolution 14-bit CCD camera (PCO. 2000) was used for PIV image acquisition with the axis of the camera perpendicular to the laser sheet. The CCD camera and the double-pulsed Nd:YAG laser were connected to a host computer via a digital delay generator (BNC565), which controlled the timing of the laser illumination. For the PIV image processing, flow velocity vectors were obtained using a frame-to-frame cross-correlation technique involving successive frames of image patterns of particle in an interrogation window of 32×32 pixels. An effective overlap of 50% of interrogation windows was employed in the PIV processing. After the instantaneous velocity vectors were derived, time-averaged velocity distribution were obtained from a time sequence of 450 images of instantaneous PIV measurement results.

In the present study, the characteristics of the airflow boundary layer were measured under the free stream velocities $U_\infty = 10m/s$, $U_\infty = 15m/s$ and $U_\infty = 20m/s$. A small amount of flat white latex dye (<1% in volume) was added into the water as well, which kept the water flow conditions of PIV measurements consistent with DIP measurements. Only one film flow rate $q = 25.3ml/min/cm$ was tested which is thought to be the representation of airflow over film flows. Airflow boundary layers over the flat plate, in front of and behind the long/short roughness arrays were measured. For the flat plate boundary layer measurements, the PIV measurement windows were located in the center of the test plate (blue window in Fig. 4-3), which is 125mm away from the inlet of test plate. The size of the PIV measurement window is about 20×20mm with spatial resolution about 0.16×0.16mm. For roughness array boundary layer measurements, the PIV measurement windows were located in front of and behind the roughness array (red windows in Fig. 4-3). The laser sheet was carefully aligned to the center of the roughness arrays. In order to protect the camera, the measurement windows were set to about 0.1-1mm above the film flow. Airflow boundary layers without film flow were also measured as reference boundary layers.

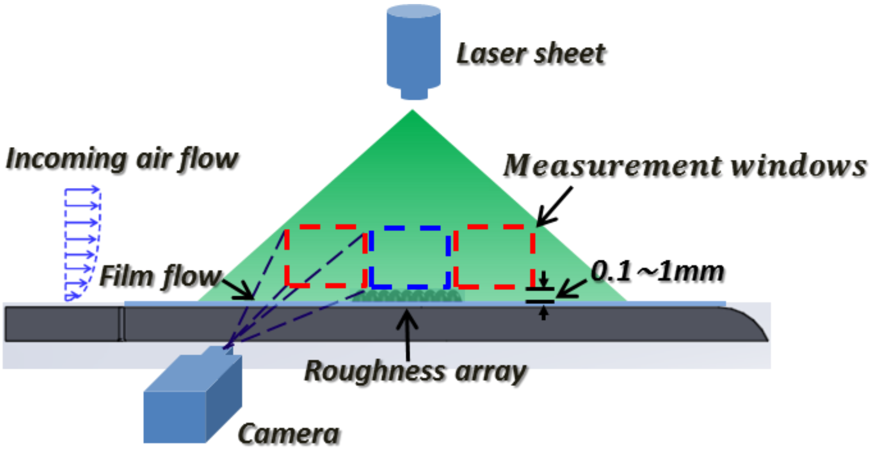

Figure 4-3 *Schematic experimental set up used for PIV measurement*

3. Airflow boundary layer above the surface water film flows

3.1. Effects of water film flow on the boundary layer profile

Figure 4-4 shows the time-averaged flow velocity distribution within the airflow boundary layer over the flat plate model without water film flow. In Fig. 4-4, y denotes the distance away from the flat plate surface. s denotes the stream wise direction where $s/d = 0$ is the center of the measurement windows. As described in the experiment setup, the measurement window was located 125mm away from the leading edge of the test plate model. δ denotes the 0.99 boundary layer thickness. D denotes the diameter of the roughness element. The axes in Fig.4-4 were normalized by the boundary layer thickness and the roughness diameter respectively. The boundary layer thickness (at the location $s/D = 0$) of free stream velocity $U_\infty = 10m/s$ was found to be about 2.8mm, while the boundary layer thickness of the airflow free stream velocity $U_\infty = 20m/s$ was about 2.2mm. Seen from Fig. 4-4, the boundary velocity distributions are similar to laminar flow velocity distribution. Laminar flow boundary layer was supposed and equation (4.2) was used to predict the value of x, which is the equivalent distance away from the leading edge of a semi-infinite flat plate.

$$x = \frac{\rho_a U_\infty \delta^2}{25.0\mu_a} \tag{4.2}$$

The obtained x values were then used to calculate the η value by the transform of $\eta = y\sqrt{U_\infty/\nu_a x}$. By extracting the time-averaged PIV measurements data along the line of $s/D = 0$, the measurement airflow velocity profiles within the boundary layer were compared with the Blasius solution. The comparison is plotted in Fig. 4-4(d). The experimental curves are almost identical with the Blasius solution. On the other hand, the boundary layer shape factors were found around 2.7 for the current study (2.6 for laminar flow boundary). Obviously, the boundary layers of airflow over the flat plat without water film flow were laminar flow boundary layer. The transition of a semi-infinite flat plate occurs at a critical Reynolds number $Re_{x,crit} \sim 3.5 \times 10^5 - 10^6$ (Schlichting and Gersten 2000). The Reynolds numbers of the current study based on the calculated distance x were about $Re_x \sim 1.6 - 4.0 \times 10^5$, which were close to the lower limit of the critical transition Reynolds number. The turbulence intensity of the tunnel used in the current study was about 0.35% (at the center of test section). The surface of the test plate was carefully wet-sanded to smooth finish using 2000 grit sandpaper. The obtained laminar flow boundary layer profile was predictable. In the following discussion, the measurement boundary layer profiles over the flat plate without film flow are used as the standard laminar boundary layer profiles.

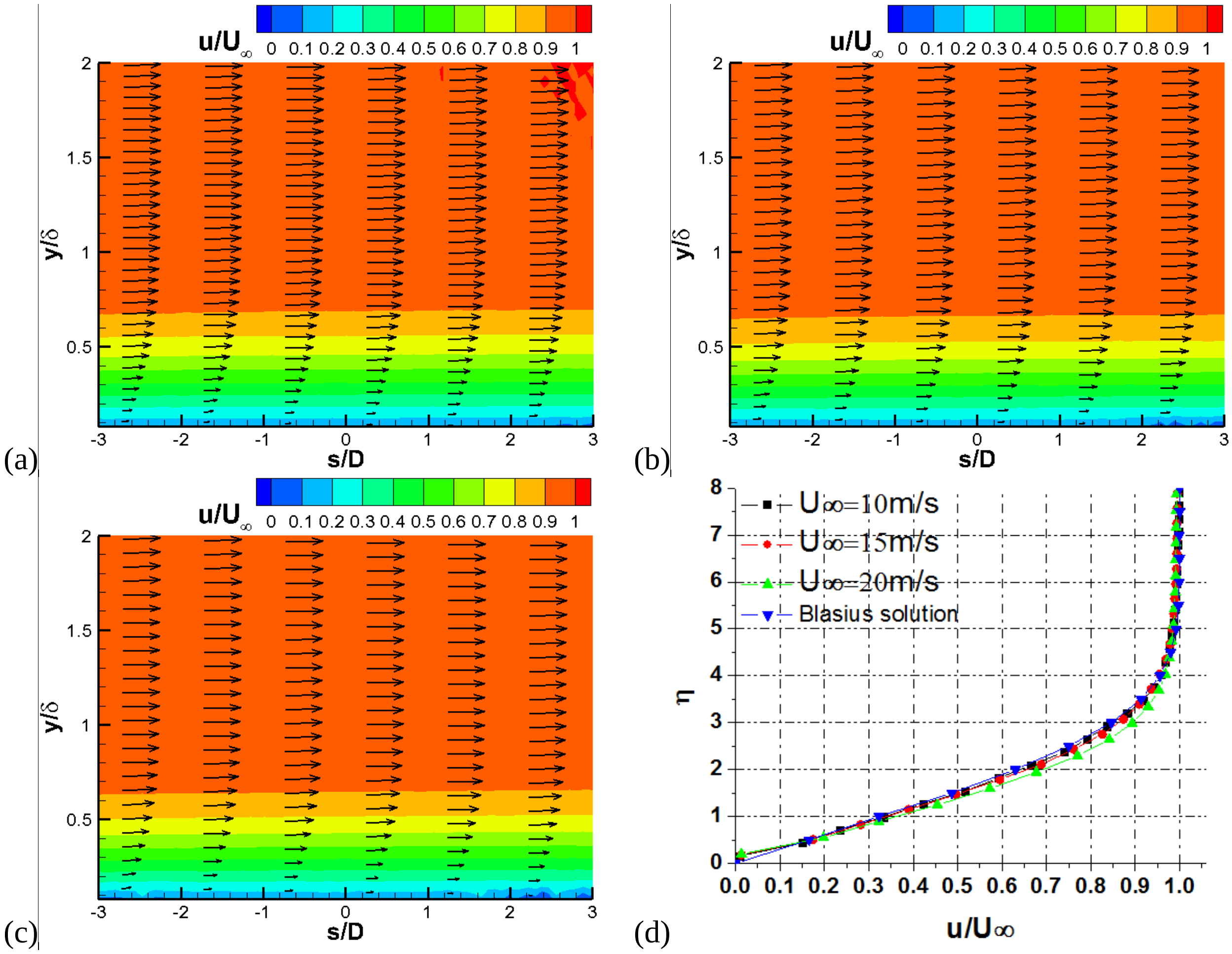

Figure 4-4 *Time-averaged PIV measurement results of the airflow boundary layer above flat plate without water film flow. (a)* $U_\infty = 10m/s$*. (b)* $U_\infty = 15m/s$*. (c)* $U_\infty = 20m/s$*. (d) Comparison of velocity profile with Blasius solution*

Figure 4-5 shows the effects of the water film flow on the airflow boundary under low free stream velocity (i.e., $U_\infty = 10m/s$). Figure 4-5(a) shows the instantaneous boundary layer velocity distribution over the flat plate without film flow. Figure 4-5(b) and (c) show the instantaneous airflow boundary layer velocity distribution at different times over the water film surface. Figure 4-5(d) shows the repeatability of the experiment by comparing three runs of measurements. As discussed above, Fig. 4-5(a) can be considered as a typical instantaneous laminar flow boundary layer velocity distribution. Figure 4-5(b) is generally the same as Figure 4-5(a), whereas turbulence boundary layer features were observed in Fig. 4-5(c). The velocity distributions shown in Fig. 4-5(b) and (c) were from snapshots of the same experiment (3^{rd} experiment shown in Fig. 4-5(d)). The change of boundary layer style proves that the airflow boundary layer was sometimes a laminar boundary layer and sometimes a turbulent boundary layer, which is the typical intermittent behavior during the laminar to turbulent transition process. The boundary layer thicknesses on the film flow were much larger than the corresponding boundary layer thicknesses on the flat plate without film flow (e.g., 5.2mm vs 2.8mm). The shape factors of the cases with film flow were around 1.8 which is a typical shape factor for transition flow. Those features all demonstrate the film flow could induce laminar to turbulent transition. Fig. 4(d) shows that the transition process is random and may not happen. Three repeated experiments were performed to check the transition behavior. Transition behavior only happens during one of the experiments. The time-average boundary layer profile of the transition one is in between laminar boundary layer profile and $1/7^{th}$ power law profile which is considered as fully developed turbulent.

This transition behavior is believed to be induced at the upstream water outlet position where the water layer thickness was much larger than the local boundary layer thickness. The maximum Reynolds number of the current study is about $Re_x \sim 4.0 \times 10^5$ which is just slightly larger than the lower limit of the critical transition Reynolds number $Re_{x,crit} \sim 3.5 \times 10^5$. The transition process was initialed randomly for all three free stream velocities. Figure 4-6 shows the time-averaged boundary velocity distributions over the flat plate with film flow. The distributions shown in Fig. 4-6 were obtained from the same experiment (the third experiment in Fig. 4-5(d)). For all three velocities, the velocity distribution is similar. However seen from the boundary layer profiles, the profile of the $U_\infty = 20m/s$ case is closer to a fully turbulent profile. Once the transition was not happened, the effect of film flow was found to increase the turbulence intensity within the boundary layer and increase the boundary layer thickness. However, both the turbulence intensity and boundary layer thickness were much smaller than the transition boundary case values.

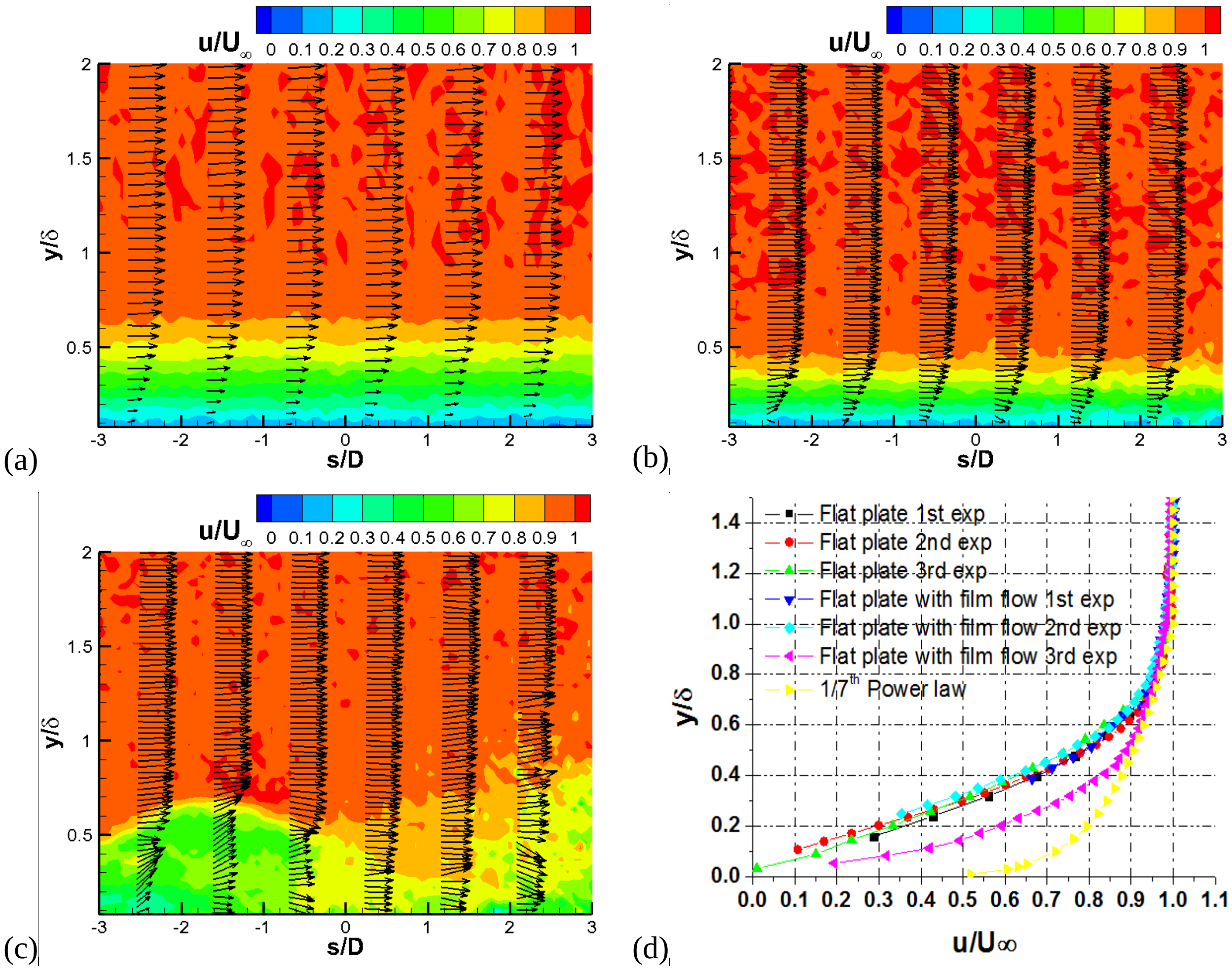

Figure 4-5 *Intermittent phenomenon of boundary layer over film flow under free stream velocity* $U_\infty = 10m/s$, *estimated (a) Instantaneous laminar flow boundary layer over flat plate without film flow. (b) Instantaneous laminar flow like boundary over flat plate with film flow. (c) Turbulent boundary layer over flat plate with film flow (snapshot in the same experiment of case (b)). (d) Time-average boundary layer profiles over flat plate*

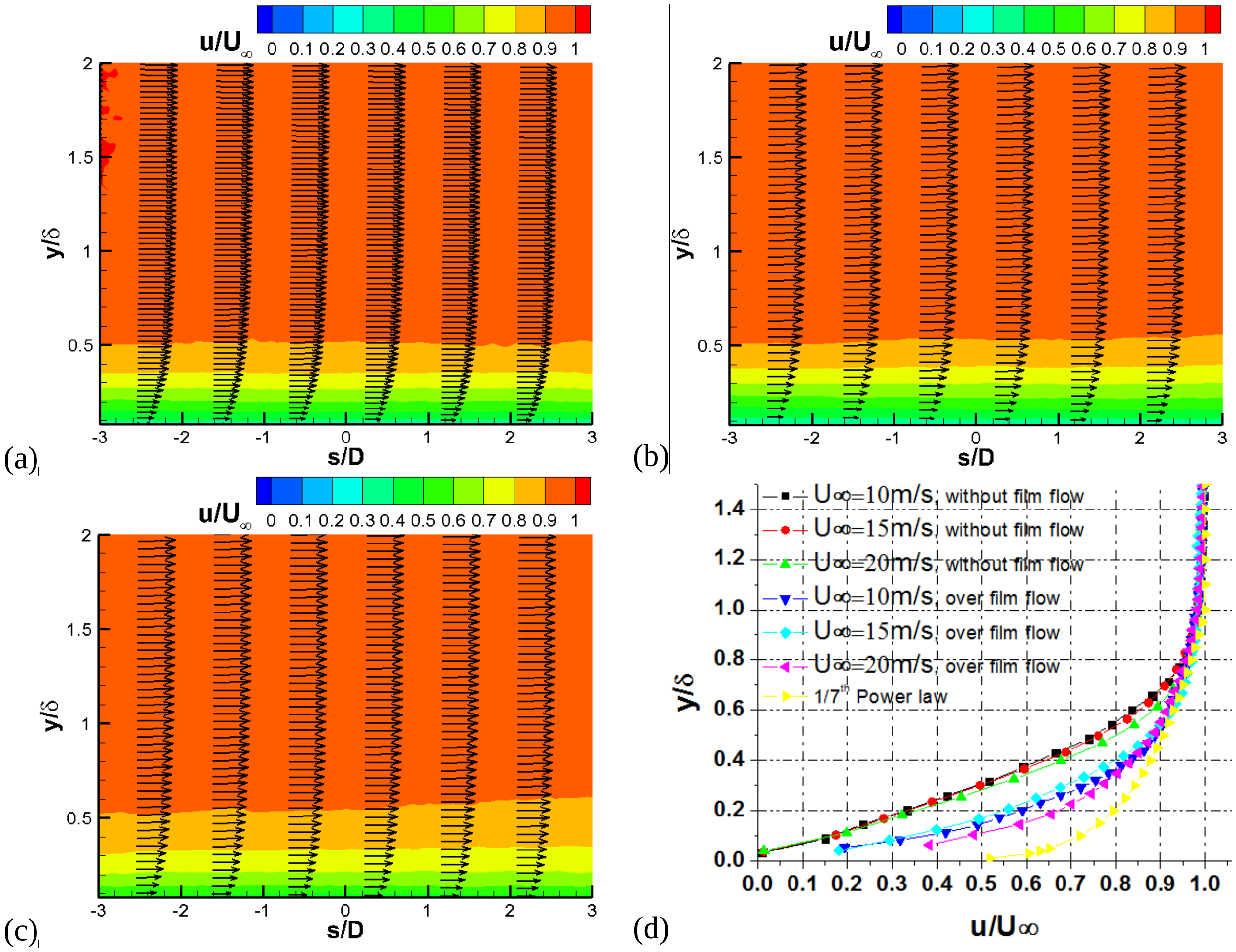

Figure 4-6 *Time-average airflow boundary layer over flat plate with film flow. (a)* $U_\infty = 10m/s$ *(b)* $U_\infty = 15m/s$ *(c)* $U_\infty = 20m/s$ *(d) Time-average velocity profiles over flat plate*

3.2. Effects of surface roughness on boundary layer

Figure 4-7 shows the velocity distributions in front of and at the back side of the roughness array. In Fig. 4-7, s is also the local coordinate along the stream wise direction but the origin point is located at the edge of the roughness array. In order to compare the flow features of both short and long roughness array, both s and y coordinate were normalized by the diameter of roughness array element ($D = 2mm$). The free stream velocity $U_\infty = 20m/s$ is selected to reveal the influences of roughness shape on the boundary layer flow. Seen from Fig. 4-7, the boundary layer velocity distributions of the short roughness and the long roughness were similar. The first column of Fig. 4-7 shows the flow field in front of roughness arrays. It can be seen that the roughness arrays can only influence the boundary layer flow at the range where the airflow approaches the roughness. The second column of Fig. 4-7 shows the flow field at the back side of the roughness arrays. Flow separations were detected right behind the roughness. The separation range can reach the downstream location at about $s/d = 4$. This observation is in agreement with Winkler and Braggair's work (1996) where the flow separation behind a roughness element was detected as well. The boundary layer was raised up by the separation range and recovered to the laminar flow boundary at $s/d = 4$. The normalized turbulent kinetic energy (TKE) distributions behind the roughness arrays are given in Fig. 4-8. The TKE value of flow field behind long roughness array was much higher than the TKE value behind short roughness array, which is predictable.

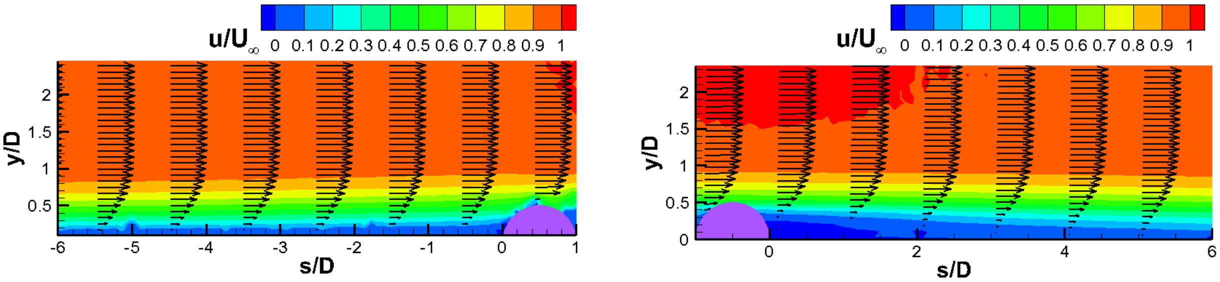

(a) In front of roughness (b) Back side of roughness

A. Short roughness array

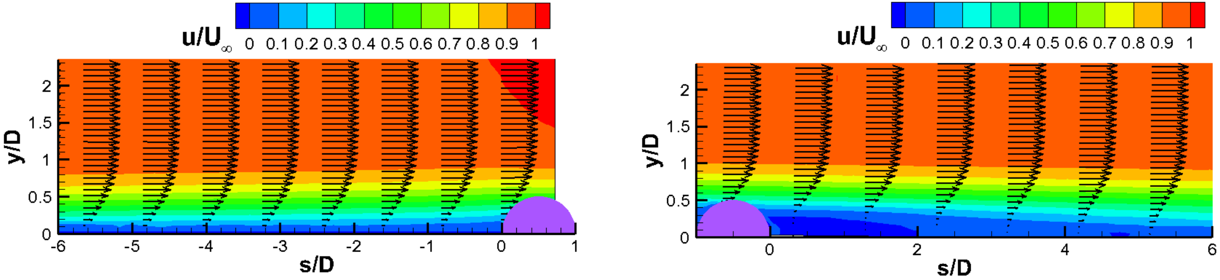

(a) In front of roughness (b) Back side of roughness

B. Long roughness array

Figure 4-7 *Time-averaged velocity distribution in front of and after the roughness array at free stream velocity* $U_\infty = 20m/s$

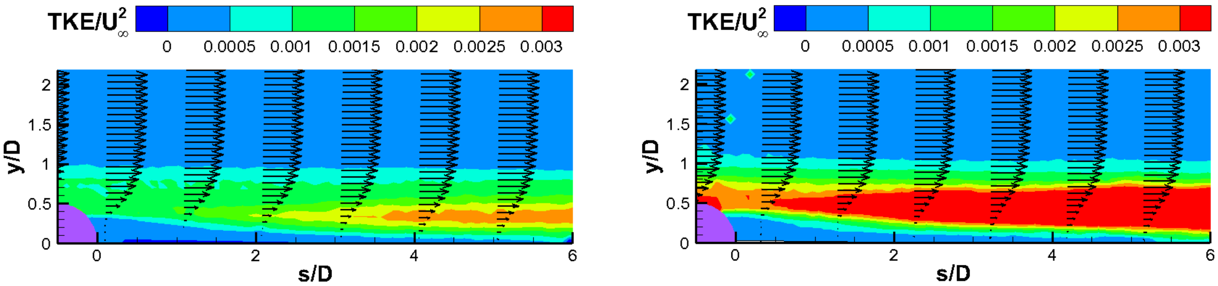

(a) In front of roughness (b) Back side of roughness

B. Long roughness array

Figure 4-8 *Turbulence intensity distribution at the back side of the roughness array at free stream velocity* $U_\infty = 20m/s$

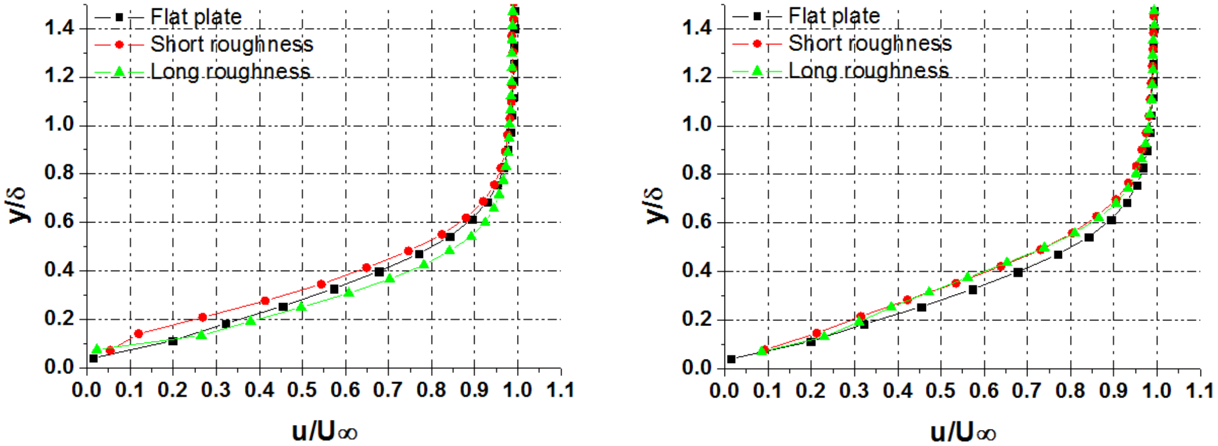

(a) In front of roughness (b) Back side of roughness

Figure 4-9 *Time-average boundary layer velocity profiles in front of and at the back side of roughness for experiment case* $U_\infty = 20m/s$ *without film flow. The location of the velocity profile is* $s/D = -8$ *in front of the roughness and* $s/D = 8$ *at the back side of roughness*

Figure 4-9 gives the boundary layer profiles far away from the roughness arrays. Fig. 4-9(a) exhibits the boundary layer profiles at location $s/d = -9$ which is in front of the roughness array whereas Fig. 4-9(b) shows the boundary layer profiles at location $s/d = 9$ which is at the back side of roughness array. For both short and long roughness array cases, the boundary layer profiles were matched with the laminar flow boundary profile. No transition behavior was observed during the tests. Actually for both short and long roughness case, when the boundary layer flow field were far away from the roughness arrays ($|s/d| > 4$), the boundary layer thickness in front of roughness were equal to the boundary layer thickness at the back side of the roughness array. However, compared with boundary layer thickness value without a roughness array, the boundary layer thicknesses with the roughness arrays were about 20% thicker. The results indicate that the roughness array only influence the boundary at a limited range of $0< s/d<4$. Outside this range the boundary layer is similar to the boundary layer without roughness array.

3.3. Boundary layer profiles in front and at back side of roughness with film flow

The combination effects of the roughness array and film flow on the airflow boundary layer are illustrated in Fig. 4-10. The first column of Fig. 4-10 shows the boundary layer profiles at location $s/d = -8$ (in front of the roughness array). The second column of Fig. 4-10 shows the boundary layer profiles at location $s/d = 8$ (at back side of the roughness array). Seen from Fig. 4-10(A), at low wind speed $U_\infty = 10m/s$, the boundary profiles were generally laminar flow boundary layer profiles. For wind speed $U_\infty = 15m/s$ cases, the boundary layer profiles in front of the roughness arrays were laminar boundary layer profiles as well. However, laminar to turbulent transition happened at the back side of the roughness arrays. Moreover, the boundary layer profile of the long roughness array case was closer to fully developed turbulent which means higher shear stress at water-air interface. The wind speed $U_\infty = 20m/s$ cases exhibits the same trend as the $U_\infty = 15m/s$ cases. In summary, the combination of roughness array and film flow could induce flow transition.

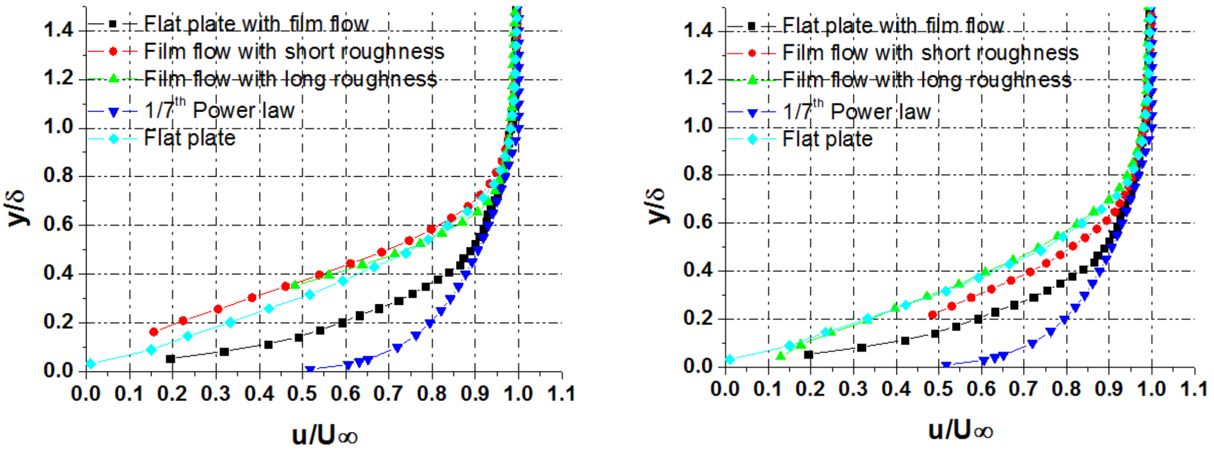

a. In front of roughness b. Back side of roughness

A. $U_\infty = 10 m/s$

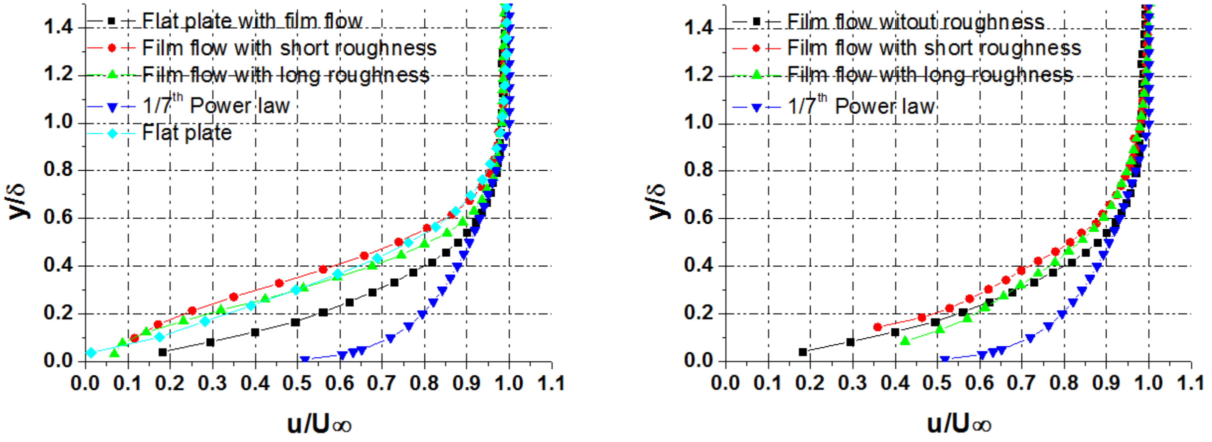

a. In front of roughness b. Back side of roughness

B. $U_\infty = 15 m/s$

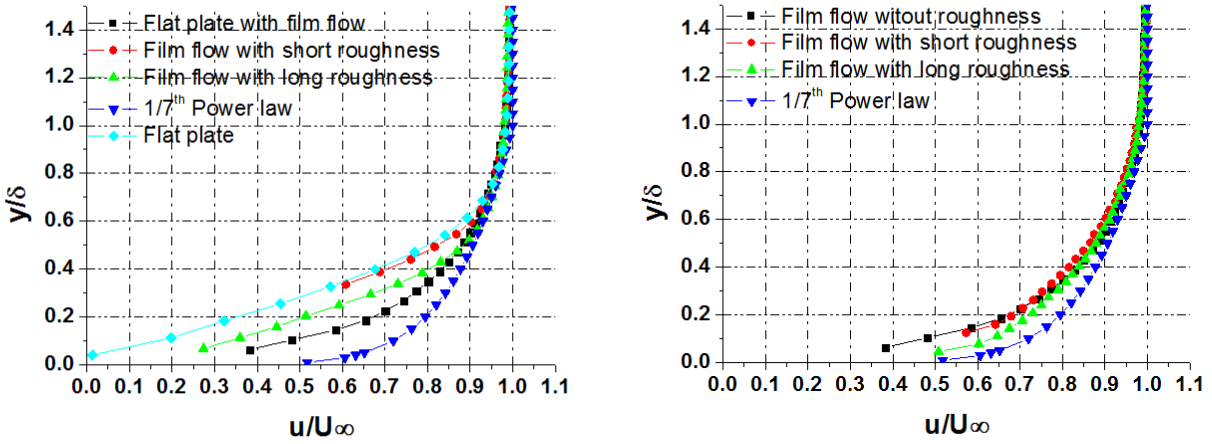

a. In front of roughness b. Back side of roughness

C. $U_\infty = 20 m/s$

Figure 4-10 *Time-average boundary layer velocity profiles in front of and at the back side of roughness for experiment cases with film flow. The location of the velocity profile is* $s/D = -8$ *in front of the roughness and* $s/D = 8$ *at the back side of roughness*

4. Film flow over roughness and water mass trapped ratio

4.1. Transient behavior of the water film flows over flat plate with and without the roughness array

Figure 4-11 shows the instantaneous film thickness distributions of the cases that wind-driven water film flows over the test plates without the roughness array. Water flow rate $q = 25.3ml/min/cm$ is selected to represent the transient behaviors of the film flow. The measurement coordinate is normalized by the diameter of the roughness element $D = 2mm$. L denotes the distance from the center of the roughness array along the stream wise direction. W denotes the distance away from the centerline of the test plate. The origin point of the coordinate is located at the center of the roughness array. The flow structures of the film flow over the flat plate without roughness can be considered as the reference to study the behaviors of the water film flows passing through roughness arrays. As shown in the Fig. 4-11, regular, long wavelength, 2D surface water waves were observed under free stream velocity $U_\infty = 10m/s$. As the free stream velocity increases to $15m/s$, the surface water waves were found to exhibit as sharp-crest shallow water waves, which demonstrates the free surface motion is disturbed by the bottom of the test plate. Meanwhile, the wave fronts broke along the spanwise direction. Figure 4-11(b) shows the spanwise wave crest separation process at the free stream velocity $U_\infty = 15m/s$. Tiny arc shape wave fronts were observed under free stream velocity $U_\infty = 20m/s$. Those tiny waves were randomly distributed within the entire film flow range. The DIP measurements were also conducted at the water film flow rate $q = 12.7ml/min/cm$ and $q = 38.0ml/min/cm$. Although the propagation speeds and frequencies of the water surface waves were found to decrease with increasing water flow rates, the behaviors of the wind-driven water film flows of cases $q = 12.7ml/min/cm$ and $q = 38.0ml/min/cm$ were found to be very similar to behaviors of the $q = 25.3ml/min/cm$ case in general. In summary, the transient behaviors of the wind-driven water film flow over the flat plate seem to be more sensitive to the free stream speed of the airflow and less sensitive to the water film flow rate.

The instantaneous film thickness distributions of the water film flow over the test plate with the short roughness array and long roughness array are displayed in Fig. 4-12 and 4-13 respectively. The flow behaviors of the short roughness cases were similar to behaviors of the long roughness cases. As shown in Fig. 4-12, the roughness array performed as a dam for the water film flow when the free stream speed was relatively low (i.e., $U_\infty = 10m/s$). The film thickness in front of the roughness array was found to be much thicker than the corresponding film thickness without the roughness array. For the cases under higher airflow free stream velocities, the surface water was found to accumulate downstream of the roughness array. As shown in Fig. 4-7, airflow separation was detected right after the roughness array. The water mass accumulation near the roughness array observed in the present study is believed to be closely related to the airflow separation behind the roughness elements. As shown in Fig. 4-12b and Fig. 4-12c, water tended to flow between the roughness elements, as a result, span wise humps could be observed along the downstream trapped water line. Surface wave structures exhibited similar behaviors as the cases of the water film flows over the flat plate without roughness. 2D regular waves showed up at the air-water interface at low wind speed as well. Those 2D waves were found to be interrupted by the roughness array, however, appeared again at the downstream range. Irregular sharp-crest waves were detected for the cases with higher wind speeds.

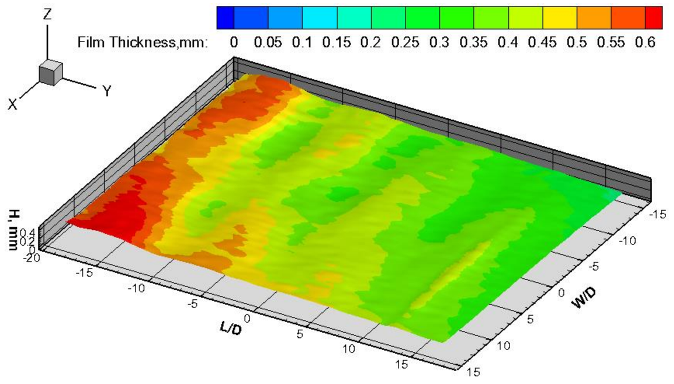

(a) $U_{\infty} = 10m/s$

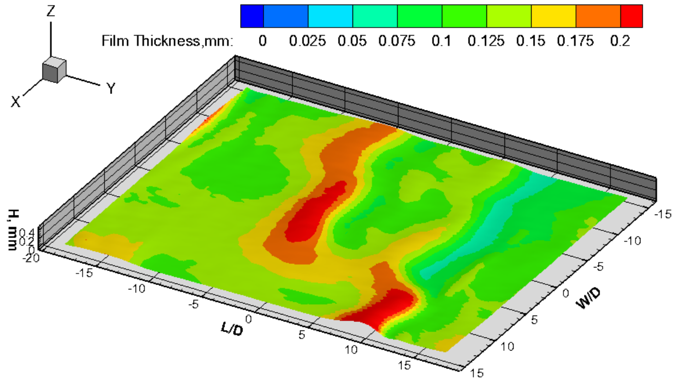

(b) $U_{\infty} = 15m/s$

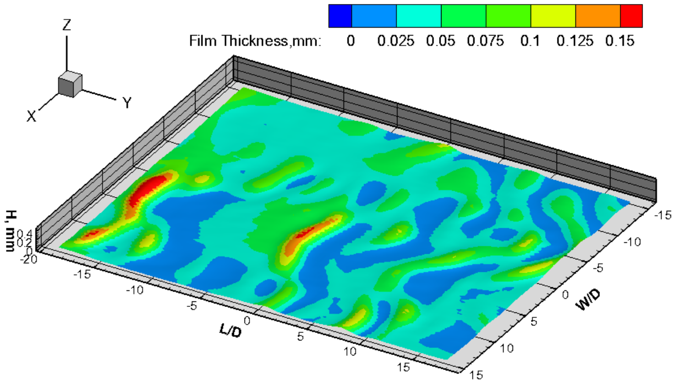

(c) $U_{\infty} = 20m/s$

Figure 4-11 *Instantaneous film thickness measurement results of the wind-driven water film flow over flat plate at the water flow rate of q=25.3 ml/min/cm*

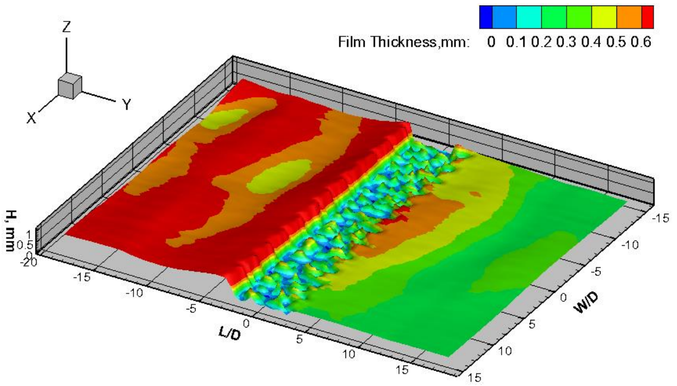

(a) $U_\infty = 10m/s$

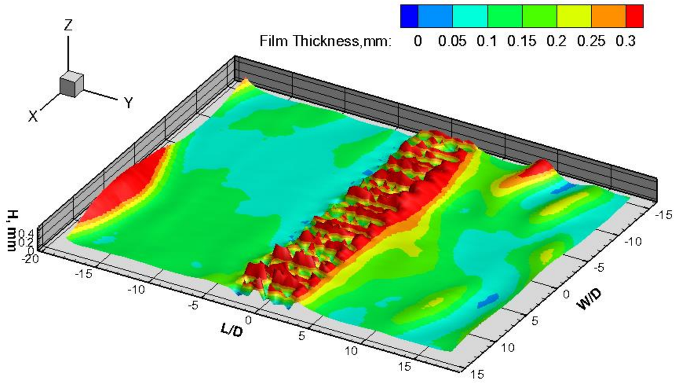

(b) $U_\infty = 15m/s$

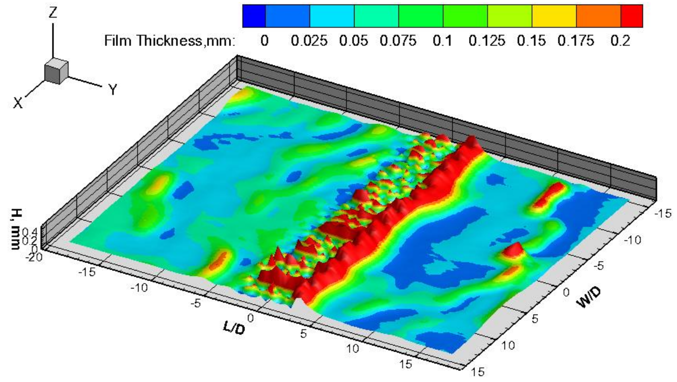

(c) $U_\infty = 20m/s$

Figure 4-12 *Instantaneous film thickness measurement results of the wind-driven water film flow over short roughness at the water flow rate of q=25.3 ml/min/cm*

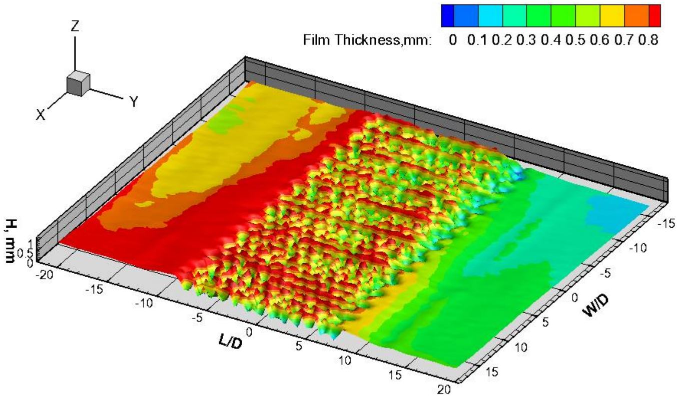

(a) $U_\infty = 10m/s$

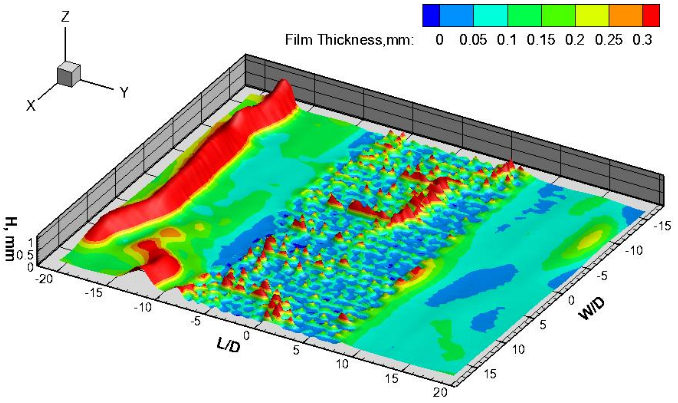

(b) $U_\infty = 15m/s$

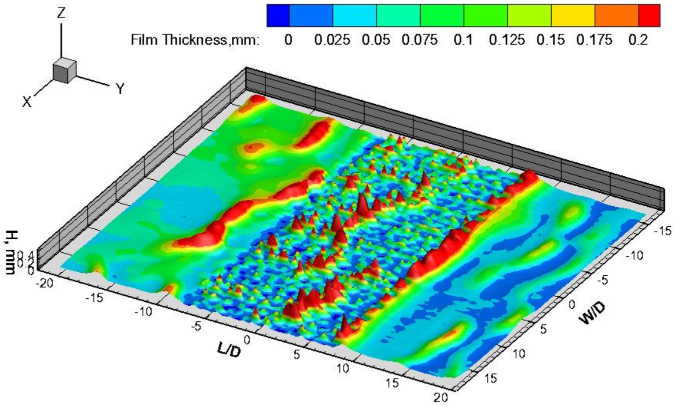

(c) $U_\infty = 20m/s$

Figure 4-13 *Instantaneous film thickness measurement results of the wind-driven water film flow over long roughness at the water flow rate of q=25.3 ml/min/cm*

4.2. Power spectrum analysis of the water surface waves

Based on the time sequences of the instantaneous DIP measurement results which were given in Fig. 4-11-4-13, a power spectrum analysis of the water film thickness was also performed to reveal the characteristics of the surface water waves under different test conditions. As shown in

Fig. 4-14, the DIP measurement results at three typical locations, Point #1 upstream of the roughness array (i.e., at $L/D = -16, W/D = 0$), Point#2 at the center of the roughness array (i.e., at $L/D = 0, W/D = 0$), and Point#3 downstream of the roughness array (i.e., at $L/D = 16, W/D = 0$), were chosen to carry out the power spectrum analysis through a Fast Fourier Transform (FFT) procedure. It should be noted that, since the frame rate of the CCD camera was set to 60 Hz for the DIP measurements and 600 images were captured for each test case, the maximum identifiable frequency of the current measurement is 30Hz with a temporal resolution of 0.1Hz.

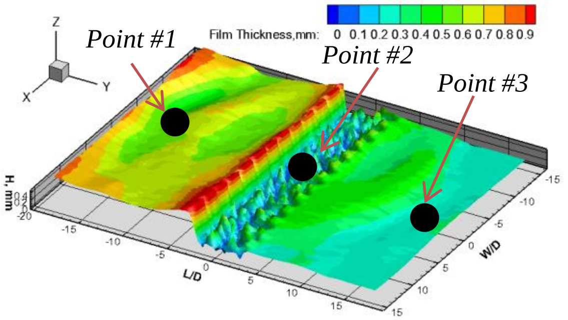

Locations of the three compared points

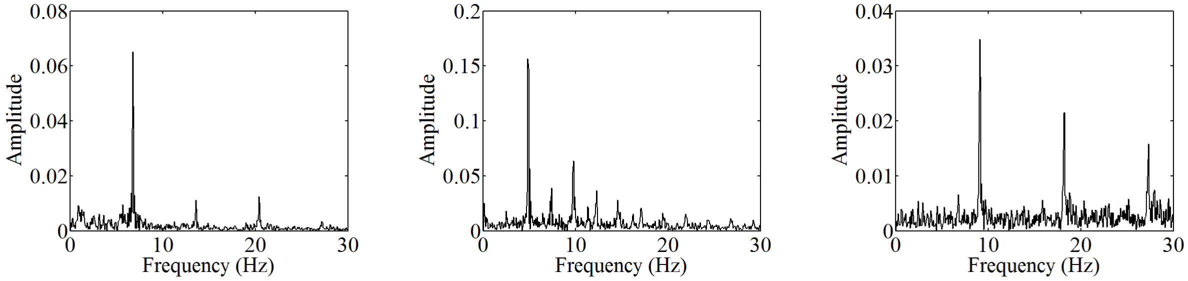

c. $U_\infty = 10m/s$ d. $U_\infty = 15m/s$ e. $U_\infty = 20m/s$

Figure 4-14 *Power spectra of the water film thickness at the point # 1 with the airflow free stream velocity changing from* $U_\infty = 10m/s$ *to* $U_\infty = 20m/s$ *and the water film flow rate being kept at* $q = 25.3ml/min/cm$.

Figure 4-14 gives the power spectrum of the water film over the flat plate at the upstream location point #1 (i.e., at L/D=-16, W/D=0) with airflow free stream velocity changing from

$U_\infty = 10m/s$ to $U_\infty = 20m/s$. The water film flow rate was kept constant at $q = 25.3ml/min/cm$. As shown in Fig. 4-14(a), with the airflow free stream velocity being relatively low (i.e., $U_\infty = 10m/s$), a well-defined peak at the dominant frequency of f_1= 6.8 Hz can be identified from the power spectrum plot, which corresponds to the propagation frequency of the 2D regular water surface waves shown in Fig. 4-11(a). As the free stream velocity increased from 10m/s to 15m/s, although the surface wave displayed as isolated long wave features, the generated wave was still periodic wave. The dominant frequencies of the water surface waves can still be identified from the power spectrum plot. The dominant wave frequency for the wind speed $U_\infty = 15m/s$ case was found to become f_1= 4.9 Hz, which was much lower than the frequency of the $U_\infty = 10m/s$ case. As the airflow free stream velocity further increased to $U_\infty = 20m/s$, the wave broke along the spanwise direction and generated many local arc wave fronts. Those small wave fronts were considered as isolated waves as well. The dominant wave frequency was f_1= 9.0 Hz which is much larger than the wave frequencies of lower free stream conditions.

Figure 4-15 gives the power spectrum plots of the water film flow over the test plate with and without the roughness array under condition of free stream velocity $U_\infty = 10m/s$ and water film flow rate $q = 25.3ml/min/cm$. It can be seen that, the dominant frequencies of the water surface waves were found to stay the same as the surface waves were propagating downstream. Very similar scenarios were found for the wind-driven water film flow passing through the roughness array. The result demonstrates that both short and long roughness array will not change the surface wave propagation frequency. Even at the center of the roughness array (e.g., at the point#2 with L/D=0, W/D=0), the dominant frequencies of the water surface waves are still the same, as shown clearly in Fig. 4-15.(B), (C).

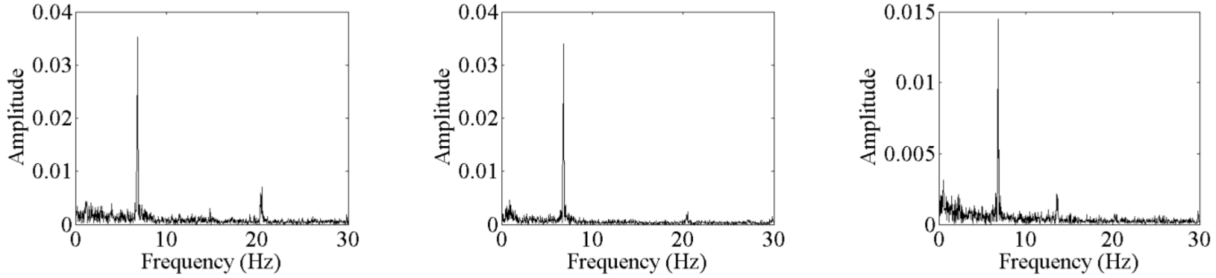

(a) Point #1 (b) Point #2 (c) Point #3

A. Wind-driven water film flow over the flat plate

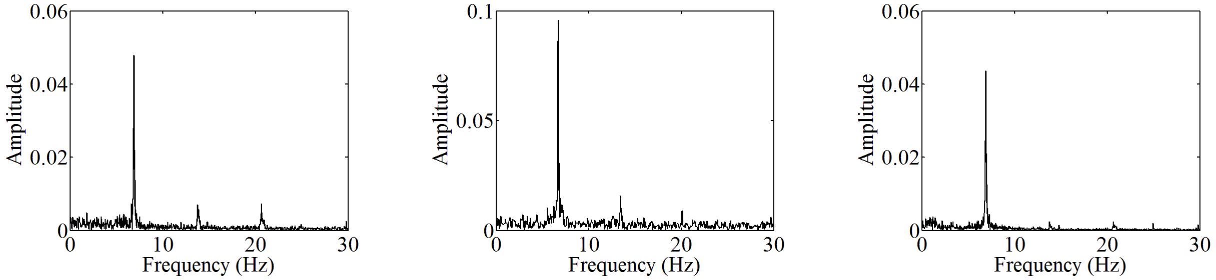

(a) Point #1 (b) Point #2 (b) Point #3

B. Wind-driven water film flow over the flat plate with short roughness

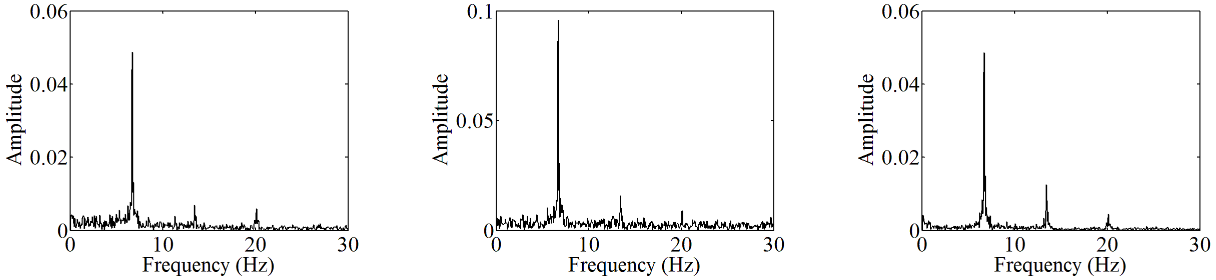

(a) Point #1 (b) Point #2 (b) Point #3

C. Wind-driven water film flow over the flat plate with long roughness

Figure 4-15 *The power spectrum plots of the water film flow over the test plate with and without the roughness array with the airflow free stream velocity* $U_\infty = 10m/s$ *and water film flow rate* $q = 25.3ml/min/cm$

Table 1 *The dominant frequencies of the water surface waves of short roughness condition*

U_∞ (m/s)	q (ml/min/cm)	$\bar{h}$ (mm)	$\overline{h_r}$ (mm)	f_1 (Hz)	f_2 (Hz)
10	12.7	0.34	0.44	6.0	6.1
10	25.3	0.52	0.64	6.8	6.8
10	38.0	0.67	0.82	7.3	7.4
15	25.3	0.17	0.16	4.8	4.7
15	38.0	0.21	0.20	5.4	5.3

Table 2 *The dominant frequencies of the water surface waves of long roughness condition*

U_∞ (m/s)	q (ml/min/cm)	$\bar{h}$ (mm)	$\overline{h_r}$ (mm)	f_1 (Hz)	f_2 (Hz)
10	12.7	0.47	0.47	5.8	5.7
10	25.3	0.7	0.69	6.8	6.7
10	38.0	0.83	0.83	7.4	7.1
15	25.3	0.15	0.21	4.9	4.6
15	38.0	0.23	0.25	5.5	5.3
20	25.3	0.07	0.07	9.0	8.6
20	38.0	0.10	0.10	10.4	9.7

Based on the power spectrum analysis results, the dominant frequencies of the wind-driven water surface waves at different test conditions can be obtained, which are listed in Table 1 and 2. Table 1 shows the comparison of dominant frequencies between film flow over flat plate without roughness array and film flow over flat plate with short roughness array. Table 2 shows the comparison of dominant frequencies between film flow over flat plate without roughness array and film flow over flat plate with long roughness array. As discussed in the experiment setup section, the measurements on film flow over flat plate were performed twice. The first column and second column in Table 1 and 2 show the airflow free stream speed and the unit width flow rate of the water film flow, respectively. In Table 1 and 2, $\bar{h}$ denotes the time-averaged film thickness of water film flow at the measurement point #1 (i.e., at $L/D = -16, W/D = 0$) for the test cases without roughness array on the test plate, $\overline{h_r}$ denotes the time-averaged film thickness of the water film flow at the same measurement point #1 for the test cases with the roughness array on the test plate. f_1 is the dominant frequency of the water surface waves for the cases without the roughness array, f_2 refers the dominant frequency of the water surface waves for the cases with the roughness array on the test plate. Seen from Table 1, the discrepancies between the dominant frequencies of the driven surface waves on the flat plate and the frequencies of surface waves on the flat plate with short roughness was less than 0.1Hz, which indicates that the existence of the roughness array would have almost no effect on the propagation frequencies of the wind-driven surface waves. It should also be noted that, for the same airflow free stream velocity $U_\infty = 10m/s$ and the same water flow rates, the film thickness values of $\overline{h_r}$ were found to be about 30% higher than the corresponding $\bar{h}$ values. It indicates that the propagation frequencies of the wind-driven surface waves seem to be less sensitive to film thickness.

4.3. Time-averaged results and water mass trapped ratio

Figure 4-16 shows the time-averaged film thickness distributions of the wind-driven water film flows over the test plate with the airflow free stream velocity changing from $U_\infty = 10m/s$ to $U_\infty = 20m/s$. The water film flow rate was kept in constant at $q = 25.3ml/min/cm$. As shown in those figures, the time-averaged film thickness distributions of the water film flow over the flat plate were found to be quite smooth for all three wind speeds. As the wind speed increases, the time-averaged film thickness was found to decrease from 0.4mm to 0.05mm.

The time-averaged film thicknesses for the cases of the wind-driven water film flows over the roughness array are given in Fig. 4-17 and Fig. 4-18. Figure 4-17 shows the cases of the film flow over the short roughness array and Figure 4-18 shows the cases of the film flow over the long roughness array. For the same wind speed, the time-averaged film thickness distributions of film flow over both the short and long roughness were similar. A U-shaped film thickness distribution was found in front of the roughness array at relatively low wind speed $U_\infty = 10m/s$ (Fig. 4-17(a)). For the cases with relatively high wind speeds (i.e., the cases of $U_\infty = 15m/s$ and

$U_\infty = 20m/s$), the time-averaged film thickness distributions of the water film flow over the roughness array were found to be smooth surfaces as well. In comparison with those of the cases without the roughness array, the main differences were found to be the trapped water mass at the downstream of the roughness array (Fig. 4-17(b), (c)).

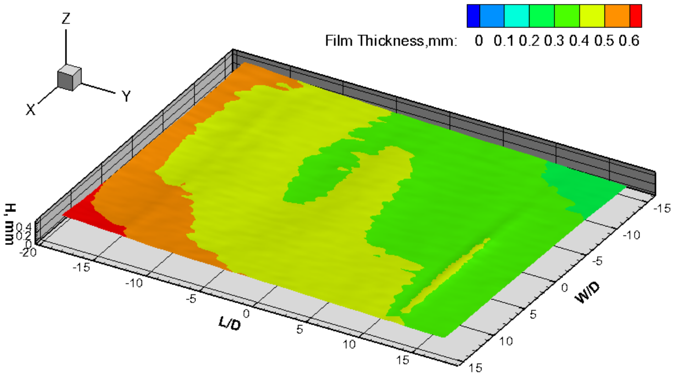

(a) $U_\infty = 10m/s$

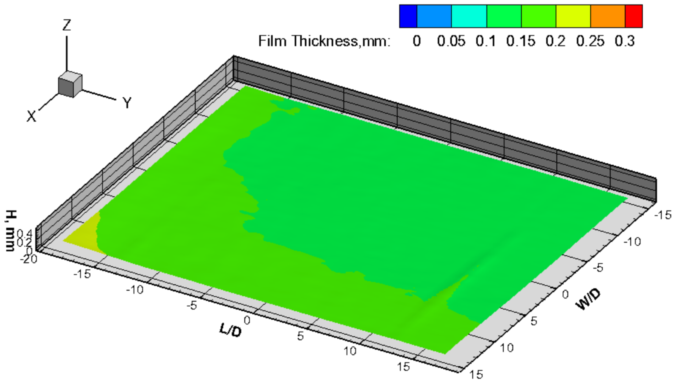

(b) $U_\infty = 15m/s$

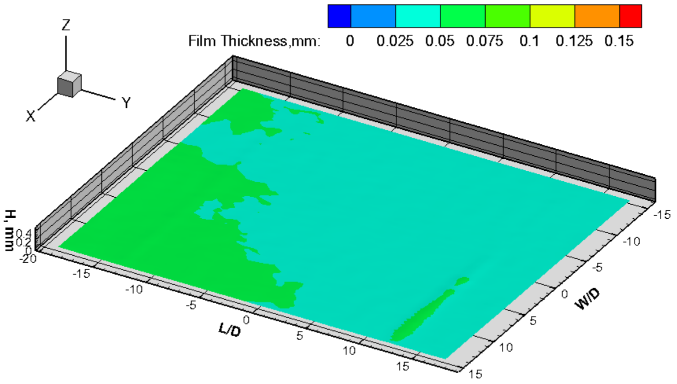

(c) $U_\infty = 20m/s$

Figure 4-16 *Time average film thickness measurement results of the wind-driven water film flow over flat plate at the water flow rate of q=25.3 ml/min/cm*

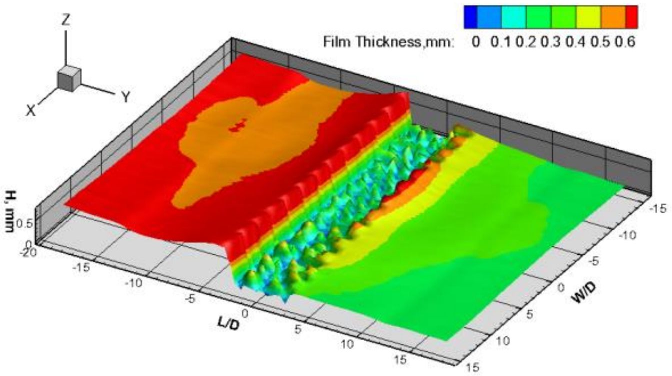

(a) $U_\infty = 10m/s$

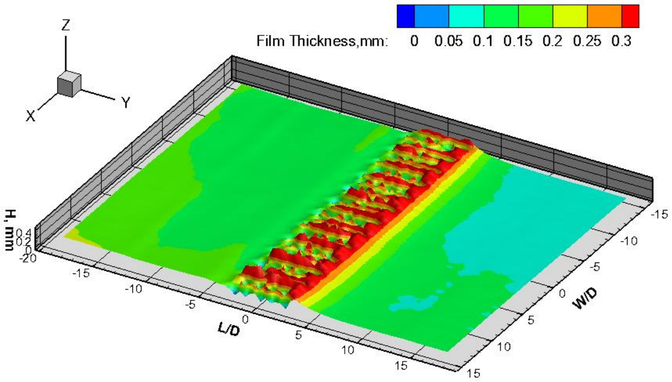

(b) $U_\infty = 15m/s$

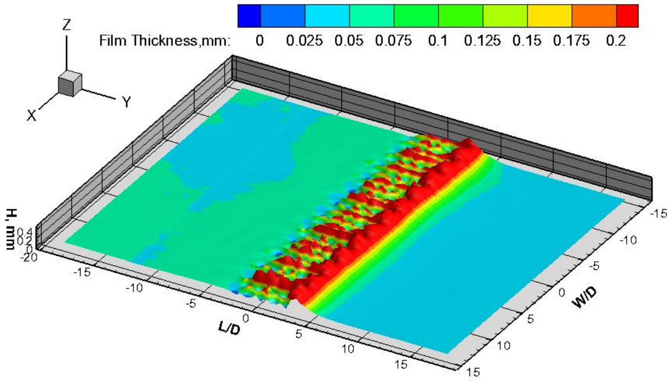

(c) $U_\infty = 20m/s$

Figure 4-17 *Time average film thickness measurement results of the wind-driven water film flow over short roughness at the water flow rate of q=25.3 ml/min/cm*

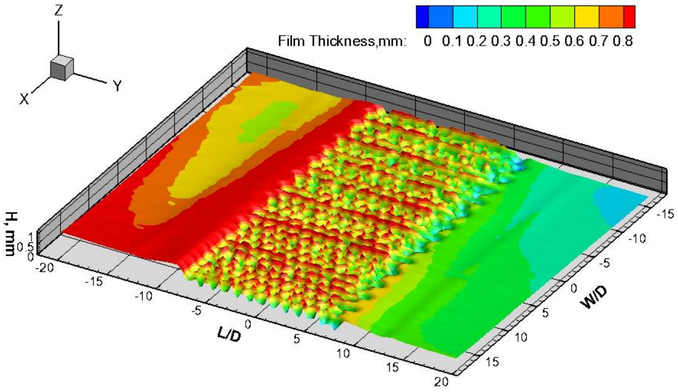

(a) $U_\infty = 10m/s$

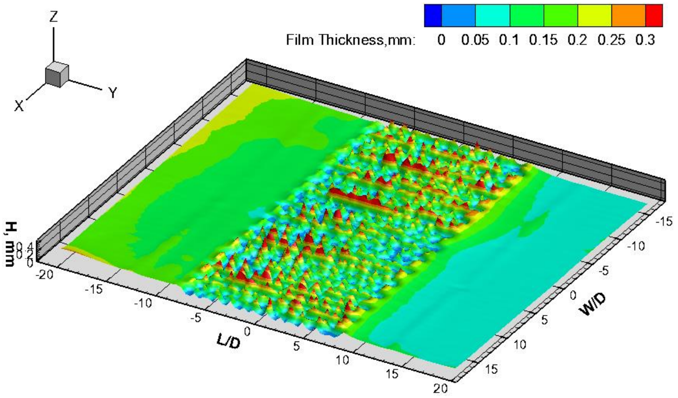

(b) $U_\infty = 15m/s$

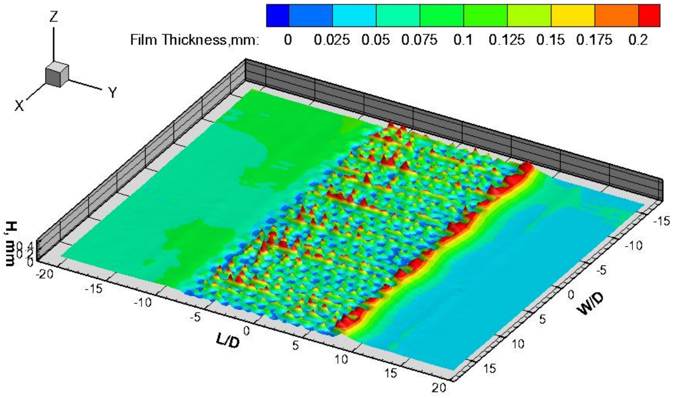

(c) $U_\infty = 20m/s$

Figure 4-18 *Time average film thickness measurement results of the wind-driven water film flow over long roughness at the water flow rate of q=25.3 ml/min/cm*

Figure 4-19 and Figure 4-20 shows the time-averaged film thickness profiles at the centerline of the surface water film flow under different test conditions. Both $\bar{h}$ and $\overline{h_r}$ were found to increase with the increase of water film flow rate; however those two values were found to decrease with the increase of the airflow free stream velocity. As shown in first column of Fig. 4-

19 and Fig. 4-20, for the cases of the water film flow over the flat plate without the roughness array, the time-averaged film thickness was found to decrease almost linearly along the stream wise direction. For the cases of the water film flow over the flat plate with the roughness array, it is observed that the roughness array would raise the film downstream of the roughness array. At the range upstream of the roughness array, the roughness was performed as a barrier to block the film flow at the low free stream velocity but had limited effects when the free speed velocity bigger than 15m/s. The influence range of the roughness array was found to decrease with the increase wind speed. As shown clearly in Fig. 4-19(A) and Fig. 4-20(A), due to the existence of the roughness array, the water film flow thicknesses downstream of the roughness array were raised up until 8D distance away from the roughness. However, for cases of the free stream wind speed increased to $U_\infty = 15m/s$ and $U_\infty = 20m/s$, the roughness array can only influence the downstream flow range 4D distance away from the roughness. The DIP measurement results are in agreement with the PIV measurement result shown in Fig. 4-7.

As suggested by Rothmayer and Hu (2014) , the roughness induced trapped water mass was defined as the total water mass held in place about the roughness. The dimensionless trapped water mass ratio was given as:

$$m_t^* = \frac{m_t}{\rho_{water} L^3} = \iint \frac{h}{L} d\left(\frac{y}{L}\right) d\left(\frac{z}{L}\right) \tag{4.3}$$

Where m_t^* is the dimensionless water trapped mass, L is the characteristic length. As given in Equation (4.3), the trapped water mass ratio would be the ratio of the water mass held in place by the roughness array to the water mass that would be within the region of interest if the test plate is flat. Based on the DIP measurement results, the time-averaged water mass trapped ratio, $\overline{\langle M_T \rangle}$, can be calculated by using the following equation:

$$\overline{\langle M_T \rangle}\Big|_i = \frac{\sum_j \bar{h}_{r(i,j)}}{\sum_j \bar{h}_{(i,j)}} \tag{4.4}$$

Where $\overline{h_r}$ is the time-averaged film thickness of the water film flow over the roughness array, $\bar{h}$ is the time-average film thickness of the water film flow over the flat plate without the roughness array, subscript i is the index of the measurement points along stream wise direction, j is the index of the measurement point along the span wise direction. As shown in Fig. 4-19 and Fig. 4-20, for the cases with relatively low wind speed, the water mass would be blocked by the roughness array and the water mass was found to be trapped mainly at the upstream of the roughness array. For the cases of higher wind speeds, the water mass was found to be trapped mainly at the downstream range of the roughness array. For the test cases with the same wind speed, the obtained mass trapped ratio curves were found to have similar distribution pattern, regardless of the water film flow rate. For film flow over short roughness cases, as the airflow free stream velocity increase from $U_\infty = 15m/s$ to $U_\infty = 20m/s$, the maximum value of the water mass trapped ratio $\overline{\langle M_T \rangle}$ for the $U_\infty = 20m/s$ case was found to be about four times higher than the of the $U_\infty = 15m/s$ case. The measurement results reveal clearly that, the water mass trapped ratio is very sensitive to the wind speed, but less sensitive to the flow rate of the water film flow over the test plate.

The same trend was obtained from the result of the long roughness trapped ratio plots (Fig. 4-20 (B), (C)). However, the trapped ratio of the film pass the long roughness array was much smaller than the trapped ratio of the film flow over the short roughness array. As the airflow turbulent kinetic energy was much higher for the long roughness cases. A small raise of the film thickness might help the airflow overcome the adverse pressure gradient and prevent flow separation, which decreased the mass trapped effect.

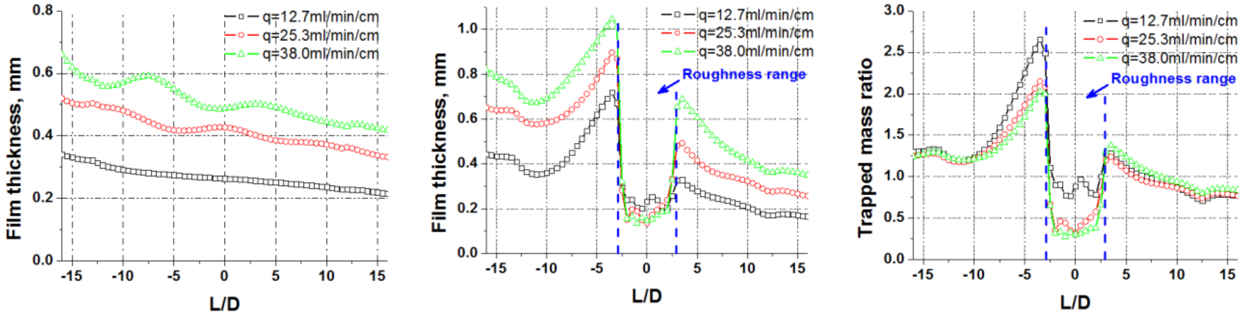

(a) Flat plate (b) Short roughness (c) Mass trapped ratio

A. $U_\infty = 10m/s$

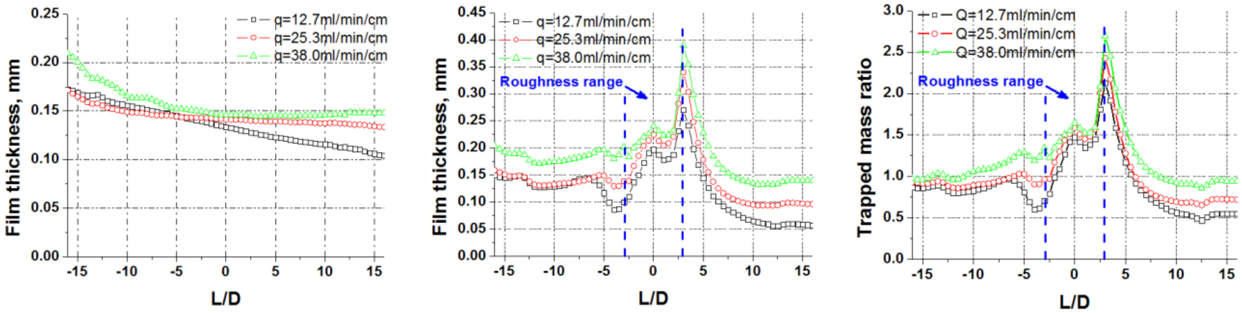

(a) Flat plate (b) Short roughness (c) Mass trapped ratio

B. $U_\infty = 15m/s$

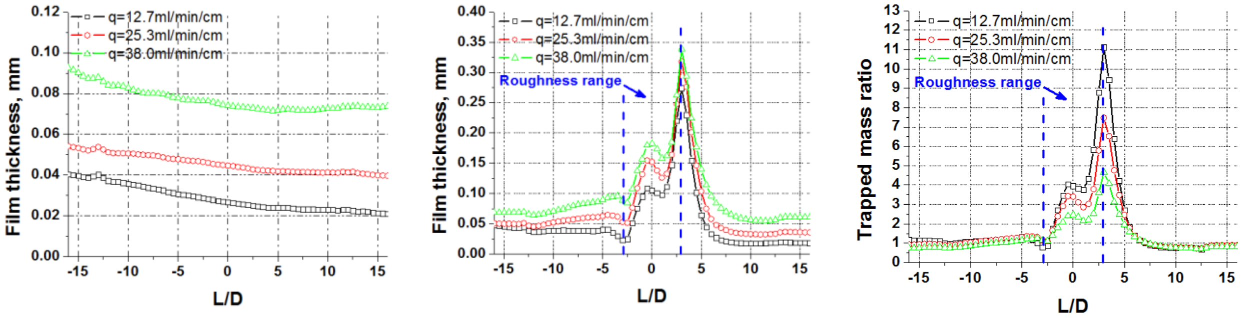

(a) Flat plate (b) Short roughness (c) Mass trapped ratio

C. $U_\infty = 20m/s$

Figure 4-19 *Time-averaged film thickness profiles and the water mass trapped ratio of short roughness array cases*

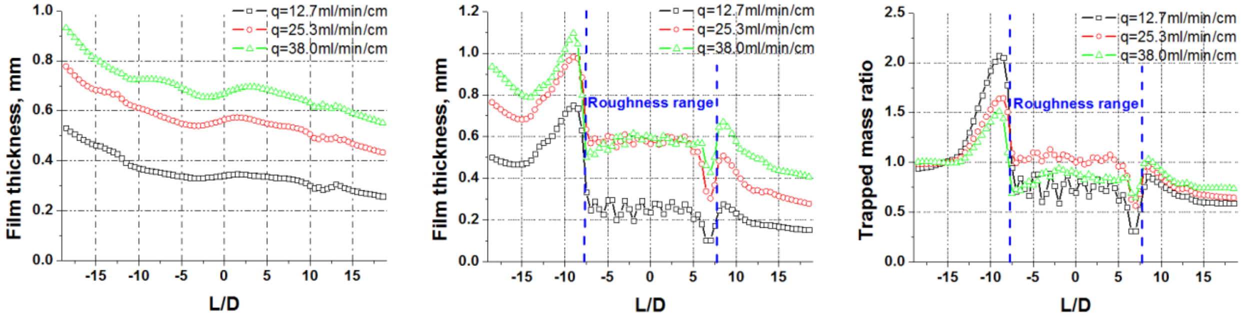

(a) Flat plate (b) Long roughness (c) Mass trapped ratio

A. $U_\infty = 10m/s$

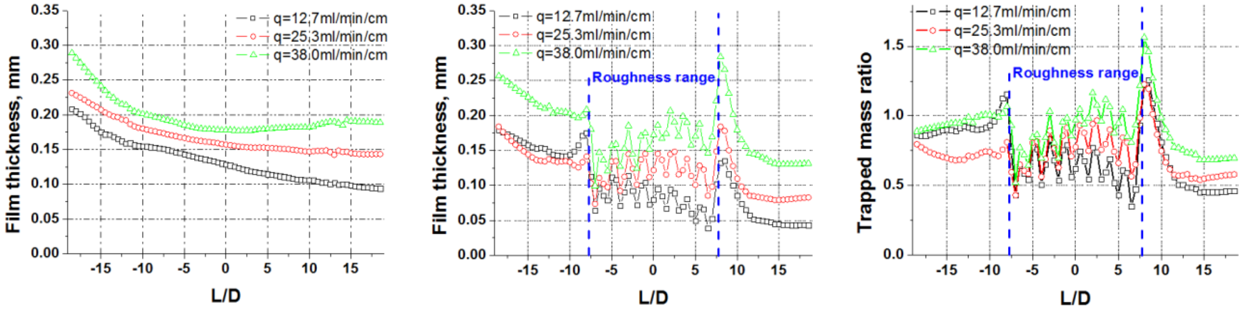

(a) Flat plate (b) Long roughness (c) Mass trapped ratio

B. $U_\infty = 15m/s$

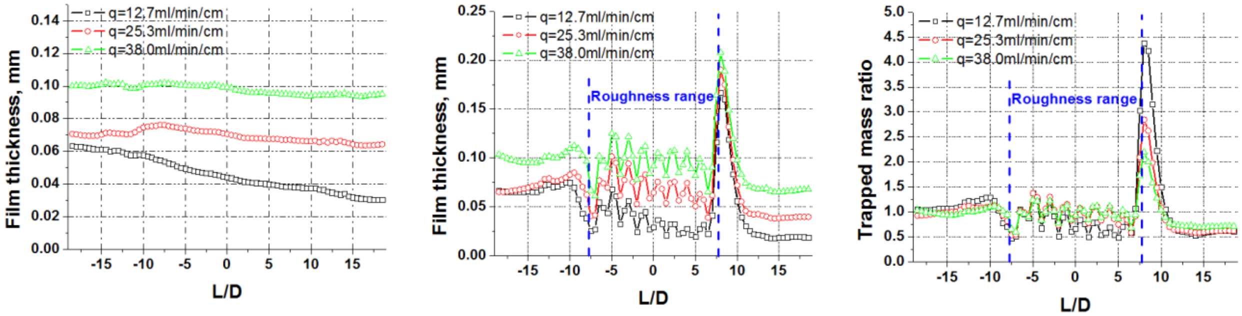

(a) Flat plate (b) Long roughness (c) Mass trapped ratio

C. $U_\infty = 20m/s$

Figure 4-20 *Time-averaged film thickness profiles and the water mass trapped ratio of long roughness array cases*

5. Conclusions

An experimental study was conducted to study the transient behavior of the wind-driven water film flows over a roughness surface. A novel digital image projection (DIP) system was used to achieve time-resolved measurements of the film thickness distributions of the surface water film flows over a flat plate and roughness arrays. The water mass trapped effect induced by the roughness array was evaluated in details. The conclusions derived from the present experimental study can be summarized as follows:

- PIV measurements were performed to characterize the boundary layer flow of the current study. The boundary layer over a flat plate with roughness and film flow was a laminar flow boundary layer. The water film flow could induce a laminar to turbulent boundary layer transition. This transition process occurred randomly. Airflow would separate behind the roughness array. Boundary layer flow transition could be initiated by the combined effect of film flow and roughness as well. Compared with the short roughness array case, the boundary layer profiles after the airflow passed the long roughness array were closer to a fully developed turbulent boundary.

- For the case with relatively low wind speed at $U_\infty = 10m/s$, long wavelength, regular 2D surface waves occurred on the wind-driven film flow. For the case with higher wind speed $U_\infty = 15m/s$ and $U_\infty = 20m/s$, irregular, sharp-crested surface waves were found to appear. The dominant frequencies of the surface waves were found to be more sensitive to the free stream velocity. The presence of the roughness array seems to have almost no effects on the frequencies of the surface waves.

- The trapped effect of the roughness array on the water film flows exhibits two different behaviors. For the case with relatively low wind speed at $U_\infty = 10m/s$, the trapped effect was found to be mainly in front of the roughness array, i.e., the roughness array was found to perform as a dam to the incoming surface water film flow. For the cases with higher wind speed at $U_\infty = 15m/s$ and $U_\infty = 20m/s$, the water mass trapped effect was located mainly at the back side of the roughness array. The water mass trapped effect was found to be very sensitive to the wind speed, but less sensitive to the flow rate of the water film flow over the test plate. Longer roughness array will decrease the mass trapped effect.

References

Anderson DN, Ruff GA (1998) Measurement and correlation of ice accretion roughness 36th AIAA Aerospace science meeting and exhibit. Reno, NV

Cobelli PJ, Maurel A, Pagneux V, Petitjeans P (2009) Global measurement of water waves by Fourier transform profilometry. Experiments in Fluids 46:1037-1047

Gent RW, Dart NP, Cansdale JT (2000) Aircraft icing. Philosophical Transactions of the Royal Society of London Series A: Mathematical, Physical and Engineering Sciences 358:2873-2911

Matheis BD, Rothmayer A (2003) Impact of underlying surface roughness on water transport AIAA 41st Aerospace sciences meeting and exhibit. Reno, NV,

Olsen W, Walker E (1987) Experimental evidence for modifying the current physical model for ice accretion on aircraft surfaces. NASA TM-87184

Rothmayer AP, Hu H (2013) Linearized solutions of three-dimensional condensed layer films. 5th AIAA Atmospheric and Space Environments Conference. San Diego, CA

Rothmayer AP, Hu H (2014) On the numerical solution of three-dimensional condensed layer films. 6th AIAA Atmospheric and space environments conference. Atlanta, GA

Schlichting H, Gersten K (2000) Boundary-layer theory. Springer Science & Business Media, pp

Shin J (1996) Characteristics of surface roughness associated with leading-edge ice accretion. Journal of aircraft 33:316-321

Wang G, Rothmayer A (2009) Thin water films driven by air shear stress through roughness. Computers & Fluids 38:235-246

Zhang K, Zhang S, Rothmayer A, Hu H (2013) Development of a digital image projection technique to measure wind-driven water film flows. 51th AIAA Aerospace sciences meeting and exhibit. Grapevine, Texas

CHAPTER 5

AN EXPERIMENTAL STUDY ON WIND-DRIVEN WATER RIVULET/FILM FLOWS OVER AN AIRFOIL PERTINENT TO AIRCRAFT ICING PHENOMENA

Abstract: Aircraft icing is a serious threat to aviation safety. Icing accretion process usually interacts with surface water run back flow under glaze icing condition. Advancing the technology for safe and efficient aircraft operation in icing conditions requires a better understanding of the underlying physics of complicated thermal flow phenomena pertinent to aircraft icing phenomena, both for the icing itself as well as for the water runback along contaminated surfaces of wing surface. In the present study, an experimental investigation was conducted to characterize the surface wind-driven water film/rivulet flows over a NACA 0012 airfoil in order to elucidate the underlying physics of the transient surface water transport behavior pertinent to aircraft icing phenomena. The experimental study was conducted in an icing research wind tunnel available at Aerospace Engineering Department of Iowa State University. A novel digital image projection (DIP) measurement system was developed and applied to achieve quantitative measurements of the thickness distributions of the surface water film/rivulet flow at different test conditions. The measurement results reveal clearly that, after impinged on the leading edge of the NACA0012 airfoil, the micro-sized water droplets would coalesce to form a thin water film in the region near the leading edge of the airfoil. The formation of rivulets was found to be a time-dependent process and relies on the initial water runback flow structure. The width and the spacing of the water rivulets were found to decrease monotonically with the increasing wind speed. The film thickness icing scaling law is evaluated by the time-average measurement film thickness. The measurement results show good consistency with the analytical scaling predictions.

1. Introduction

Aircraft icing is due to the supercooled water droplets impinging and subsequent icing in the surface of the airplane. There are two types of icing accretion processes: glaze icing and rime icing. In a dry regime, all the water collected in the impingement area freezes on impact to form rime ice. For a wet regime, only a fraction of the collected water freezes in the impingement area to form glaze ice and the remaining water runs back and can freeze outside the impingement area. Because of its wet nature, glaze ice is the most dangerous type of ice. It causes airplane performance degradation (Bragg et al. 1986) and inhibits the control of airplane (Ranaudo et al. 1991). Water beads, rivulets and film flows run back along the airfoil surface during glaze icing condition (Olsen and Walker 1987). The behaviors of surface water run back flows will redistribute the impinging water mass and disturb the local flow filed, as a result, influence the icing accretion process and aerodynamic characteristics of the aircraft. In this work, an experimental investigation was conducted to quantify important micro-physical processes of water runback on an airfoil surface which are pertinent to aircraft icing.

Wind-driven water thin films over airfoil surfaces and flat plates have been studied both theoretically and experimentally. Theoretical study on water film over an flat plate by Nelson (1995) provided steady smooth film thickness solution which increases along stream direction. Feo (2001) and Rothmayer (2003) suggested a scaling law that relates steady film thickness with Reynolds number and Liquid Water Content (LWC). The wave generation of wind-driven liquid films over flat plate had been examined for small disturbances (Craik 1966, Miesen and Boersma 1995, Ueno and Farzaneh 2011). Tsao et al (1997) investigated the stability of a thin film over an airfoil surface. In those works, water-air interface becomes unstable and surface waves arise under certain film thickness conditions. Boundary layer theories were developed to describe the more complex interfacial waves on thin liquid films (Rothmayer et al. 2002, Rothmayer and Tsao 2000). The formation of local roughness and water beads were observed during airfoil icing tests (Anderson and Ruff 1998, Olsen and Walker 1987). The incipient motions of water beads and film flows over roughness had been examined by Rothmayer (Rothmayer and Hu 2013, Rothmayer and Tsao 2001, Wang and Rothmayer 2009). The mechanism of initial roughness formation underneath wet surfaces was considered as the instability effect of ice surface (Otta and Rothmayer 2009, Rothmayer and Hu 2012). An spray water airfoil test at NASA Lewis (Glenn) research center revealed that the water runback flow on an airfoil can be divided into fully wetted film flow range and partly wetted rivulets range (Gelder and Lewis 1951). A number of studies have been done to model the formation of rivulets (Al-Khalil et al. 1990, Marshall and Ettema 2004, Thompson and Jang 1996, Thompson and Marrochello 1999).

Previous experimental investigations about surface water flows over aerodynamic shapes generally illustrated the macro water flow phenomena by analyzing videos taken in the experiments (Hansman and Barsotti 1985, Hansman and Craig 1987, Olsen and Walker 1987, Thompson and Jang 1996). The important micro-physical processes such as film thickness distribution, contact line moving velocity and wet surface area can not be well revealed in those experiments. Advanced experimental techniques capable of providing accurate measurements to reveal the micro-transient phenomenon of surface water behavior like film thickness, wavy surface structure, rivulet width, and contact angle and rivulet front speed are highly desired.

In the present study, a digital image projection (DIP) system is developed to achieve non-intrusive thickness measurements of wind-driven water droplet/rivulet flows over a NACA0012 airfoil in order to elucidate the mechanisms of the unsteady surface water transport process pertinent to icing and rain phenomena. The DIP technique is based on the principle of structured light triangulation in a similar manner as a stereo vision system but replacing one of the cameras for stereo imaging with a digital projector. The digital projector projects line patterns of known characteristics onto the test specimen (i.e., a water droplet/rivulet on a test plate for the present study). The pattern of the lines is modulated from the surface of the test object. By comparing the modulated pattern and a reference image, the 3D profile of the test object with respect to the reference plane (i.e., the thickness distribution of the water droplet/rivulet flow) can be retrieved quantitatively and instantaneously. The fundamental principles and more details of the technique including image correlation algorithm, displacement to height calibration procedure, accuracy verification and sample measurements about wind-driven film flow over flat plate were described in Zhang et al., (2013).

In the following sections, section 2 describes the complete experiment set up for measurements of wind-driven thin water rivulet/film flows over a NACA 0012 airfoil surface. Section 3 shows water film/rivulet thickness measurement results. The transient process of developing water runback flow is revealed. Average film thickness is obtained and agrees with theoretical analysis. Section 4 presents conclusion remarks.

2. Experiment setup

Figure 5-1 illustrates the schematic of the experiment setup for the thickness measurement of thin water rivulet/film flows over a NACA 0012 airfoil surface. The experiments were performed in ISU-Goodrich Icing Research Tunnel (IGIRT). The wind tunnel has a plexiglass test section with cross section dimension of 25.4×25.4cm (W×H). Three internal mix air atomization nozzles are installed in the upstream of the tunnel contract section. Pressure regulators were used to control the spray nozzle’s air and water supply incoming pressure. The spray water flow rate was monitored by a flow meter (Omega FLR1010ST-D). The Liquid Water Content (LWC) and droplet Mean Volume Diameter (MVD) can be controlled by adjusting the spray nozzle water pressure and air supply pressure. In order to avoid spray water beads blocking the light paths of camera and projector, only two of the spray nozzles were used to generate a cloud of spray water droplets. The spray air supply pressure and spray water supply pressure for the nozzle are 45 and 20 psi respectively. A small amount of flat white latex paint (1% volume fraction) was added into the spray water for enhancing the diffusive reflection on the liquid surface. A NACA0012 airfoil model with chord length c=101mm was installed in the center of the test section. The model was 3D printed by a rapid prototyping machine. To improve the diffuse reflectivity of the model surface, the test model was coated with flat white paint. The painted surface of the test model was carefully sanded. In present study, all experiments were conducted with zero angle of attack (AOA=0º) at room temperature. Five different wind speeds 10m/s, 15m/s, 20m/s, 25m/s and 30m/s ($Re = 0.67 \times 10^5 - 2.02 \times 10^5$) were employed.

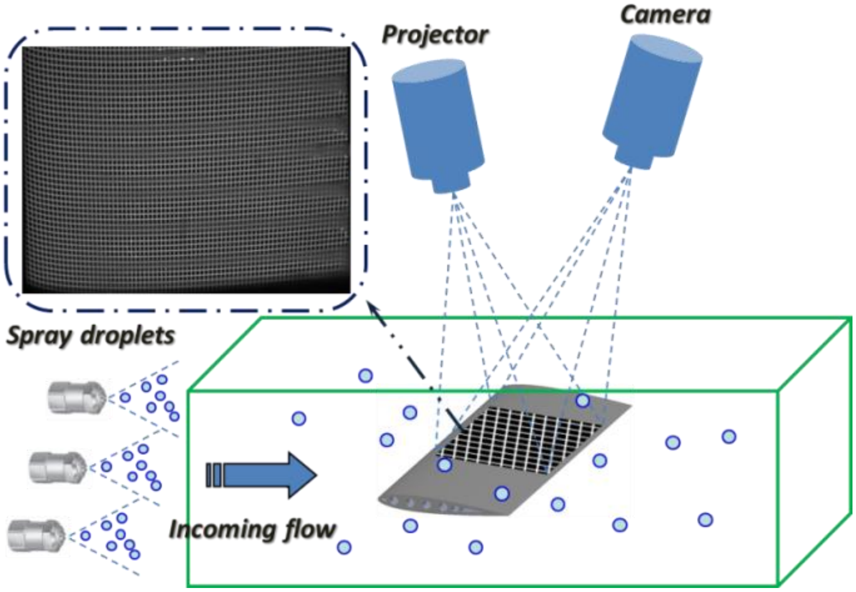

Figure 5-1 *Experimental setup used in the present study*

The DIP system set up is generally the same as our previous experiments (Zhang et al 2013). Dell DLP projector (M109S) was used to project cross line grid to the upper surface of the airfoil model. A CCD camera (DMKBU2104) with a Pentax C1614-M lens (F/1.4, f=16mm) were used for image acquisition. The CCD camera and the projector were synchronized by a digital delay generator. Camera speed was set to 30FPS with an exposure time of 2ms. For each measurement, 1200 images (60S) were recorded after the spray nozzle was active. The field of view of the CCD camera is approximately 11cm×8cm. The projected grid size on the captured image is 7×7 pixels (1.1×1.1mm), which is also the interrogation window size for the cross-correlation calculation. The relative location of camera and projector was aligned along the span wise direction to suppress the mirror reflection of the film/rivulet surface and avoid fake cross-line displacement due to the curvature surface of the model. Figure 5-2 shows the typical reference and deformed displacement images. The pictures of the projected cross grid pattern on the airfoil model surface were used as reference images, as shown in Fig. 5-2(a). Compared with a flat plate substrate, the grid crosses were pre-bended. Figure 5-2(b) shows the typical displacement vector field due to presence of film/rivulet flows. Those vectors were converted to actual film/rivulet thickness using the displacement-to-height parameter map that was obtained in the calibration process.

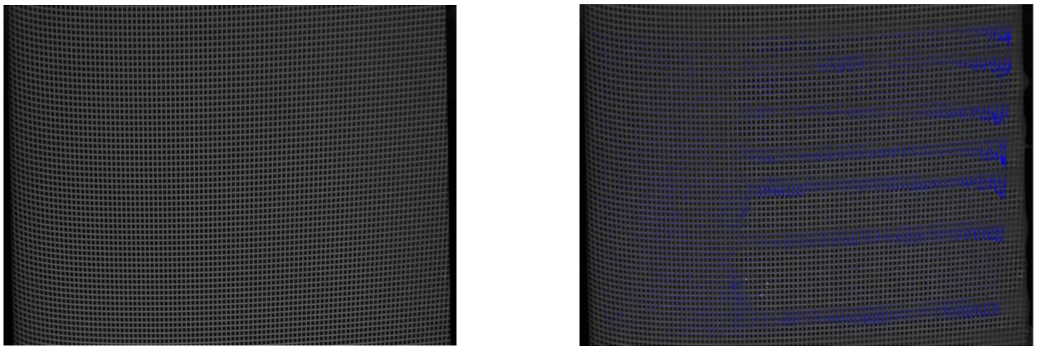

(a). Reference image (b). Deformed image with water rivulets

Figure 5-2 *Typical acquired DIP images*

3. Result and Discussion

3.1. Initial developing process of water runback flow over an airfoil surface

Figure 5-3 - 5-5 shows the time history results of thickness measurements of thin film and rivulet flows under wind speed from U_∞=10m/s to U_∞=20m/s. Seen from Fig. 5-3 to Fig. 5-5, DIP measurement system successfully characterized the whole process of water surface flows. The global structure of rivulet flows were well reconstructed, especially the irregular saw tooth like shape. Rivulets' fronts, rivulets' width, interfacial waves on the rivulets surface were clearly indicated. The results demonstrate the robustness and feasibility of DIP measurement system. The uniform film flow thickness near the leading edge region was well detected as well. However, the accuracy of the measurement needs to be verified because the film thickness close to the stagnation line is the same level as the typical background measurement error (0.1 pixel displacement in the raw picture or 20 micrometer). Note that these measurements were conducted with a camera field of view that covered the whole airfoil surface. Better measurement accuracy might be achieved by refined level of measurement window that focuses on the nose region of the airfoil. In the following section, the process of airfoil water run back flow, the mechanism of formation of rivulet flow and scaling laws pertinent to leading edge film thickness will be discussed in details.

Figure 5-3 to Figure 5-5 illuminate the water runback flow procedure under different free stream wind speeds. As displayed in Fig. 5-3, under low wind speed condition (i.e., U_∞=10m/s), several tiny rivulets were generated near the airfoil leading edge at the initial spray stage (Fig. 5-3(a)). Then the impinging droplets wetted the whole airfoil surface and formed a uniform water film within the direct impinging range. At the same time, those tiny rivulet fronts merged with each other as they flowed downstream. A uniform film flow front that showed a hump shape was detected (Fig. 5-3(b)). As the film flowed further downstream, surface waves appeared and the film front became unsteady and displayed saw tooth shape. At a certain point the film fronts edge broke into rivulets (Fig. 5-3(c)). As rivulets flowed back to the tail of the airfoil, the wetted area of the airfoil was stable and did not change any more (Fig. 5-3(d)). For higher wind speed cases (i.e., U_∞ =20m/s), tiny rivulets appeared and merged with each other at the initial spray stage (Fig. 5-5(a), and Fig. 5-5(b)). However spray water tended to flow into the rivulet paths. No hump shape film front was generated. Finally, the runback flow exhibited uniform film flow at the front of the airfoil surface and rivulets flowed beyond the film flow range (Fig. 5-5(d)). The water runback flow behavior under wind speed U_∞ =15m/s could be considered as an internal process between U_∞ =10m/s and U_∞ =20m/s. The film flow front was more irregular with small breakout shapes which displayed rivulet feature (Fig. 5-4(b)). The runback flow behavior was very similar for the cases of wind speed U_∞>20m/s. The flow phenomena of U_∞=25m/s and U_∞ =30m/s could be represented by the flow phenomena of U_∞=20m/s.

The surface water behaviors are controlled by surface tension, aerodynamic shear stress and pressure force. Notice that tiny rivulets appeared near the airfoil leading edge for all of the wind speeds. This phenomenon is consistent with Olsen and Walker’s observations of above freezing temperature condition experiments (Olsen and Walker, 1987). According to Olsen and Walker’s experiments, the impinging water will first form water beads. When the water beads grows large enough, the aerodynamic force overcome the surface tension force and water beads flow downstream along airfoil surface. Ueno and Farzaneh demonstrated the vertical and horizontal air shear stress force is negligible compared with surface tension under wind speed U_∞ = 5m/s (Ueno and Farzaneh, 2011). Near the stagnation line, the local wind speed is very small. As a result, even free stream wind speed is large, static water beads still form near the stagnation line and generate tiny rivulets after they grow large enough. Those tiny rivulets/beads and their subsequent icing might cause the local ice thickness to increase. Otta and Rothmayer confirmed that a local increase in ice height leads to more cooling from the airflow and cause rapid ice accretion at that point (Otta and Rothmayer, 2009). So the tiny rivulets could be the start point of icing instability.

Franc et al., (1999) presented the collection efficiency experiment results of a 2D NACA 0012 airfoil with 0.9144m of chord. The experiment was performed with a free stream velocity 44.4m/s, angle of attack 0º and spray droplets MVD=20µm. The results show the collection efficiency β of the airfoil surface with wrap distance S>2%c was smaller than 0.1. Similar numerical simulation result were presented by Da-Silveira et al. (2003). Papadakis et al., (1994) gave experimental collection efficiency coefficients of a swept wing with the NACA 0012 airfoil cross section. Papadakis et al. found that the area of collection efficiency β>0.25 was about within wrap distance S<3%c. The relative higher collection efficiency range was very narrow with impinging limit less than 20% of chord length. Based on the previous experiments, we assume that the direct impinging range of the model used in current study is small (<5%c).

According to our observation, the thicknesses of the initial rivulets decreased after they flowed in to low collection efficiency range. The skin friction significantly decreases along the chord length as well (suppose no turbulence transition at the initial spray stage). Under low wind speed condition, those rivulets stagnated at a certain location x_s on the upper surface of the airfoil (around 10% chord length). Meanwhile, the tiny rivulets continuously generated and flowed to the stagnation line. By this way, water accumulated near the stagnation line and formed hump shape film front (Fig. 5-3(b) and Fig. 5-4(b)). The sum of local pressure difference and aerodynamic shear stress exceeded the local surface tension restriction and hump film front flowed back along the stream direction. As can be seen from Fig. 5-4(b), the film front was more instable for higher aerodynamic force. On the other hand, under higher free stream velocity conditions, initial tiny rivulets slowed down and merged with coming rivulets (Fig. 5-5(a) and Fig 5-5(b)). After the rivulets grew large enough, they accelerated again and the oncoming impinging water flowed into the rivulets path. There was no uniform film front generated. The rivulet width might depend on the acceleration rivulet thickness.

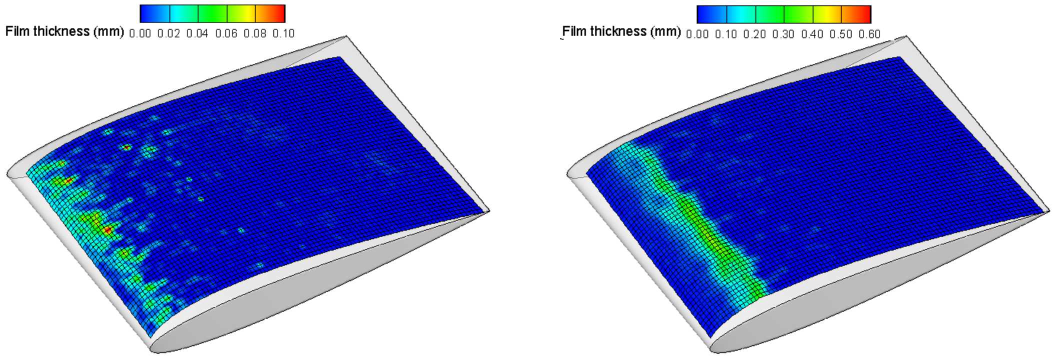

a). t=1s b). t=5s

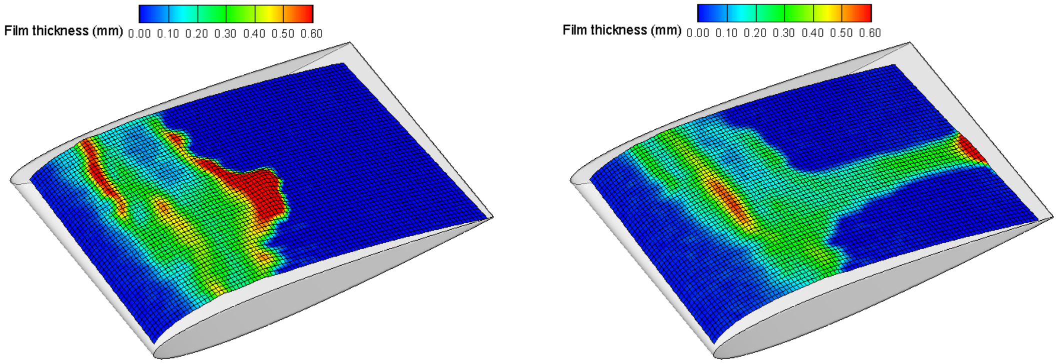

c). t=15s d). t=20s

Figure 5-3 *DIP measurement results of wind speed* U_{∞}*=10m/s.*

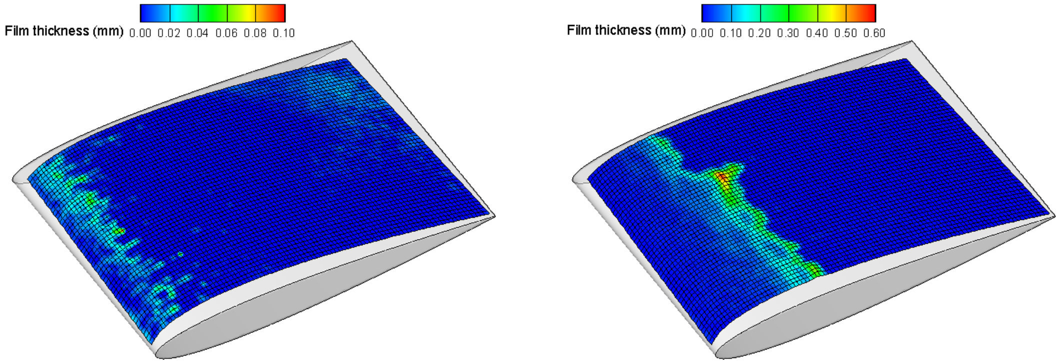

a). t=0.5s b). t=3.0s

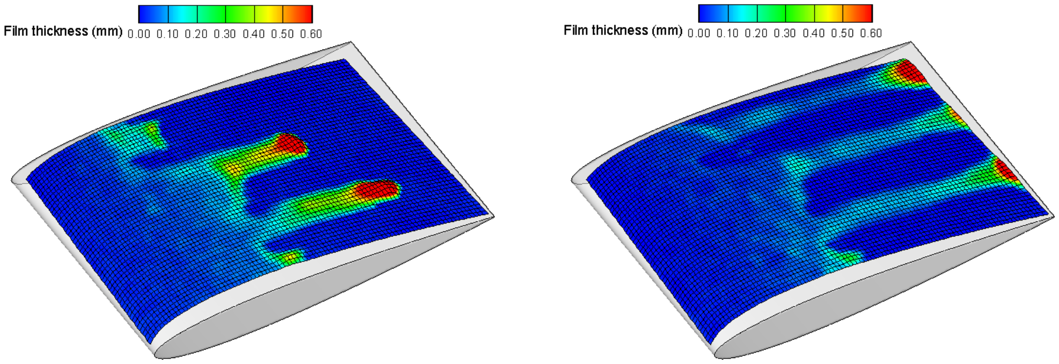

c). t=6.0s d). t=12.0s

Figure 5-4 *DIP measurement results of wind speed* U_∞*=15m/s.*

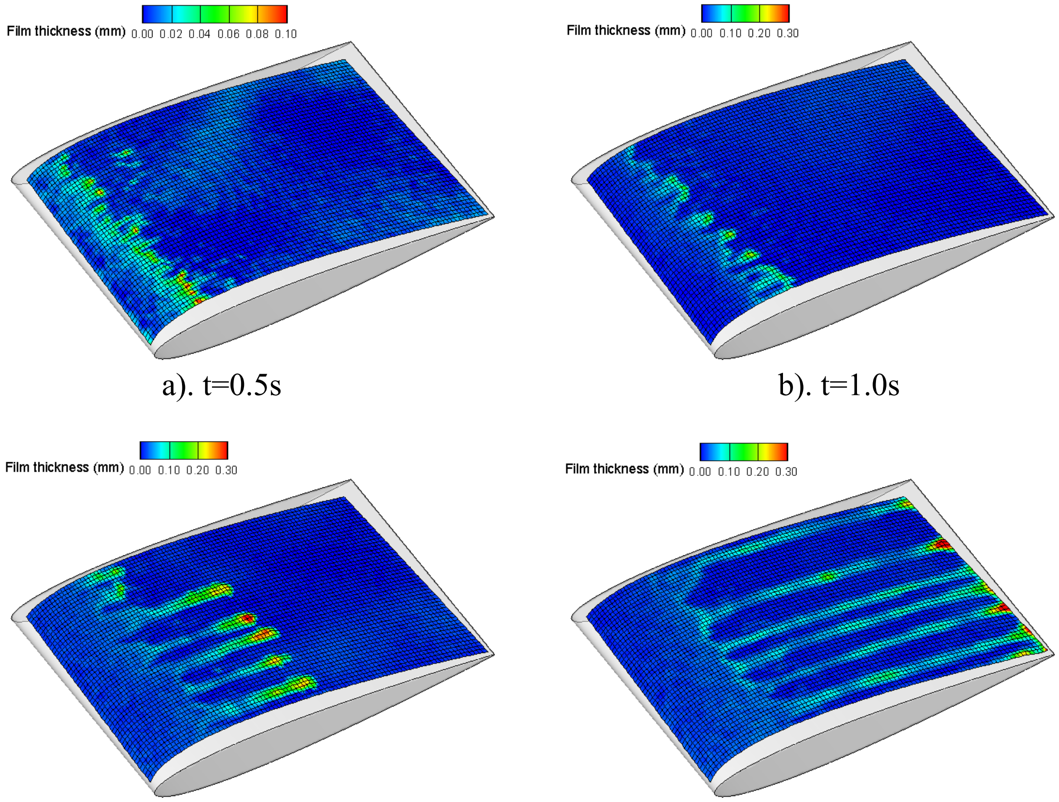

a). t=0.5s b). t=1.0s

c). t=2.0s d). t=6.0s

Figure 5-5 *DIP measurement results of wind speed* U_∞*=20m/s.*

3.2. Evaluation of rivulet formation models on airfoil surface

Thompson and Jang (1996) and Tompson and Marrochello (1999) introduced a rivulet formation model which stated that the rivulets will be formed where the air shear stress surpasses the restraining force due to surface tension. According to Thompson's paper, rivulet formation occurs at the location where

$$0.5C_{f,c}\rho_{air}U_{\infty}^{2}=\sigma\left(1-cos\theta\right) \qquad (5.1)$$

$C_{f,c}$ is the local skin friction coefficient, σ is the liquid surface tension, θ is the liquid-solid contact angle. Thompson's model is based on the steady state theoretical analysis of rivulet formation. As discussed in the above paragraphs, the rivulet formation on the airfoil surface was a time-dependent process. For wind speed U_{∞}=10m/s and U_{∞}=15m/s, before the hump film front broke into rivulets, the hump front was getting thicker and surface waves occurred due to the block of film front. Figure 5-6 shows the film front break point at wind speed 10m/s and 15m/s. The left column of Fig. 5-6 shows the film/rivulet thickness distribution at the film flow break point. The right column of Fig. 5-6 displays the film thickness profile along the streamwise direction at the breaking point. Figure 5-6 revealed that rivulet formation was highly influenced by water surface waves under low wind speed condition. The wave crest thickness approached 0.9mm which is 15% of maximum airfoil thickness. As a result the air pressure at the backside of the water wave was considerably strong. The sum of the pressure force and shear stress surpassed the surface tension restraining force and caused the rivulet front flow downstream. For higher wind speed conditions, rivulet fronts formed shortly after the beginning of impinging. The liquid contact line between the rivulets still moved downstream after the rivulets front formed. The final steady water contact line between rivulets displayed a wedge shape. The vector direction of the sum of surface pressure force, shear stress and surface tension must be along the wedge shape contact line edge as well. Instead of steady 2D analysis, 3D theory is needed to determine the stable water contact line and forecast rivulet configuration.

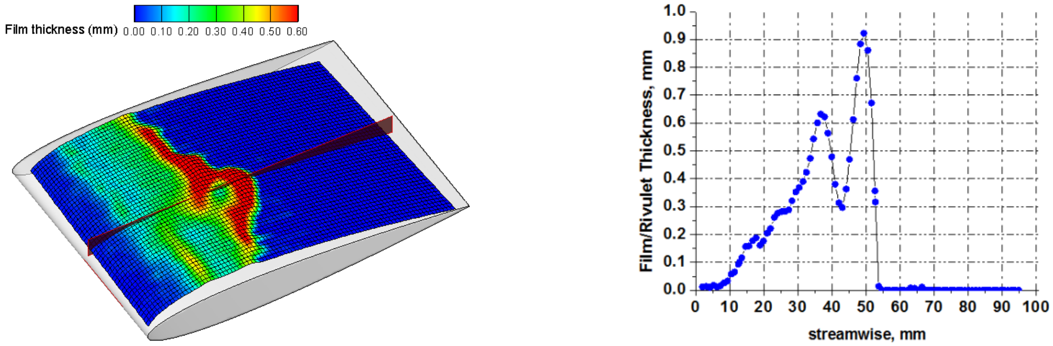

(a). $U_{\infty} = 10m/s$, film front break point (b). Film/rivulet thickness (red plane)

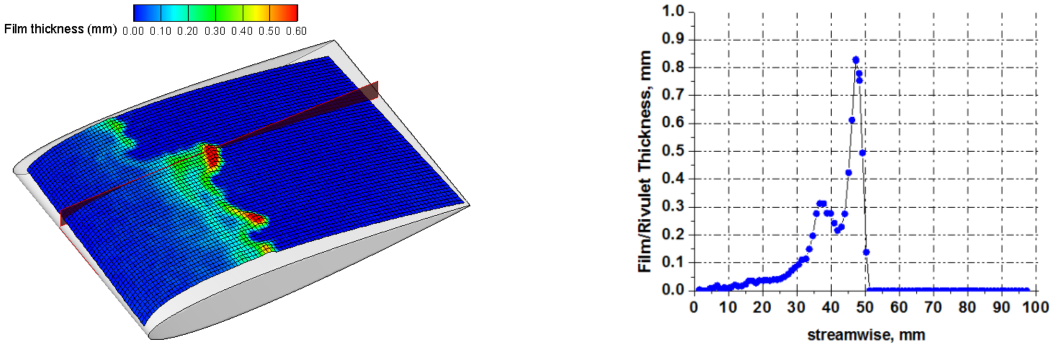

(c). $U_{\infty} = 15m/s$, film front break point (d). Film/rivulet thickness (red plane)

Figure 5-6 *DIP measurement result at film front break point*

Al-Khalil presented a rivulet model base on three criterions: mass flow rate of film and rivulet is equal, energy of film flow and rivulet is equal, rivulet energy is minimum at the steady rivulets configuration (Al-Khalil et al., 1990). The three criterions are modeled by the following equations in Al-Khalil's paper:

$$Q_f = Q_r \tag{5.2}$$

$$E_f = E_r \tag{5.3}$$

$$\frac{\partial}{\partial F}\left[\frac{E_r}{\lambda}\right] = 0 \tag{5.4}$$

Where F is the wetness factor and λ is the ratio of rivulet width to wetness factor. Wetness factor F is defined as the fraction of the surface that is wetted by runback flow at a particular downstream location. By applying those three criterions, Khalil introduced a critical dimensionless film thickness $h^{+} = h_o^3/[6\mu^2\sigma/\rho\tau^2]$, where h_o is dimensional local film thickness, τ is shear stress, and h^{+} is the minimum dimensionless thickness of an unbroken, stable film. Al-Khalis's model considers the film thickness near the leading edge of an airfoil is thinner than the critical film thickness. Within the impinging limit, spray water force to wet the whole surface of airfoil. Rivulet immediately forms right behind the impinging limit. However, seen from Fig. 5-6(a), the hump film front is the thickest area of the whole film and the film flow region definitely exceeds the impinging limit (< 20%c). For higher wind speed, the formation of initial rivulets influences the stable rivulet configuration. In steady impinging droplets wetting the surface, the film-rivulet connection line moves down stream due to the blowing of air flow. Al-Khalis did not consider the dynamic balance of shear stress, surface pressure and surface tension at the stable contact line. The formation of rivulets is a time-dependent process as well. As a result, the steady state rivulets are not necessary to evolve to the minimum energy status.

3.3. Average surface water distribution and steady state scaling law of water layer on airfoil

Time average rivulet/film thickness distributions are shown in Fig. 5-7. The time-averaged thickness was calculated by 500 measurements after the steady wetted area was formed. It is displayed clearly that, as wind speed increase, film/rivulet thickness, leading edge film length, the spacing between rivulets and rivulets' width all decreased. The leading edge film lengths changed from 40% chord to 20% chord as the free stream velocity changed from 10m/s to 30m/s. To elucidate the tendency of surface water distribution along chordwise direction, average surface water thicknesses at the centerline of rivulets are plotted in the right column of Fig. 5-7. Rivulets near the center of measurement windows are selected to extract the data and the data extraction lines are parallel with chord line. Because of the imperfect thin rivulet boundary and the limitation of measurement spatial resolution, the data extraction line can not stay in the center of the selected rivulet. As a result, the thickness profile of cases U_∞=25m/s and U_∞=30m/s are different with other cases. Shown in Fig. 5-7, the surface water thickness kept increasing along the chord length of the airfoil for all the wind velocities. Because of surface tension effect, a sharp increasing of water thickness was detected near the trailing edge. The leading edge film thickness changed from 150 to 10 µm as the wind speed increase. From wind speed 10m/s to 25m/s, The average rivulets' width at streamwise location x=60mm (60%c) were 18.5mm, 11.2mm, 5.6mm, 3.3mm respectively. It is interesting that the wetted factor (F=50%) was almost the same for wind speed 15m/s, 20m/s and 25m/s. Due to the limitation of measurement spatial resolution (1.1×1.1mm), the average rivulets' width under the condition $U_\infty = 30m/s$ is not accurate , we establish the width is around 2mm.

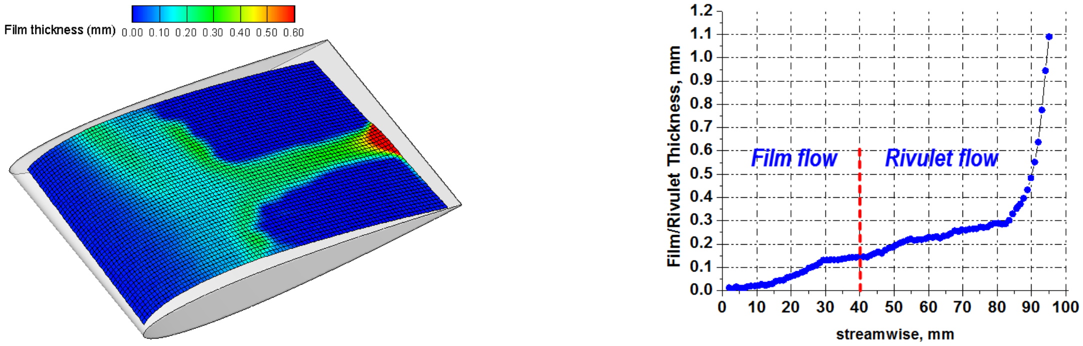

a). Average film thickness b). Film/rivulet thickness profile

(a). Wind speed U_∞=10m/s

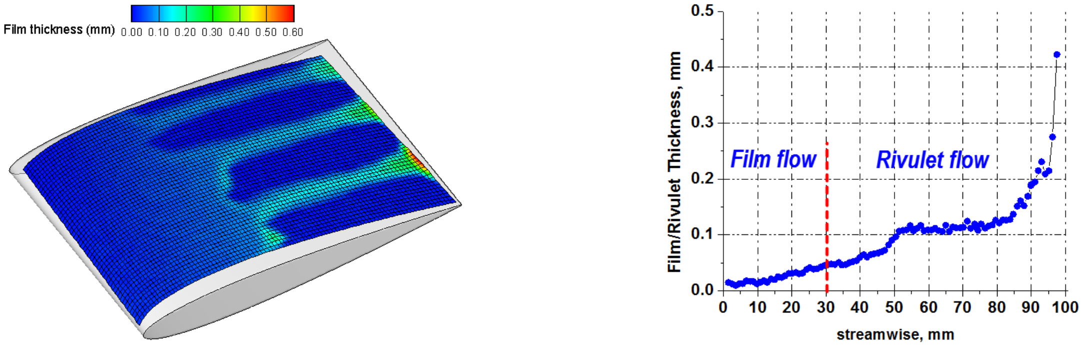

a). Average film thickness b). Film/rivulet thickness profile

(b). Wind speed U_∞=15m/s

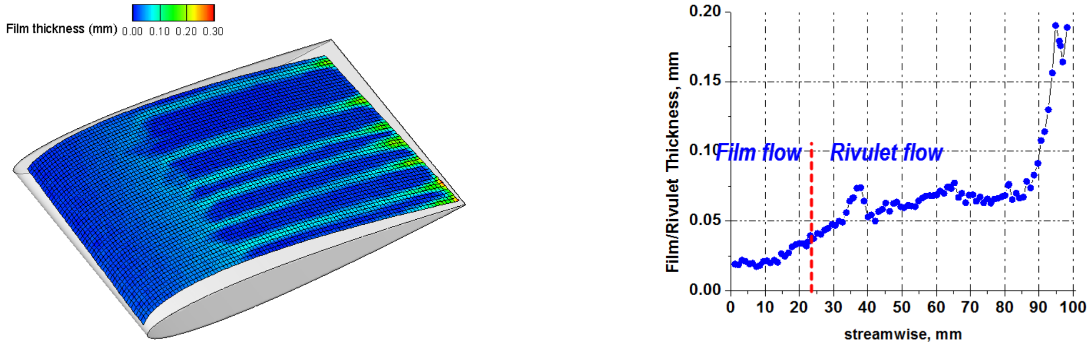

a). Average film thickness b). Film/rivulet thickness profile

(c). Wind speed U_∞=20m/s

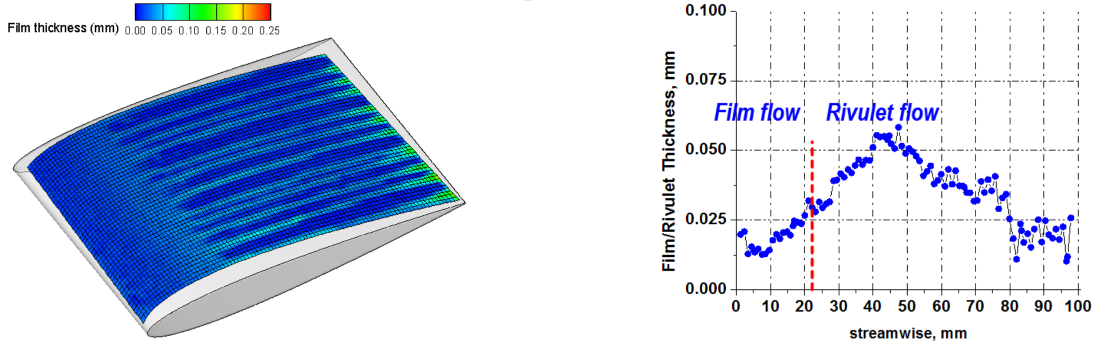

a). Average film thickness b). Film/rivulet thickness profile

(d). Wind speed U_∞=25m/s

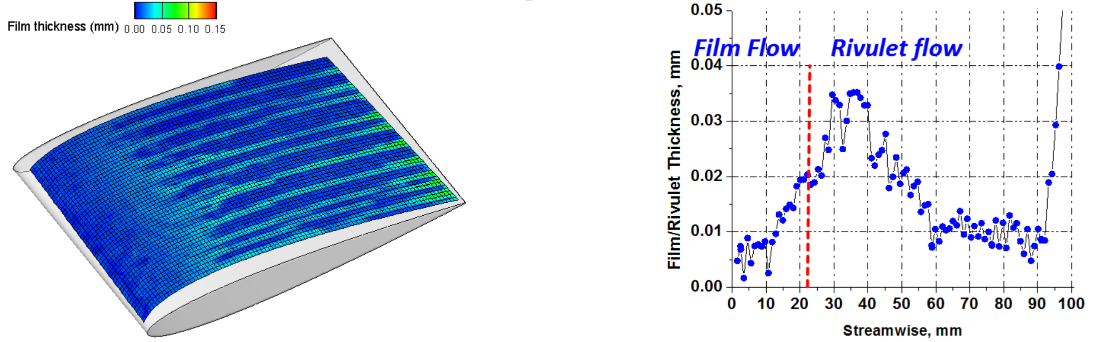

a). Average film thickness b). Film/rivulet thickness profile

(e). Wind speed U_∞=30m/s

Figure 5-7 Time-averaged water film/rivulet thickness result
(Left column: contour plots of time-average film thickness distributions. Right column: film/rivulet thickness profile at the centerline of the rivulets along chordwise direction)

Nelson presented a non-similar boundary layer theory for water film flow in flat plate driven by laminar airflow (Nelson et al., 1995). Nelson assumed the velocity profile within the water film is linear. Using two boundary conditions: (i) Flow rate of film is constant, (ii) Shear stress at the water-air interface is continuous, Nelson derived that film thickness is proportional to $x^{1/4}$, where x denotes the distance away from the flat plate leading edge. Tsao et al. (1997) and Ueno

& Farzaneh (2011) obtained the same scaling law using similar but different methods. In Ueno & Farzaneh's paper (2011), thin water film flow over flat surface was modeled. Water was supplied at the leading edge of flat plate with a constant flow rate. Ueno made the following approximations: (i). airflow and water flow are both laminar flows. (ii). The velocity profile within the water film is linear, in the other word, (i.e., film flow is dominated by viscous effect and the inertia force can be neglected). (iii). The obtained film thickness is steady state value. The influence of the presence of surface waves is ignored. (iv). The only water supply in Farzaeh's simulation was at the leading edge of flat plate, no spray droplet impinging was considered.

Then, Blasius's equation was used to model the undisturbed laminar air flow. For water film, Ueno assumed the following scaling: $\mathrm{h_o} = \mathrm{C_1 x^a}$, $\mathrm{u_{la}} = \mathrm{C_2 x^b}$. Where $\mathrm{u_{la}}$ denotes the water-air interface horizontal velocity. The constants, C_1, C_2, a and b, were determined from the two boundary conditions. First, the volumetric water flow rate per width is constant:

$$Q / l_w = \int_0^{h_o} u_l dy = C_1 C_2 x^{a+b} \int_0^1 u_{l*} dy_* \tag{5.5}$$

Where Q/l_w is the unit width film flow rate, u_{l*}, y_* is normalized interfacial velocity and thickness. Second, the horizontal shear stress at interface is continuous:

$$\frac{C_2}{C_1} \mu_l \frac{du_{l*}}{dy_*} |_{y_*=1} x^{b-a} = \left(\frac{U_\infty^3}{2\upsilon_a} \right)^{1/2} \mu_a \frac{d^2 f_a}{d\eta^2} |_{\eta=0} x^{-1/2} \tag{5.6}$$

Where μ_l, μ_a is the viscosity of water and air, f_a is the normalized stream function, f_a'' is a constant. From equation (5.6), $b - a = -1/2$. Q/l_w is constant along streamwise direction, form Equation (5.5), $a + b = 0$. Consequently, $a = -1/4\,, b = -3/4$. C_1, C_2 are also determined by equation (5.5), (5.6). The relationship between film thickness and film flow rate, wind speed, distance away from leading edge is expressed as:

$$h_o \sim \left(Q / l_w\right)^{1/2} U_\infty^{-3/4} x^{1/4} \tag{5.7}$$

Feo (2001) and Anderson & Feo (2002) measured water film thickness on a stagnation-point probe surface in INTA 2.8×1.7m wind tunnel. The geometry of the stagnation-point probe was a cylindrical shape with diameter d=120mm. A single air-atomizing nozzle was installed in the open test section to generate water spray. However, three type of spray nozzles SUJ 12A, SUJ12, SUJ22B were used. Those nozzles were operated under different water and air pressure to obtain desired LWC and MVD. The tests covered the LWC range 3~14 g/m^3, the MVD range 15-160μm and free stream velocities 20~55 m/s. All of the tests were performed at ambient temperature. The experiment results are plotted in Fig. 5-8. By doing correlation of the measured film thickness, Feo (2001) suggested that the film thickness has a LWC and Reynolds number scaling:

$$h/d \sim LWC^{1/2}\,\mathrm{Re}^{-1/4} \tag{5.8}$$

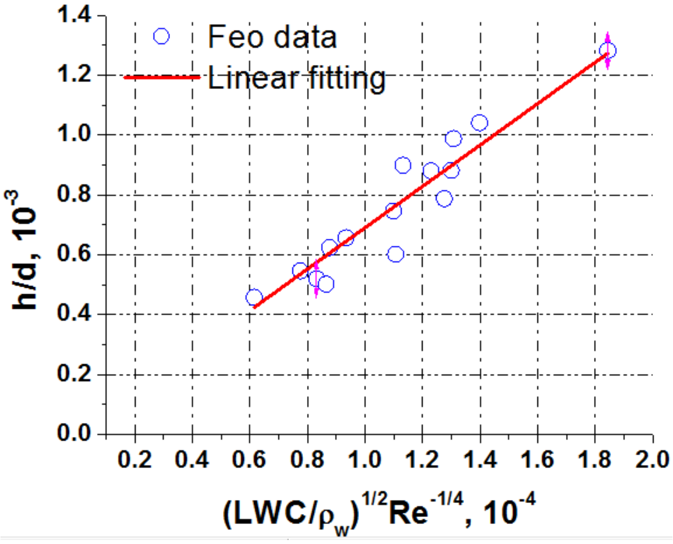

Figure 5-8 *Feo's (2001) film thickness correlation*

This scaling law is verified analytically by Rothmayer (Rothmayer, 2003). Rothmayer assumed that the droplets impact uniformly and continuously on the surface of the stagnation probe. The ultimate equilibrium film thickness was determined from a balance between the water mass that was added to the film due to spray droplets impact and the mass that transported by the film to the side wall of the probe. The rate of mass added to the surface element with streamwise arc length ds is proportional to LWC*ds. The mass flux within the film was modeled as $\rho_l V_l A$. Equating the above two mass flux gives:

$$\rho_l V_l A \sim \text{LWCds} \tag{5.9}$$

Where ρ_l is water density, V_l denotes average streamwise direction velocity within film flow, A is the cross section area of the film flow.

The average streamwise direction velocity within film flow V_l was determined by the shear stress balance in the interface of water and air. For shallow water surface, the streamwise stress balance at air-water interface was given by (Rothmayer and Tsao, 2001):

$$Re^{-1} M \left(\frac{\partial u}{\partial y} \right)_l = Re^{-1} \left(\frac{\partial u}{\partial y} \right)_a \tag{5.10}$$

Where M denotes the water to air viscous ratio which is a constant for current work. Suppose the velocity profile in the film is linear, then $\left(\frac{\partial u}{\partial y}\right)_l = \frac{u_{la}}{h_o}$. Near the bottom of boundary layer, $\left(\frac{\partial u}{\partial y}\right)_a \sim Re^{1/2}$ (Rothmayer and Tsao, 2000). Substitute those two terms into equation (5.10), the average streamwise direction velocity can be expressed as $V_l \sim Re^{1/2} M^{-1} h_o$. Substitute V_l into equation (5.9), the average local film thickness behaves like:

$$h_o / c \sim (LWC)^{(1/2)} Re^{(-1/4)} M^{(1/2)} \tag{5.11}$$

Although equation (5.11) is used to compare with Feo's experimental film thickness on a point-stagnation probe, it is not limited by the model shape. Furthermore, the scaling analysis is also not limited by the range where the impinging water mass rate equals the water mass flux within the film. For film flow over an airfoil surface beyond impinging limit, the water mass flux is coming from the mass flow rate generated by the collected spray droplets within the impinging limit. The ultimate water mass flux balance can be rewrite as:

$$\rho_l V_l A \sim \mathrm{LWC} s_{im} \beta \tag{5.12}$$

Where s_{im} denotes the airfoil arc length within the impinging limit, β denotes the average collection efficiency. s_{im} and β can be considered as constants under specific conditions (i.e. MVD, LWC, free stream velocity, temperature are fixed). By doing the same analysis, equation (5.11) still works for film flow propagation range.

Actually, we find that Ueno's work confirms with Feo's scaling law. Suppose that the LWC distribution is uniform within the whole test section, then the LWC is proportional to Q_s/U_∞, unit width film flow rate Q/l_w should be proportional to Q_s, where Q_s denotes spray water flow rate. Substitute those two relations into equation (5.11), we have

$$h_o / c \sim \left(Q / l_w\right)^{1/2} U_\infty^{-3/4} M^{1/2} \tag{5.13}$$

This formula is generally the same as equation (5.7) except lack the $x^{1/4}$ term. The derivation of the two scaling law are similar, the discrepancy is due to the different expressions for air streamwise shear stress.

For the current work, the spray water flow rate Q_s is fixed. The unit width film flow rate is the same under different wind speed conditions. Figure 5.9 plots the film thickness versus the ¼ power of wrap distance s within film flow range. Wrap distance s is defined as the arc length that starts from the stagnation point. Seen from Fig. 5.9, the leading edge film thickness is 10-100μm. Whereas, the estimated laminar boundary layer thickness based on the chord length of airfoil is 1-2mm. Film thickness is only a small fraction (5%) of the boundary layer thickness. The Couette flow approximation within the film is reasonable. The global profiles in the film flow region exhibit exponent growing trend. However, the film thickness profiles are generally linear curve when the wrap distance $s^{1/4}>1.9$ (s>13mm, x>11.5%). The results are encouraging and show a good agreement with Nelson's theory (The $x^{1/4}$ scaling is first introduced by Nelson). The thickness profile near the airfoil leading edge is not proportional to $x^{1/4}$ due to three reasons: (i) Nelson's theory assume a constant water flow rate near the leading edge, which leads to the theory failing near the leading edge. The film thickness proportional to $x^{1/4}$ must start from certain point downstream. (ii) The leading edge of the NACA 0012 airfoil is a curvature shape. Flat plate analysis result is comparable with airfoil shape when the radian of the airfoil surface is small. (iii) Note that the film thickness at the range s<13mm is less than 15 µm. Cross-correlation generally has sub-pixel accuracy, corresponding to 20 micrometers measurement uncertainty. Additionally, the project light ray may enter into the liquid and cause diffusion effect. Measurement error caused by this diffusion effect is still not clear. The inconsistency between current measurement and Nelson's theory may be caused by the measurement error.

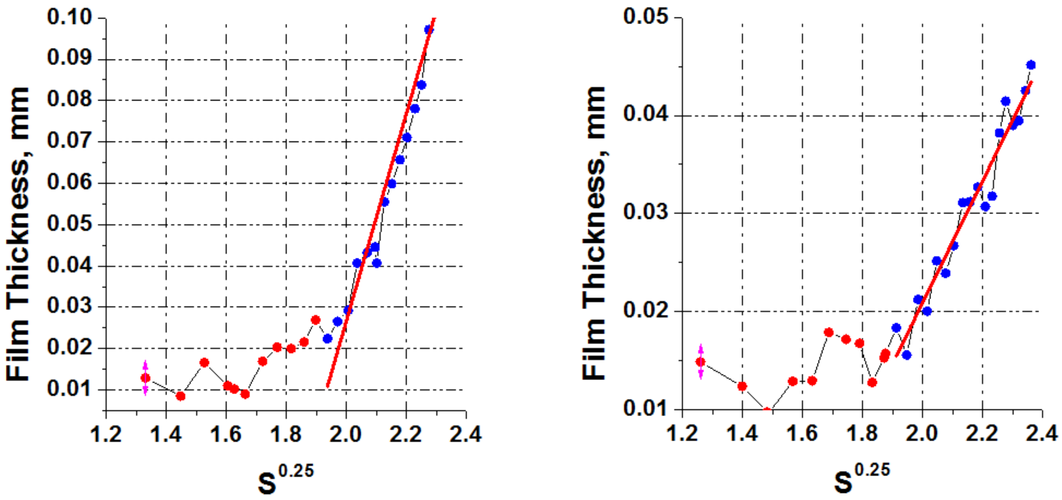

(a). Wind speed U_∞=10m/s

(b). Wind speed U_∞=15m/s

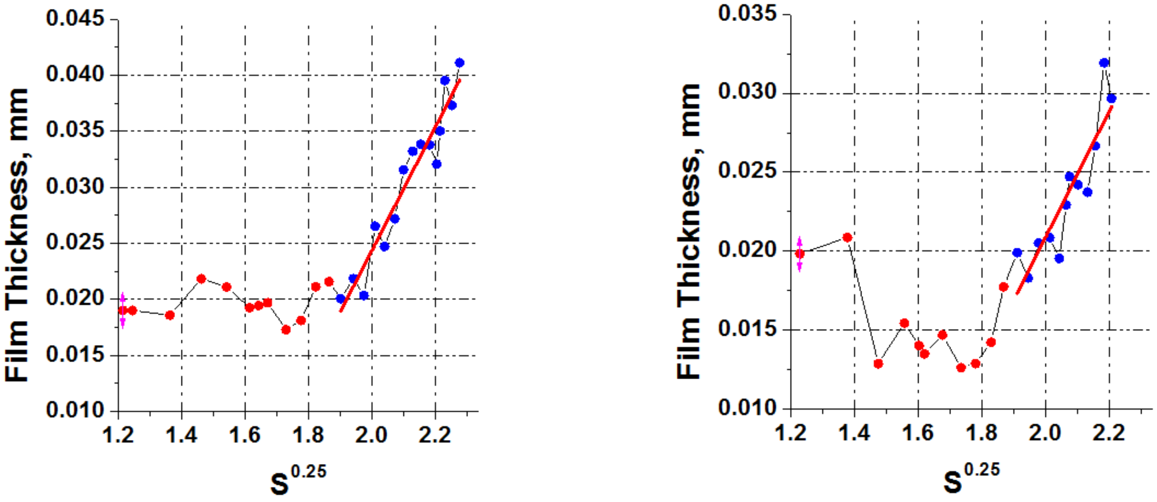

(c). Wind speed U_∞=20m/s (d). Wind speed U_∞=25m/s

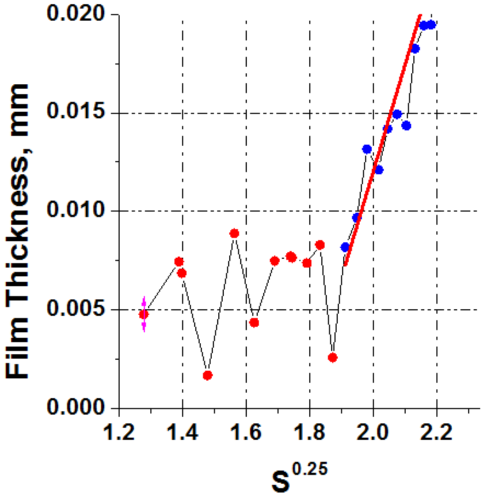

(e). Wind speed U_∞=30m/s

Figure 5-9 *Film thickness vs* $s^{1/4}$ *power scaling*

Film thickness at streamwise location x=16, 18, 20, 22mm (16%-22%c) under different wind speed conditions were plotted in Fig. 5.10(a). The film flow at that range was far away from the direct impinging range, so the film flow propagated downstream. Additionally, the curvature of the airfoil surface is small as well. The experimental film thickness is comparable with Ueno's analysis. Shown in the Fig. 5.10(a), film thickness profiles are similar. Film thickness monotonically decreases with free stream velocity except for U_∞=15m/s whose film thickness is almost the same as the film thickness of wind speed condition U_∞ =20m/s. This odd thickness might be caused by the influence of surface waves at the water-air interface. Due to our previous experimental study on the wind-driven film flow, nonlinear surface waves with wave height higher than the average film thickness were observed under free stream velocity condition $U_\infty = 15m/s$ (Zhang et. al., 2013). However, for free stream velocity $U_\infty = 10m/s$, no surface waves were observed. For free stream velocity $U_\infty = 20m/s$, shallow wave height surface waves were detected. Although, the wave pattern is also influenced by the water flow rate, due to our observation, higher crest height nonlinear wave is much more likely to generate under small water flow rate. We can predict that kind of nonlinear wave happened for free stream velocity $U_\infty = 15m/s$. However, for the free stream velocity larger or smaller than 15m/s, either moderate interfacial wave or no interfacial wave occurred in the film flow surface. Film flow with nonlinear waves is a highly unsteady flow, the steady linear velocity profile approximation within the film ceases to be valid. Additionally, the interfacial wave increase the mass flux within the film as well (Rothmayer and Tsao, 2000), as a result, film thickness decreases under condition $U_\infty = 15m/s$.

In order to evaluate the $U_\infty^{-3/4}$ law, point x=20mm (20%c) was selected to compare the measurement h_o and h_o predicted by the scale law (Fig. 5.10(b)). The scaling law that predicts h_o is calculated by $h_o|_{U_\infty} = (U_\infty/10)^\alpha h_o|_{U_\infty=10}$. Where α is a scale parameter (e.g., $\alpha = 0.75$). As the icing tunnel does not have a honeycomb and screen structure, the airflow turbulence intensity is relatively higher. As discussed above, the continuity shear stress condition is used in Ueno's derivation which leads to $h_o \sim \tau^{-1/2}$, where τ is the skin fraction. In laminar flow, skin fraction τ is proportional to $U_\infty^{3/2}$, as a result, $h_o \sim U_\infty^{-3/4}$. For the current study, the Reynolds number ranges from 6.7×10^4 to 2.0×10^5. As described in Schlichting (2000), for turbulence flows in this Reynolds number range, the velocity profile within the boundary layer follows the 1/7 power law. The semi-empirical expression of the skin fraction coefficient of a flat plate is:

$$c_f = 0.074 Re^{-1/5} \tag{5.14}$$

Then, skin fraction is proportional to $U_\infty^{9/5}$, so as $h \sim U_\infty^{-9/10}$. We plot scaling parameter $\alpha = -0.75$ and $\alpha = -9/10$ to exhibit the turbulence effect.

In Fig. 5.10(b), for $U_\infty > 20 m/s$, both the -3/4 and -9/10 scaling film thickness is close to the measurement value. It proves that the thin film flow will not significantly influence the air boundary. The measurement h_o is thinner than the h_o forecasted by the -3/4 scaling and -9/10 scaling is closer to the measurement result. The experimental film thickness is more consistent with turbulence scaling law analysis. There are inconsistencies for U_∞=15m/s, as we discussed above, interfacial wave with deep wave height might generate on the film surface, which invalids the Couette flow approximation. As a result, the scaling analysis no longer works.

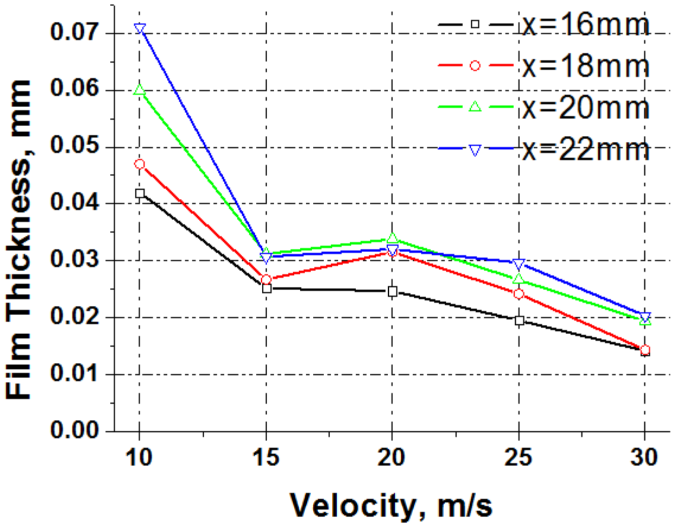

(a) Film thickness profiles at streamwise location x=16, 18, 20, 22mm

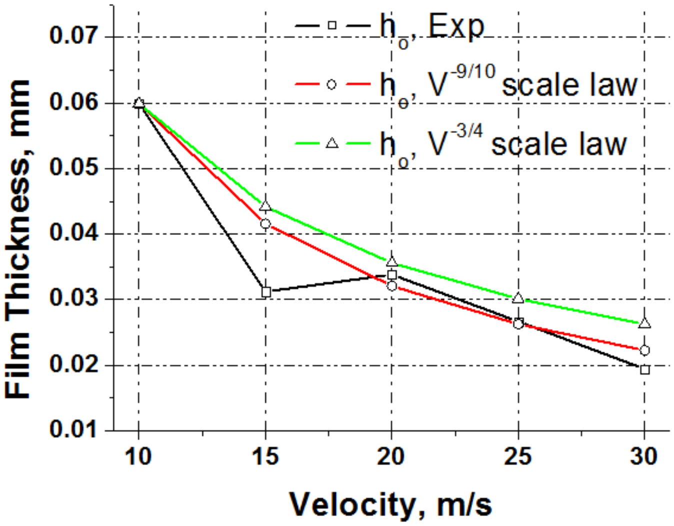

(b) Comparison of measurement film thickness with scaling law forecast film thickness at location x=20mm.

Figure 5-10 *Film thickness vs oncoming airflow velocity*

4. Conclusions

An experimental study was conducted to achieve water film/rivulets flow thickness measurements on a NACA0012 airfoil surface at five different wind speeds by using a digital image projection (DIP) system. The whole process of surface water film/rivulet flow was well revealed from the time-resolved film/rivulet thickness distribution measurements. The formation of rivulets highly relies on the initial flow structure. Film thickness scaling law is evaluated by the time-average film thickness profile. The conclusion derived from the experiments can be summarized as follows:

- At the initial stage of the impingement of the water droplets, impinging water tends to generate tiny rivulets near the stagnation line of airfoil. For the case with relatively low wind speed at U_∞= 10m/s and 15m/s, those tiny rivulets will stagnate and impinging water accumulate near the rivulets station line. A hump shape film front forms and run back slowly. Finally the film front breaks into rivulets. For the cases with relatively high wind speed (i.e., $U_\infty \geq 20$ m/s), the initial tiny rivulets slow down and merge with coming rivulets. The oncoming surface water flows tend to be transported only through formed rivulet paths. For all of wind speed, after the rivulets begin to shred from the trailing edge of the airfoil, the wetted area on the airfoil was found to be almost stable and does not change any more.

- The rivulet formation procedure is found to be a time dependent process. The steady state rivulet configuration is influenced by the rivulets formed at the initial spray stage. Surface wave behaviors significantly influence the formation of rivulets when a hump film front appears.

- Time-averaged surface water thickness distributions were determined after the water transport paths became stable. The measurement results illustrate that, the chordwise length of the water film near the airfoil leading edge, the spanwise spacing between the water rivulets and the width of each rivulet were all found to decrease monotonically with the increasing oncoming wind speed.

- The propagation part of the leading edge uniform film thickness is proportional to $s^{1/4}$ and $U_\infty^{-9/10}$.

References

Al-Khalil K, Keith Jr T, De Win K (1990) Development of an anti-icing runback model. 28th AIAA aerospace sciences meeting and exhibit. Reno, NV

Anderson DN, Feo A (2002) Ice-accretion scaling using water-film thickness parameters. 40th AIAA Aerospace sciences meeting and exhibit. Reno, NV

Anderson DN, Ruff GA (1998) Measurement and correlation of ice accretion roughness. AIAA 36th Aerospace science meeting and exhibit. Reno, NV

Bragg MB, Gregorek GM, Lee JD (1986) Airfoil aerodynamics in icing conditions. Journal of Aircraft 23:76-81

Craik ADD (1966) Wind-generated waves in thin liquid films. Journal of Fluid Mechanics 26:369-392

Da Silveira RA, Maliska CR, Estivam DA, Mendes r (2003) evaluation of collection efficiency methods for icing analysis. Proceedings of 17th international congress of mechanical engineering. Sao Paulo, SP

Feo A (2000) Icing scaling with surface film thickness similarity for high lwc conditions. madrid INTA (Instituto Nacional de Tecnia Aeroespacial) Report AE/PRO/4420/184/INTA/00 13pp

Franc p, Morency o, Tezok F, Paraschivoiu I (1999) Anti-icing system simulation using canice. Journal of Aircraft 36:999-1006

Gelder TF, Lewis JP (1951) Comparison of heat transfer from airfoil in natural and simulated icing conditions NACA TN 2480. NACA

Hansman RJ, Barsotti MF (1985) Surface wetting effects on a laminar flow airfoil in simulated heavyrain. Journal of aircraft 22:1049-1053

Hansman RJ, Craig AP (1987) Low Reynolds number tests of NACA 64-210, NACA 0012, and Wortmann FX67-K170 airfoils in rain. Journal of Aircraft 24:559-566

Marshall J, Ettema R (2004) Contact-line instabilities of driven liquid films Instability of Flows. WIT Press, Southampton, Boston,

Miesen R, Boersma BJ (1995) Hydrodynamic stability of a sheared liquid film. Journal of Fluid Mechanics 301:175-202

Nelson JJ, Alving AE, Joseph DD (1995) Boundary layer flow of air over water on a flat plate. Journal of Fluid Mechanics 284:159-169

Olsen W, Walker E (1987) Experimental evidence for modifying the current physical model for ice accretion on aircraft surfaces.

Otta SP, Rothmayer AP (2009) Instability of stagnation line icing. Computers & Fluids 38:273-283

Papadakis M, Breer M, Craig N, Liu X (1994) Experimental water droplet impingement data on airfoils, simulated ice shapes, an engine inlet and a finite wing. NASA-CR-4636.

Ranaudo RJ, Reehorst AL, Bond TH, Batterson JG, O'Mara TM (1991) Effects of horizontal tail ice on longitudinal aerodynamic derivatives. Journal of Aircraft 28:193-199

Rothmayer A, Matheis B, Timoshin S (2002) Thin liquid films flowing over external aerodynamic surfaces. Journal of engineering mathematics 42:341-357

Rothmayer AP (2003) Scaling laws for water and ice layers on airfoils 41th AIAA Aerospace sciences meeting and exhibit. Reno NV

Rothmayer AP, Hu H (2012) Solutions for two-dimensional instabilities of ice surfaces uniformly wetted by thin films. 4th AIAA Atmospheric and space environments meeting. New Orleans, Louisiana

Rothmayer AP, Hu H (2013) Linearized solutions of three-dimensional condensed layer films. 5th AIAA Atmospheric and space environments conference. San Diego, CA,

Rothmayer AP, Tsao J (2001) On the incipient motion of air driven water beads. 39th AIAA Aerospace sciences meeting and exhibit. Reno, NV

Rothmayer AP, Tsao JC (2000) Water film runback on an airfoil surface. 38th AIAA Aerospace sciences meeting and exhibit. Reno, NV

Schlichting H, Gersten K (2000) Boundary-layer theory. Springer Science & Business Media

Thompson BE, Jang J (1996) Aerodynamic efficiency of wings in rain. Journal of aircraft 33:1047-1053

Thompson BE, Marrochello MR (1999) Rivulet formation in surface-water flow on an airfoil in rain. AIAA journal 37:45-49

Tsao J-C, Rothmayer AP, Ruban AI (1997) Stability of air flow past thin liquid films on airfoils. Computers & fluids 26:427-452

Ueno K, Farzaneh M (2011) Linear stability analysis of ice growth under supercooled water film driven by a laminar airflow. Physics of Fluids (1994-present) 23:042103

Wang G, Rothmayer A (2009) Thin water films driven by air shear stress through roughness. Computers & Fluids 38:235-246

Zhang K, Zhang S, Rothmayer A, Hu H (2013) Development of a digital image projection technique to measure wind-driven water film flows. 51th AIAA Aerospace sciences meeting and exhabit. Grapevine, Texas

CHAPTER 6

GENERAL CONCLUSIONS

A novel high-speed digital image projection (DIP) system is developed to achieve non-instructive thickness measurements of water droplets and film/rivulet flows during the glaze icing process. The DIP technique can be considered as a further development of the DFP technique. In contrast to project sinusoidal patterns, grid line pattern, which is enlighten from the Molecular Tagging Velocimetry (MTV) technique, is used to reconstruct 3D shapes. By replacing the phase difference of sinusoidal patterns with displacement of grid points, the measurement bias error caused by the distortion of a projected sinusoidal pattern and the accumulated error generated by the two-dimensional phase unwrapping integration are totally avoided. The advantages of the DFP system, such as easy to set up, low cost, and non-contact whole field measurements at video speed, are persisted in the DIP technique. Moreover, the novel technique can achieve a more precise measurement with a lower requirement on the test image quality. The benefits of the novel technique were proved by reconstructing a spherical cap shape. The average measurement error of the DIP system was 0.04mm with a standard deviation of 0.04mm, which was much better than the average measurement error of the DFP system (0.12mm mean error with standard deviation of 0.08mm). The feasibility and implementation of the DIP system was then demonstrated by a series of experiment measurements of wind-driven film/rivulet flows over a flat plate, a roughness surface and an airfoil surface. The experiment results clearly reveal the dynamic features and transient micro-structures of those motions. Flow properties such as film/rivulet thickness, contact line angle and speed, and surface wave frequency and propagation speed, were quantitatively measured to elucidate the underlying physics of the water transport behaviors associated with aircraft icing.

Experimental study was performed to characterize the runback behavior of wind-driven rivulets under variety of wind speeds and water flow rates. The transient phenomena of wind-driven rivulets front were exhibited. The instantaneous rivulets front contact line velocities were calculated by further processing the measured instantaneous rivulets thicknesses. It is found that when the wind speed is low ($U_\infty = 5m/s$), a wide film front was generated. The film front was moved slowly but continuously. Further increased the wind speed ($U_\infty = 10m/s$, $U_\infty = 15m/s$), the motion of rivulet fronts were pause-move process which was significantly influenced by the presence of surface waves. For the even higher wind speed ($U_\infty = 20m/s$), the rivulet front motion accelerated or decelerated as the surface wave crest or trough reached the rivulet front. However, the surface wave did not influence the rivulet motion for a long timescale. The Force Balance (FB) rivulet breaking criterion was evaluated and refined by the elucidated transient motion of rivulets and the instantaneous-micro structure of the rivulet flows. The height-width ratio of rivulet bodies was found to be a small value. As a result, the linear velocity distribution within rivulets' body could be an well assumption to predict the inertia force of the rivulets. The aerodynamic force was found to apply on the bottom of the connection area between the rivulet front hump and the rivulet body. Therefore, the area difference between the rivulet front and rivulet body should be used to predict the aerodynamic drag. Rivulet meandering and the water mass trapping effect due to the meandered water-air contact line were revealed during the experiment. Wind-driven rivulet meandering instability threshold is modeled based on the force balance analysis between the inertia force, the capillary force and the aerodynamic drag. The relative importance of those force terms is determined by doing Scale analysis. It is found that the final rivulet meandering was a balance between the surface tension and the aerodynamic drag. The deduced equation was then used to predict the yaw angles of meandered rivulets, which are in agreement with experimental results.

The wind-driven water film flows over a flat/rough surface was quantified by the DIP technique. The air flow boundary layers over a film flow with roughness arrays were disclosed by the PIV measurements. The air boundary layer over the flat plate without the roughness array was found to be a laminar flow boundary. Although the air boundary separations were observed downstream of the roughness array, the influence area of the roughness array was found to be a limited range right behind the roughness element ($s/d < 4$). The roughness itself would not disturb the air boundary layer at the region far away from the roughness array ($s/d > 8$). Laminar to turbulent boundary layer transients were induced by the water film flow itself or combined effect of the film flow over a roughness surface. The DIP measurements show that the surface waves of the wind-driven film flow are sensitive the free stream velocity. Sinusoidal waves were observed for low wind speed ($U_\infty = 10ms$), whereas irregular sharp-crest surface waves were generated under higher wind speeds. The presence of roughness array will not change the propagation frequency of the film flow. The water mass trapped effect of roughness occurs right after the roughness. The trapped mass ratio due to the presence of roughness was obtained which shows that the trapped mass can be 10 times higher than the water mass of the original film flow. The trapping effect was found to be more sensitive to free stream velocity and less sensitive to film flow rate. The longer roughness array may decrease the mass trapping effect because of the higher turbulence intensity induced by the longer roughness surface.

The DIP measurement system was used to investigate the wind-driven film/rivulet flows on an NACA0012 airfoil surface. The behaviors at the initial stage of water runback flow were disclosed in details. At the initial water runback stage, tiny rivulets occurred near the stagnation line of airfoil. Under low wind speeds ($U_\infty = 10m/s$, $U_\infty = 15m/s$), the rivulets stagnation period was long and the coming impinging water accumulated near the rivulets stagnation line. A hump shape film front was generated and ran back along airfoil slowly. Then the film front broke into rivulets and finally formed a steady film-rivulets surface water runback configuration. For higher wind speeds ($U_\infty > 20m/s$), the initial tiny rivulets slowed down and merged with coming tiny rivulets. Then the rivulets size grew bigger and started to flow along the airfoil surface. The impinging water followed the water paths of those bigger rivulets and finally evolved to a film-rivulets configuration. The initial water transport behavior clearly revealed that the rivulet formation on an airfoil surface is a time-dependent process. Time-averaged surface water thickness distributions were determined through DIP measurements. The film flow scaling laws were evaluated by the averaged leading edge film thickness which was found to be proportional to $s^{1/4}$ and $U_\infty^{-9/10}$.